ELSEVIER

Physics Reports 375 (2003) 1–103

PHYSICS REPORTS

www.elsevier.com/locate/physrep

Magnetic light scattering in low-dimensional quantum spin systems

P. Lemmens[a,*], G. Güntherodt[b], C. Gros[c]

[a] Max Planck Institute for Solid State Research, Heisenbergstrasse 1, D-70569 Stuttgart, Germany
[b] 2. Physikalisches Institut, RWTH Aachen, D-56056 Aachen, Germany
[c] Institut für Theoretische Physik, Univ. des Saarlands, D-66041 Saarbrücken, Germany

Received 1 July 2002
editor: D.L. Mills

Abstract

An overview of one- and two-dimensional quantum spin systems based on transition-metal oxides and halides of current interest is given, such as spin-Peierls, spin-dimer, geometrically frustrated and ladder systems. The most significant and outstanding contributions of magnetic light scattering to the understanding of these materials are discussed and compared to results of other spectroscopies and thermodynamic measurements.

PACS: 75.10.Jm; 78.30.−j

Keywords: Transition metal compounds; Low-dimensional quantum spin; Magnetic light scattering

---

Contents

---

* Corresponding author. Tel.: +49-711-689-1631; fax: +49-711-689-1632.
E-mail address: plemmens@fkf.mpg.de (P. Lemmens).

PII: S0370-1573(02)00321-6

0. Preface

This article reviews recent progress in magnetic light scattering in one- and two-dimensional quantum spin systems. These systems received considerable attention during the past decade both from a theoretical and an experimental point of view. Following the investigations of the two-dimensional superconducting cuprates and the search for related transition-metal oxides a fascinating field of copper oxide compounds, vanadates, manganites and nickelates opened up. These compounds show effects of strong electronic correlations and magnetism in low dimensions, in particular interplay between spin, charge and orbital degrees of freedom.

The theory of magnetism in one dimension, on the other hand, has a history reaching back to the origin of quantum mechanics. This is due to the fact that a spin chain allows more easily analytical or numerical solutions. It was found that the suppression of "trivial" long-range magnetic order sets the stage for an enormous complexity of possible ground states, exotic quasiparticles and many-body states. Understanding these effects is the most intriguing challenge at present.

A central concept in describing these low-dimensional quantum spin systems is that of a spin liquid. This ground state is dominated by strong quantum fluctuations, pronounced spin–spin correlations and a suppression of long-range magnetic order. The Heisenberg chain with isotropic antiferro-magnetically coupled ($s = 1/2$) spins represents such a state in the sense that the spin–spin correlations decay algebraically. It is therefore often denoted as a critical spin liquid. An interesting situation occurs when competing interactions lead to a sudden change of the excitation spectrum, e.g., the opening of an excitation gap or the formation of long-range magnetic order. These quantum phase transitions are driven or controlled by the exchange coupling parameters, the exchange topology or by spin vacancies. The excitation gap may be realized with or without a spontaneously broken translational symmetry.

The spin-Peierls transition and the related charge ordering instability discovered in the inorganic compounds $CuGeO_3$ and NaV_2O_5, respectively, represent the case of broken translational symmetry. These compounds allow to investigate the excitation spectrum going from a homogeneous gapless to a dimerized state just as a function of temperature. In the two-leg spin ladder system $SrCu_2O_3$ and the chain/ladder system $Sr_{14}Cu_{24}O_{41}$ an excitation gap is realized without breaking translational symmetry. These compounds are discussed as model systems for an electronic mechanism of high-temperature superconductivity. The steady improvement of understanding also leads to surprising reinterpretations of compounds that have been investigated for years. The formerly canonical example of a spin ladder, the vanadium compound $(VO)_2P_2O_7$, is now recognized as a spin chain with strongly alternating coupling constants. This result has profound consequences for the interpretation of its low-energy excitations. Very important compounds that bridge one and two dimensions and still do not show long-range magnetic order are the spin frustrated system $SrCu_2(BO_3)_2$ and the 1/5-depleted square lattice system CaV_4O_9.

Light scattering experiments or other spectroscopic methods like inelastic neutron scattering have been used to investigate both the above cited and many more compounds. One of the most significant aspects of light scattering experiments is the observation of magnetic singlet bound states. These states originate from strong triplet–triplet interaction and characterize the excitation spectrum of the spin system. Recent theoretical progress has enabled a more detailed understanding of these effects. Parameters like dimerization, frustration, interchain coupling, and spin–phonon coupling have an important impact on the ground state and the excitations of a quantum spin system.

This review is organized as follows: After a brief description of the excitations and the phase diagram of quantum spin systems given in Section 1, important low-dimensional model-type spin systems, recent experimental results and their interpretations are discussed in Section 2. Up to now no comprehensive review on this rapidly growing field exists that also considers materials aspects. Therefore, we try to balance between well established results and very recent developments. In Section 3 magnetic light scattering in low-dimensional spin systems is reviewed. The following

Sections 4 and 5 discuss magnetic bound states and quasielastic scattering, respectively. Section 6 finally summarizes aspects of the present knowledge in this field and gives an outlook to future developments.

This review benefited from discussions and collaborations with many colleagues, too numerous to mention here completely.

We would like to thank especially E.Ya. Sherman and R. Valentí for carefully reading the manuscript. P.L. and G.G. would like to express their gratitude to the recent and previous members of the light scattering group in Aachen, e.g., K.Y. Choi, J. Pommer, A. Ionescu, M. Fischer, M. Grove, G. Els, and P.H.M. van Loosdrecht.

Further valuable discussions with F. Mila, W. Brenig, K. Ueda, M. Sigrist, W. Metzner, B. Lüthi, G.S. Uhrig, C. Pinettes, M. Udagawa, V. Gnezdilov and Yu.G. Pashkevich are gratefully acknowledged. We are obliged to C. Geibel, F. Steglich, H. Kageyama, M. Isobe, Yu. Ueda, J. Akimitsu, H. Tanaka, M. Johnsson, P. Millet, A. Revcolevschi, B.C. Sales, W. Assmus, S. Barilo and their collaborators for providing numerous samples. Furthermore, P.L. acknowledges gratefully a stipend of the Venture Business Laboratory for a visit to the Institute of Integrated Arts and Sciences (IIAS), Hiroshima University.

1. Excitations in low-dimensional spin systems

In strongly correlated electron systems with integer number of electrons per site the low-energy excitations are usually given by the spin degrees of freedom. This situation is properly described by the Heisenberg exchange spin Hamiltonian. If, in addition, the exchange is restricted to low dimensions, then spin chains, spin ladders, and respective systems with a more complex exchange geometry are realized. These systems exhibit a number of unusual properties which are related to strong quantum fluctuations. These properties will be addressed in the following.

One-dimensional $s = 1/2$ spin systems (spin chains) with uniform nearest neighbor exchange coupling show according to the Lieb–Schultz–Mattis theorem a degeneracy of the singlet ground state with triplet excitations [1]. Assuming negligible spin anisotropies even for $T = 0$ the ground state is gapless and not magnetically ordered [2,3]. It is described by the Bethe Ansatz [4,5]. The spin–spin correlations are algebraically decaying, typical for a quantum critical state. Triplet excitations in such a system are not described as magnons (bosons) but as massless domain wall-like $s = 1/2$ spinons (fermions). These spinons are created as pairs, e.g., by an exchange process. Their dynamical structure factor is therefore given by a gapless two-particle continuum restricted by a lower and an upper dispersing boundary. In Fig. 1.1 a sketch of the spinon creation and the spinon continuum is given. The spectral weight of the continuum is dominant close to its lower boundary.

A quantum phase transition from a gapless critical state into a gapped state (disordered spin liquid) is induced by dimerization, i.e. an alternation δ of the coupling constants to nearest neighbors $J_{\mathrm{nn}}^{\pm} = (1 \pm \delta)J_{\mathrm{nn}}$ along the chain or by a sufficient frustration $\alpha = J_{\mathrm{nnn}}/J_{\mathrm{nn}}$ due to next nearest neighbor antiferromagnetic exchange J_{nnn} [6]. With dimerization the spinons are confined into massive triplet excitations. This confinement of spinon and antispinon composite objects (triplets) is discussed similar to the quark confinement in particle physics [7,8]. The resulting quantum disordered ground state is characterized by short-ranged exponentially decaying spin–spin correlations. In many cases the system is allowed to be described as an arrangement of spin dimers. The resulting lifted degeneracy

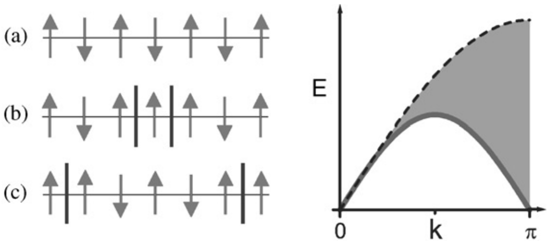

Fig. 1.1. Spin excitations on a homogeneous chain. On the left-hand side following (a)–(c) the generation of two spinons (vertical bars) by a spin flip and consecutive exchange processes is given. On the right-hand side the corresponding two-spinon continuum is shown. The spectral weight of the continuum is maximal on the dispersing lower branch.

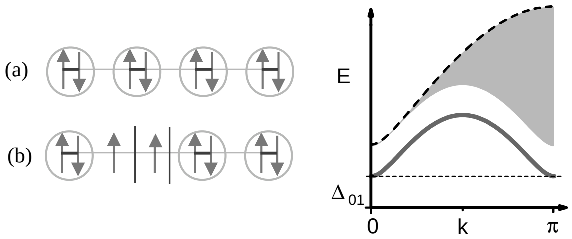

Fig. 1.2. Sketch of spin excitations on a dimerized chain. Breaking a dimer (a)–(b) corresponds to the singlet/triplet gap Δ_{01} with the respective triplet dispersion shown on the right-hand side. The continuum of "free" triplets is reached for energies $E > 2\Delta_{01}$. For small $\mathbf{k}$ there exists a finite slope of the dispersion relation.

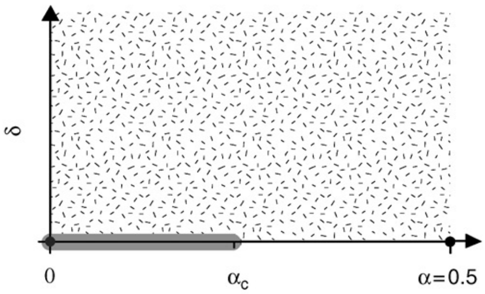

Fig. 1.3. Phase diagram ($T = 0$) of spin chains in dependence of dimerization δ and spin frustration α. For $\delta = 0$ and $\alpha \leqslant \alpha_c = 0.2412$ (dark grey bar) a gapless quantum critical ground state exists. The remaining dashed region denotes the phase space of the gapped quantum disordered state.

of triplet and singlet excitations leads to an energy gain of the system. Fig. 1.2 shows a sketch of the excitation processes in a dimerized chain with the respective energy dispersion. The dimerization or alternation of the coupling constants connects $\mathbf{k} = 0$ and $\mathbf{k} = \pi$, therefore a small part of the continuum spectral weight ($\propto \delta^2$) is also expected for $\mathbf{k} \leqslant \pi/2$ [6]. In Fig. 1.2 this contribution is neglected. A ($T = 0$) phase diagram of dimerized and frustrated spin chains is given in Fig. 1.3. The points ($\delta = 0, \alpha = 0$) and ($\delta = 0, \alpha = 0.5$) correspond to the Bethe Ansatz and the Majumdar–Ghosh point, respectively. For $\delta = 0$ and $\alpha_c < \alpha < 0.3$ the gap remains numerically small [9–12].

The simplest representative of the quantum disordered state, however, is the two-leg spin ladder with an approximately equal or larger exchange coupling along the rungs with respect to the coupling along the legs of the ladder [13]. The singlet ground state is composed of spin dimers on the rungs. Here, the term spin liquid is even more appropriate as it is not based on a broken translational symmetry. An excitation in this picture of strong dimerization corresponds to the breaking of one dimer. The energy related to this process is the singlet–triplet gap Δ_{01}, see Fig. 1.2. A coupling of more than two chains to three-, four- or five-leg ladders leads to the experimentally proven

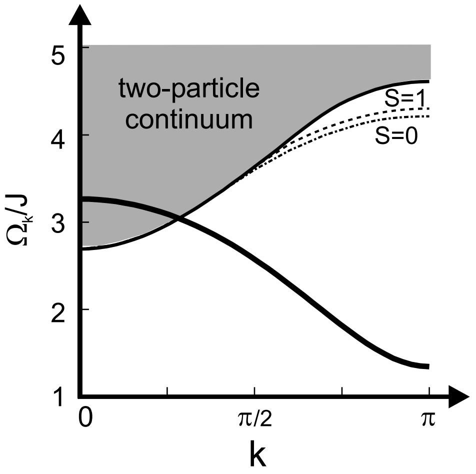

Fig. 1.4. Dispersion of magnetic excitations of a homogeneous two-leg ladder with $J_\perp = 2J_\parallel$. The triplet branch as well as the lower boundary of the two-particle continuum are given by full lines. The dashed lines mark singlet ($S = 0$) and triplet ($S = 1$) bound states [21].

conjecture that ladders with an even number of legs have a spin gap while odd-leg ladders are gapless [14,15].[1]

In the limit of a large number of coupled chains a two-dimensional Heisenberg system is obtained and the magnitude of the respective spin gap is going to zero. This limit may also be used to understand the two-dimensional high-temperature superconductors (HTSC). Weakly doped two- and three-leg ladders have been theoretically investigated in this context [19,22–24]. However, also in two dimensions spin dimer ground states with a gapped excitation spectrum are realized. This happens either if the exchange topology is modified to favor a dimer ground state, e.g., in removing 1/5 of the spins from a square lattice [25–27], or due to strong frustration (next nearest neighbor interaction) [28].

The triplet–triplet interactions that are responsible for the opening of the gap also lead to magnetic bound states, i.e. triplet excitations that are bound to singlet, triplet or quintuplet states [6,21,29–31]. The former two states are characterized by a well-defined excitation with an energy reduced with respect to the energy of the two-particle continuum of "free" triplets. If interchain or magnetoelastic interactions are dominant, bound states consist of soliton–antisoliton pairs [32–36]. Neglecting these effects, the binding energy of a bound state in a dimerized spin chain originates from frustration. The maximum number of bound states of a spin chain is restricted to one singlet and one triplet state. In spin ladders with an additional diagonal frustration the number of bound states and their binding energy is less limited and increasing with frustration. In Fig. 1.4 the excitation spectrum of a homogeneous two-leg $s = 1/2$ ladder is shown with a singlet and a triplet bound state at the lower

---

[1] It should be mentioned that the combined effect of dimerization and interchain interaction may also lead to a vanishing spin gap in a quantum spin system. In a certain parameter space of a two-leg ladder [16] with additional frustration, 4-spin cyclic exchange or interchain interactions, quantum phase transitions to gapless phases have been observed [17,18]. On the other hand, there is theoretical evidence for a spin gap in doped three-leg ladders for a certain set of exchange coupling constants [19,20].

boundary of the two-particle continuum [21]. A quantum phase transition at a critical frustration into a gapless phase is understood as a condensation process of many-particle bound states together with a general softening of the excitation spectrum [30]. More generally, magnetic bound states may therefore be used to study the triplet–triplet interaction, determine the coupling parameters and the phase diagram of the system.

If defects, either as localized non-magnetic vacancies or as mobile carriers, are introduced into a quantum spin system its excitation spectrum may change drastically [37–41]. In a 2D square lattice doping with mobile carriers destroys long-range Néel order and leads to the opening of a pseudo-gap for spin and charge excitations. The effect of localized spin vacancies in dimerized spin chains or in even-leg spin ladders is different. Here, a transition from a gapped into an ordered and gapless Néel-type state is induced by a seemingly negligible amount of vacancies. This effect is based on the doping of only weakly bound spinons by every vacancy. Thereby additional excitations are introduced in the gap corresponding to staggered moments for sites far from the vacancy and increasing spin–spin correlations [38,42,43]. Interchain interaction leads to the occurrence of magnetic order at finite temperature.

The coexistence of true long-range magnetic order and dimerization is possible if spatial variations of the competing order parameters are taken into account [44]. This means that the excitation spectrum of such a system has two features, the gapped triplet mode due to dimerization and the gapless "spin wave mode" [45]. The emergence of antiferromagnetism keeps the structure and the energy scales of these modes essentially unchanged as the transfer of spectral weight from the gapped to the spin wave mode is realized with only a small reduction of the gap and an increase of the spin wave velocity. The latter mode is damped with a broadening proportional to the square of the wave vector [46]. Similar arguments have recently been used to describe the interplay or competition of disorder-induced antiferromagnetism and superconductivity in Heavy Fermion compounds [45]. Comprehensive experimental studies concerning the effect of spin vacancies exist for spin ladder and dimerized spin chain systems. Some results including light scattering data will be presented in the next section.

The effect of mobile carriers on the gapped excitation spectrum of a spin liquid is directly related to the problem of an electronic mechanism for HTSC and not yet understood completely [47–49]. In the 2D CuO_2 square lattice the doped holes are believed to form self-organized slowly fluctuating arrays of metallic stripes in which the motion of holes shows a locally quasi-one-dimensional character [50–52]. A spin gap or pseudo-gap is then the result of the spatially confined Mott-insulating regions of the material in the proximity of the metallic stripes. This effect has been described by the term "topological doping" [48]. Corresponding theoretical studies of weakly doped two- and three-leg ladders confirm these ideas in the sense that a tendency toward a binding effect of holes either into a superconducting condensate or charge ordered ground state exists [22–24]. The excitation spectrum of the latter system is of special interest as it is separated into a gapless Luttinger-liquid (odd channel) and an insulating gapped spin liquid phase (even channel) [20,24]. In some sense this spectrum represents or mimics the scenario of spin and charge separation discussed for HTSC. A quantum phase transition into a superconducting state with d-wave character has been predicted for the three-leg ladder at higher doping levels [24].

In a very simplified picture the two channels of the three-leg ladder may be understood as a "plain" ladder coupled to a chain. Holes hop back and forth from the chain to the ladder system. In the ladder they prefer to form pairs minimizing the number of broken dimers. Hopping back into the chain system this correlation is “partially transferred” into the conducting channel [20,24]. The experimental part of this problem is far from being completely settled and therefore under progress. Although only few spin ladder systems are available, unusual experimental results exist, pointing to **k**-dependent relaxation rates different from the undoped material [53]. In the following section a thorough review of the presently known inorganic low-dimensional compounds will be given focusing on the questions discussed above.

2. Important inorganic quantum spin systems

A general advantage of the use of inorganic compounds like transition-metal halides and oxides is the availability of large single crystals of considerable quality. This advantage is based on their high thermal stability. Recent developments in crystal growing techniques together with the wider availability of optically heated travelling solvent floating zone (TSFZ) furnaces [54] enabled systematic substitution studies for several inorganic compounds. These investigations themselves provided further motivation due to surprising results in the sense of rich phase diagrams and a modification of the low-energy excitations [36,37,40,42,55–58]. Unfortunately only few compounds have been realized where doping of mobile carriers is achieved. Here the application of high pressure either during crystal growth or later during the determination of phase diagrams proved to be important and is still growing in acceptance. In contrast, the use of soft chemical routes, such as hydrothermal growth, is still limited, partly due to problems in the controllability of the growth parameters [59]. The sample quality of compounds that have a singlet ground state may be judged by measurements of the magnetic susceptibility in dependence of temperature. Every spin defect induces a local moment that is observed as a “Curie contribution” to the magnetic susceptibility.

2.1. Structural considerations and important parameters

Three building principles exist that reduce the superexchange of a 3d ion–oxygen configuration to less than three dimensions. These are on the one hand an enlarged distance or missing bridging oxygen between two 3d ion sites or on the other hand a superexchange path with an angle different from 180°. Due to the Kanamori–Goodenough–Anderson rule (vanishing AF superexchange via perpendicular oxygen O2p-orbitals) a non-collinear exchange path leads to a weakening of the magnetic exchange of, e.g., neighboring CuO chains [61,62]. Finally, so-called lone pair cations, such as As^{3+}, Se^{4+}, Te^{4+}, Pb^{2+} or Bi^{3+} in combination with halides can be used to form crystal structures with unique magnetic topologies that show a reduced connectivity [63–65].

In this way compounds representing chains, zig-zag double chains or ladders with different number of legs are realized [66,67]. Fig. 2.1 shows a comparison of several possible 3d ion–oxygen configurations. In Table 2.2 at the end of Section 2 some representative low-dimensional spin systems and their magnetic properties are listed.

Experimental parameters to expand the phase diagram are pressure, that may control the exchange interaction, and frustration that is strongly related to triplet–triplet interaction and the existence of magnetic bound states. Furthermore, the application of an external magnetic field might lead to interesting behavior. For instance in a fermionic picture (strictly applicable for a 1D system) the magnetic field controls some filling of the quantum spin system. In several systems plateaus in the

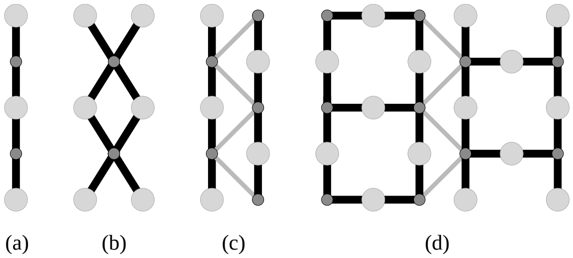

Fig. 2.1. Overview of 3d ion–oxygen configurations realized in low-dimensional transition metal compounds: (a) a linear 3d ion–O-chain, (b) a non-collinear 3d ion–O_2-chain with reduced exchange, (c) a frustrated double chain (zig-zag chain), and (d) two ladders with a frustrated weak interladder coupling. The thick (thin) lines mark dominant (reduced) exchange coupling paths. The small circles denote the positions of the transition metal ions, e.g., Cu^{2+} or V^{4+} with $s = 1/2$. The large circles denote O^{2-}. The magnetic properties of these networks depend in addition on the relative strength of the exchange coupling constants [60].

magnetization as a function of the field exist that are divided by step-like transitions (see Sections 2.3 and 2.6.2). In some systems, transitions into incommensurate magnetic phases are observed [68–70]. So far, the available literature on light scattering experiments mainly discusses $s = 1/2$ compounds. The reported experiments on $s = 1$ Haldane systems [71,72] are limited in number [73–76].

2.2. *Quasi-zero-dimensional compounds*

A series of compounds made out of weakly coupled units, mostly spin dimers or spin-tetrahedra, can be viewed in first approximation as zero-dimensional. Depending on the strength of the couplings in between the units, one might view these compounds also as quasi-one-dimensional or quasi-two-dimensional. An example is the spin-1/2 ladder compound CaV_2O_5, in which the inter-rung coupling is so weak that it might be viewed in first approximation as made up of dimers with only very weak interdimer couplings [77,78].

2.2.1. *Dimer compounds*

A spin dimer system with still noticeable interdimer interaction is realized in the copper ditellurate $CuTe_2O_5$. The structure is shown in the inset of Fig. 2.2. The lone pair cation Te^{4+} yields a magnetic insulation of pairs of strongly distorted and edge-sharing CuO_6 octahedra with respect to each other [81]. The resulting Cu–Cu distances are 3.18 Å within the pair of octahedra and 5.28 Å to the next pair [79]. The magnetic susceptibility of $CuTe_2O_5$ shows a maximum at $T_{\max} = 56.5$ K and a strong decrease for smaller temperatures. It can be described with the dimer model $\chi \propto \beta[3 + \exp(\beta \cdot J)]^{-1}$, $\beta = 1/k_B T$ [82] and an intradimer coupling $J = 90$ K. The high temperature susceptibility corresponds to a Curie–Weiss temperature of $\Theta = 41$ K.

Concerning the effect of dimerization, also the spin-Peierls system $CuGeO_3$ and the related charge ordering system NaV_2O_5 are very attractive. They allow to investigate both the homogeneous and dimerized state of a spin chain system as function of temperature. With respect to larger degrees of dimerization and a coupling of two chain systems we refer to $(VO)_2P_2O_7$ as discussed in Section 2.5.2.

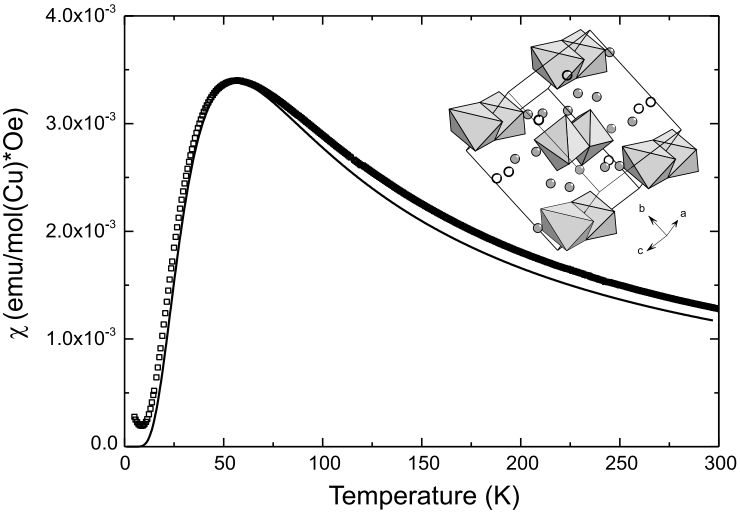

Fig. 2.2. Magnetic susceptibility (dots) and lattice structure of $CuTe_2O_5$ with edge-sharing CuO_6 octahedra forming Cu dimers. The line corresponds to a dimer fit [82] with $J = 90$ K. The open (full) spheres in the inset represent oxygen (tellurium) ions [79].

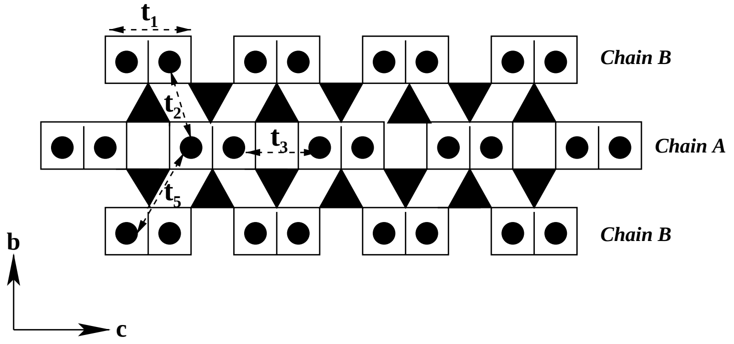

Fig. 2.3. Topology of the intra- and inter-dimer hopping matrix elements of one *bc*-layer of CsV_2O_5. Note the close resemblance to the compound $(VO)_2P_2O_7$, see Fig. 2.30. The filled triangles denote projections of $V^{5+}O_4$-tetrahedra, the filled circles the spin-1/2 V^{4+}-ions. The magnitude of the interchain hopping matrix-elements t_2 and t_5 are small [80].

The weakly coupled spin-1/2 dimer compounds $(VO)_2P_2O_7$ (see Section 2.5.2 and the crystal structure in Fig. 2.30) and CsV_2O_5 [83] are structurally very similar. Both systems contain planes of weakly coupled dimers with a topology illustrated in Fig. 2.3. CsV_2O_5 contains one of these planes per unit-cell and $(VO)_2P_2O_7$ contains two inequivalent planes. A density functional theory (DFT) and susceptibility analysis has found that CsV_2O_5 might be viewed alternatively as a strongly dimerized chain compound with a dimerization parameter of $\delta = 0.8$ [80].

The dimer compound [84,85] $CaCuGe_2O_6$ is very unusual. Crystallographically [84,86] the dominant topological structure are chains of edge-sharing CuO_6 octahedra running along the *c*-axis. The spin-1/2 Cu^{2+}-ions form nevertheless spin-dimers in between pairs of third-nearest-neighbors

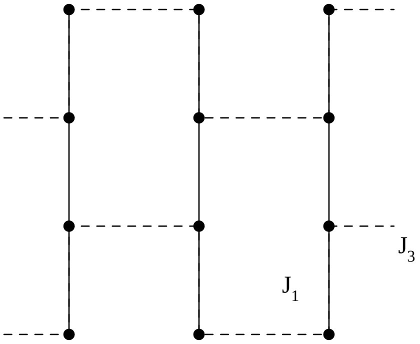

Fig. 2.4. Topology of $CaCuGe_2O_6$. The full and dashed lines denote the first- and third nearest-neighbor exchange couplings J_1 and J_3, respectively, with $J_1/J_3 \approx -0.2$, $J_3 = 67$ K, and J_1 parallel to the crystallographic c-axis.

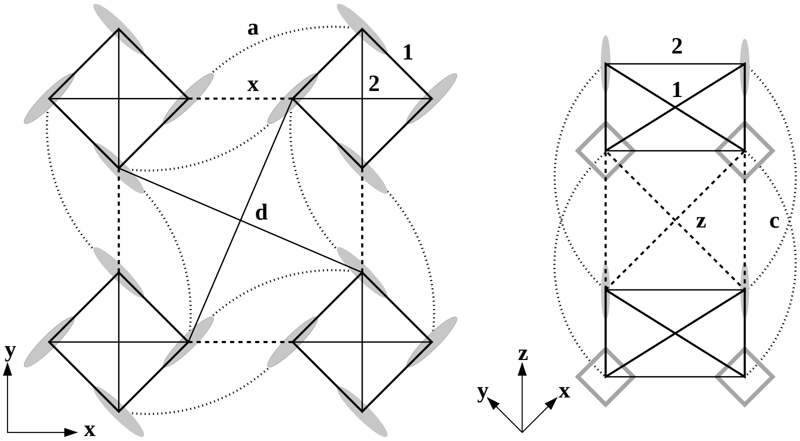

Fig. 2.5. Topology of $Cu_2Te_2O_5X_2$, with X = Br, Cl. The ovals and the squares denote the CuO_3X units which are linked by intra-tetrahedra couplings J_1 and J_2. The in-plane (ab) couplings are J_x, J_a and J_d. The in-chain (c) couplings are J_c and J_z.

located on adjacent chains. This very unusual physics is possibly due to the near-to-90° Cu–O–Cu superexchange angle along the c-axis [86]. This leads to a strong reduction of the exchange coupling which, due the Kanamori–Goodenough–Anderson rule [87–89], actually becomes slightly negative (ferromagnetic) [86]. (Fig. 2.4.)

2.2.2. The Cu-tetrahedra systems $Cu_2Te_2O_5X_2$, X=Br, Cl

In Fig. 2.5, a projection of the topology of $Cu_2Te_2O_5X_2$ with X = Br, Cl is presented. It contains tetrahedra of Cu^{2+} ions which are weakly coupled in the (ab)-plane and along the c-axis. The magnetic susceptibility as function of temperature is shown in Fig. 2.6. The susceptibility at higher temperature contains a similar Curie–Weiss-like term for both compounds. Towards lower temperatures a maximum at 30 K (Br) and 23 K (Cl) is observed in $\chi(T)$ [64]. This susceptibility can be fitted in first approximation [63] by non-interacting tetrahedra with intra-tetrahedra

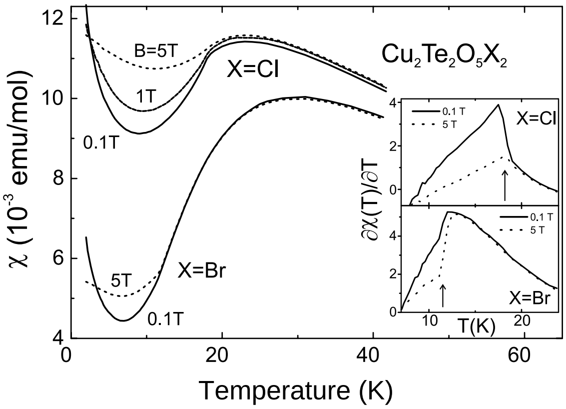

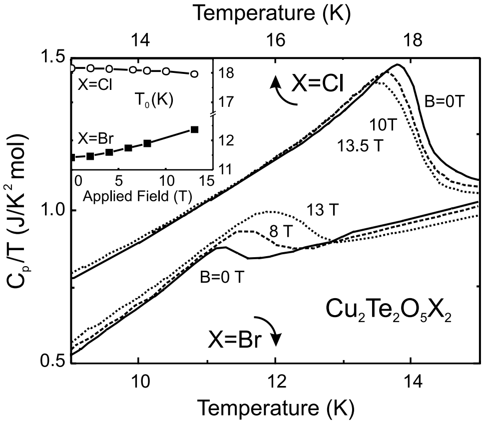

Fig. 2.6. Magnetic susceptibility of $Cu_2Te_2O_5X_2$, with X = Br, Cl for different magnetic fields. The inset shows the derivative $\partial\chi/\partial T$ at $B = 0.1$ and 5 T with the transitions assigned by arrows [64].

Fig. 2.7. Specific heat of $Cu_2Te_2O_5X_2$, with X = Br, Cl close to the transition in magnetic fields up to 13.5 T. Note the two different temperature scales for the respective compounds. The inset gives the field dependence of the transition temperatures [64].

exchange couplings $J_1 \approx J_2 \approx 43$ and 38.5 K, respectively, for the bromide and the chloride compound.

The two compounds undergo an ordering transition [64], presumably of antiferromagnetic nature, at $T_0^{(\mathrm{Br})} = 11.4$ K and $T_N^{(\mathrm{Cl})} = 18.2$ K. The smaller transition temperature of the bromide is attributed to the approximately 6% larger unit cell volume of the bromide related to a weaker inter-tetrahedra coupling. The ordering in $Cu_2Te_2O_5Br_2$ is anomalous concerning thermodynamic and spectroscopic properties. As a first example note the opposite behavior of the bromide compared to the chloride concerning the unusual shape of the derivative $\partial\chi/\partial T(T = T_0)$ shown in the inset of Fig. 2.6.

Thermodynamic properties. The specific heat $C_p(T)$ of $Cu_2Te_2O_5Cl_2$ (see upper curve with upper temperature scale in Fig. 2.7) shows a mean field like transition with a sizeable anomaly at T_N and a weak dependence on magnetic fields. These data point to a 3D-antiferromagnetic ordering of a system with only weak spin anisotropies and appreciable inter-tetrahedra coupling. The related energy scales are characterized by the ratio of the transition temperature to the maximum temperature in $\chi(T)$, $T_0/T_{\chi_{\max}} = 0.78$ for $Cu_2Te_2O_5Cl_2$. For $Cu_2Te_2O_5Br_2$ the ratio $T_0/T_{\chi_{\max}} = 0.27$ is much smaller implying the freezing out of a large part of the magnetic triplet excitations already for $T > T_0$. The derivative $\partial\chi(T)/\partial T$ reveals a small but well discernible step which has the opposite sign compared to $Cu_2Te_2O_5Cl_2$ (Fig. 2.6), i.e. the slope for $T < T_N$ is smaller than for $T > T_N$ [64].

The specific heat of $Cu_2Te_2O_5Br_2$ at $B = 0$ (see lower curves with lower temperature scale in Fig. 2.7) shows a broadened anomaly at $T = T_0(0) = 11.4$ K. This proves that this transition also occurs in the absence of an external field. Applying a magnetic field leads to a very strong increase of the size of the anomaly, by more than a factor of 3 at $B = 13$ T, and to a pronounced shift of T_0 to higher temperatures, e.g. to $T_0(B = 13\text{ T}) = 12.4$ K. This shift corresponds to a larger magnetization of the ordered state compared to the disordered state. The field dependence follows a power law

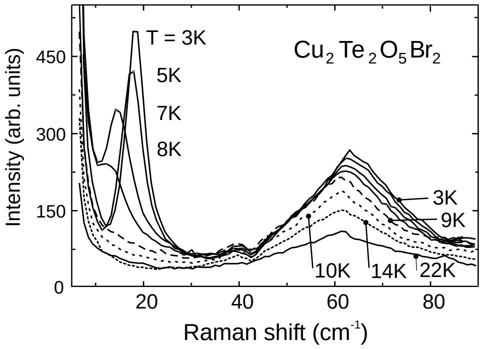

Fig. 2.8. Raman spectra of $Cu_2Te_2O_5Br_2$ as function of temperature in (cc) polarization parallel to the crystallographic c-axis [64].

with $T_0(B) = T_0(0) + a \cdot B^n$ and $n = 1.41 \pm 0.05$. The magnetic entropy at T_0 involved with the instability has been roughly estimated to be only $S_m(T_0) \simeq 1.8$ J/K mol $= 0.16 \cdot$ Rln2/spin, whereas for $Cu_2Te_2O_5Cl_2$, the entropy at T_N is much larger, $S_m(T_N) \simeq 4.1$ J/K mol $= 0.36 \cdot$ Rln2/spin.

One might view these compounds, especially $Cu_2Te_2O_5Br_2$, as weakly coupled tetrahedra compounds close to a quantum critical transition between an antiferromagnetic state and a spin liquid [92,93]. On the other hand, some of the presented results provide evidence for a sizable magnetic anisotropy and an additional Dzyaloshinskii–Moriya (DM) interaction in the spin system. This interaction is allowed due to the low symmetry exchange path lacking the inversion center. High-field magnetization experiments performed on powder samples in fields up to 50 T point into the same direction [94]. A finite but small slope is observed in $Cu_2Te_2O_5Br_2$ for "small fields" up to 15 T followed by a smooth change of slope for higher fields. This behavior is attributed to a mixing of triplets to the singlet ground state. The pseudo-spin gap of this compound is therefore attributed to an unique interplay of quantum fluctuations with anisotropies.

Magnetic light scattering. Of special interest is the possible occurrence of low-lying intra-tetrahedra singlet-excitations in magnetic Raman scattering [64,91]. Indeed Raman scattering has been the first tool to demonstrate the instability. In Fig. 2.8 Raman spectra of $Cu_2Te_2O_5Br_2$ are shown in c-axis polarization as a function of temperature. The high-temperature spectra are dominated by a triangle-shaped scattering continuum centered at 61 cm^{-1} = 88 K. This position matches the energy scale $2J = 86$ K previously determined from a fit of the magnetic susceptibility [63]. The continuum has been discussed as a two-magnon-like scattering process of a tetrahedra chain supported by the "in-chain" selection rule [95,96]. The total linewidth and low energy onset at 40 cm^{-1} both point to an appreciable inter-tetrahedra coupling. For temperatures $T < 9\text{ K} < T_0^{(\mathrm{Br})}$, a sharp maximum develops with a soft mode-like behavior. This mode reaches its maximum energy of 18 cm^{-1} at the lowest temperatures. The change of the low-energy excitation spectrum is accompanied by an increase of intensity on the right-hand shoulder of the scattering continuum leading to a small shift of the triangle to higher energies. No other transition related anomalies have been found in optical spectroscopy, especially no phonon anomalies were observed at higher energy.

The two magnetic signals are only observed with both electric field vectors parallel to the crystallographic c-axis corresponding to the chains of tetrahedra. This symmetry selection rule and the

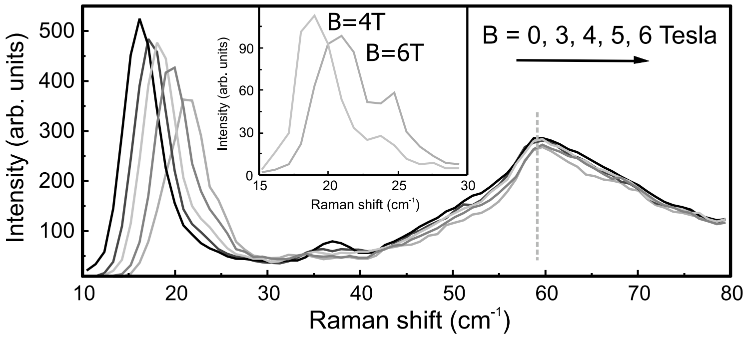

Fig. 2.9. Raman spectra of $Cu_2Te_2O_5Br_2$ at $T = 2.3$ K in (cc) polarization in magnetic fields parallel to the crystallographic c-axis. The inset shows low frequency data with higher spectral resolution [90].

temperature dependence of the low-energy mode are similar to the properties of singlet bound states observed, e.g. in the dimerized phase ($T < T_{SP} = 14.5$ K) of $CuGeO_3$. In the latter spin chain system frustration leads to a binding effect of two elementary triplets to a well-defined mode at the energy 1.78Δ [97]. The physics and phenomenology of such states will be further described in Section 4. An important difference between this pure singlet mode and the low-energy excitation in $Cu_2Te_2O_5Br_2$ is given by its quite large magnetic field dependence. In Fig. 2.9 Raman spectra are shown with magnetic fields parallel to the c-axis of the compound. The maximum frequency shifts non-linearly with the magnetic field leading to an increase by 4.5 cm^{-1} in 6 T. Also this shift might tentatively be attributed to a mixing of triplet states into the ground state due to DM interaction. At higher fields ($B > 4$ T) a second peak is induced at higher energies (≈ 22 cm^{-1}). This peak does not shift with further increase of field. This complex behavior is not yet understood in detail.

A comparison of the Raman response of $Cu_2Te_2O_5Br_2$ with the related $Cu_2Te_2O_5Cl_2$ is given in Fig. 2.10. It is obvious that the low-energy spectral response of the two compounds is completely different. In the chloride the magnetic scattering is less pronounced and more spread out. This corresponds to a larger inter-tetrahedra coupling. An interesting aspect is that substitution studies allow a continuous tuning of the composition and to study the crossover between the two systems. In samples with mixed composition a continuous shift of the phonon frequencies is observed as given in Fig. 2.11 for some selected phonon modes. Generally the spectrum of optical phonons is softer for the bromide compared to the chloride. This is related to the approximately 6% larger volume of the unit cell of the bromide. Preliminary investigations of the magnetic excitation spectrum show with increasing Cl concentration a shift of the soft mode to higher frequency and splitting into at least three peaks that finally overlap and form the continuum shown in Fig. 2.10 for X = Cl.

2.3. Quasi-two-dimensional compounds

Only very few 2D spin systems with a quantum disordered ground state are discussed in the literature in which the spin gap is comparably large and not due to spin anisotropies. In 2D this spin liquid ground state should follow from exotic exchange topologies as both the square and the triangular lattice have a Néel-like ground state [98]. Examples of 2D spin gap systems are the Kagomé lattice, the 1/5-depleted square lattice [25–27,99–101], and the Shastry–Sutherland

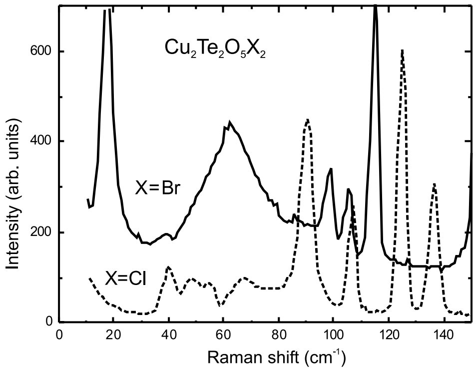

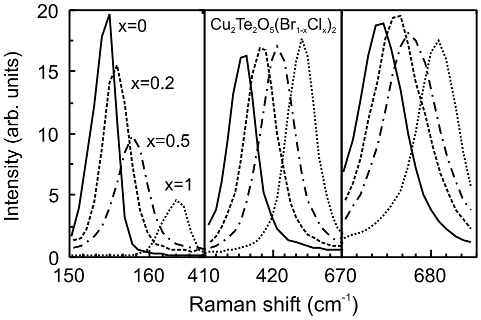

Fig. 2.10. Comparison of the Raman response of $Cu_2Te_2O_5Br_2$ and $Cu_2Te_2O_5Cl_2$ at $T = 3$ K in (cc) polarization. The curve for X = Br is shifted vertically for clarity [91].

Fig. 2.11. Phonon Raman spectra of $Cu_2Te_2O_5(Br_{1-x}, Cl_x)_2$ as function of x in (cc) polarization [90].

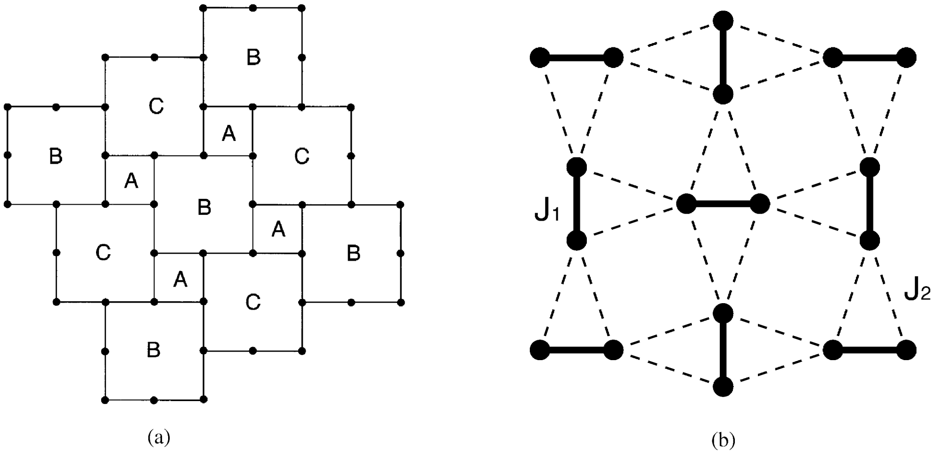

Fig. 2.12. (a) Topology of V^{4+} in CaV_4O_9 forming a 1/5-depleted square lattice with three sublattices (A, B, C). (b) Topology of Cu^{2+} in $SrCu_2(BO_3)_2$ in the ab plane. The intradimer (J_1) and interdimer (J_2) exchange couplings are given by solid and dashed lines, respectively.

lattice [28] shown in Fig. 2.12. The latter two exchange topologies are realized in CaV_4O_9 and $SrCu_2(BO_3)_2$, respectively.

2.3.1. The 1/5-depleted system CaV_4O_9

The compound CaV_4O_9 with a singlet–triplet gap $\Delta_{01} = 135$ K [25,102,103] is a 2D arrangement of plaquette singlet units of four V^{4+} atoms $(s = 1/2)$ within four corner-linked VO_5 pyramids. These are coupled by an exchange between the V spins within edge-linked VO_5 pyramids [103]. A simplifying sketch of the corresponding 1/5-depleted 2D spin structure is displayed in Fig. 2.12(a). This structure is built up by three plaquette systems, denoted by A, B and C. The exchange coupling constants are therefore divided into intra-plaquette coupling J_A, acting between spins on a link in an A plaquette, and inter-plaquette coupling J_{BC}, acting on links shared by the B and C plaquettes. Theoretically several possible ground states have been identified, e.g., a "plaquette RVB" state or, in contrast, a spin-Peierls state with a spontaneously broken lattice symmetry [26,27]. Their existence is controlled by the ratio of the coupling constants. More general, the experimentally observed gap formation has been discussed either due to the coupling of two meta-plaquette systems (i.e. plaquettes formed by n.n.n. links) or due to a considerable effect of frustration by intra-plaquette next nearest neighbor exchange interaction [104]. Theoretical and experimental results on this interesting compound are reviewed in Refs. [105,106]. Recently the structurally and electronically related SrV_4O_9 has been prepared using hydrothermal synthesis and found to have a spin gap of similar magnitude as in CaV_4O_9 [59].

2.3.2. The Shastry–Sutherland system $SrCu_2(BO_3)_2$

The layered compound $SrCu_2(BO_3)_2$ consists of buckled $CuBO_3$ planes and Sr layers. A projection of this structure on the *ab* plane realizes the frustrated 2D exchange topology shown in Fig. 2.12(b). Its magnetic ground state is a direct product of singlet dimers with a spin gap $\Delta_{01} = 34$ K [107,110,111]. Despite the problematic viscosity of borate melts, large single crystals can be prepared using an optically heated travelling solvent floating zone (TSFZ) furnace [112]. A review of experimental properties of this system is given in Ref. [113].

$SrCu_2(BO_3)_2$ is the only realization of the Shastry–Sutherland lattice studied theoretically nearly 20 years ago [11]. Its exactly solvable dimer ground state is a 2D analogue of the Majumdar–Ghosh point [10] of a 1D spin chain with a strong frustrating next nearest neighbor exchange coupling, $\alpha = J_2/J_1 = 0.5$, see Fig. 1.3. The triplet excitations in this type of frustrated lattice are almost localized leading to very flat triplet branches compared to the energy scale of the exchange coupling constants [113,114]. The corresponding "spin wave" velocities should therefore be very small leading to strong triplet–triplet interaction especially at the high symmetry points of the magnetic Brillouin zone. On the other hand, with increasing interdimer exchange coupling a quantum phase transition of the spin system from an exact dimer ground state to an antiferromagnetically ordered gapless state is expected. Then the exchange topology is equivalent to a 2D Heisenberg square lattice. The quantum critical point separating these phases is therefore controlled by the ratio $x = J_2/J_1$ of the next nearest interdimer coupling J_2 to the nearest neighbor intradimer coupling J_1. A critical ratio of $x_c = 0.691$ has been determined theoretically [28,115]. A modification of this ratio by pressure or substitutions would allow to study the crossover between these two competing states in a unique way. While substitution experiments in $SrCu_2(BO_3)_2$ did not prove to be successful, a still preliminary investigation of magnetic susceptibility under pressure has indeed shown a decrease of the spin gap as expected for a closer proximity to the antiferromagnetic state [116].

Thermodynamic properties. The magnetic susceptibility of $SrCu_2(BO_3)_2$ at ambient conditions shows a maximum ($T_m^{\chi} = 15$ K) and a rapid decrease toward lower temperatures with an exponential tail for $T \to 0$ [107], see Fig. 2.13. A similar behavior is observed in the specific heat of the spin system with a maximum ($T_m^{C_p} = 8$ K) [108] given in Fig. 2.14.

It is noticeable that the maxima in both thermodynamic quantities are observed at temperatures much smaller than the singlet–triplet gap and nearly one order of magnitude smaller than the

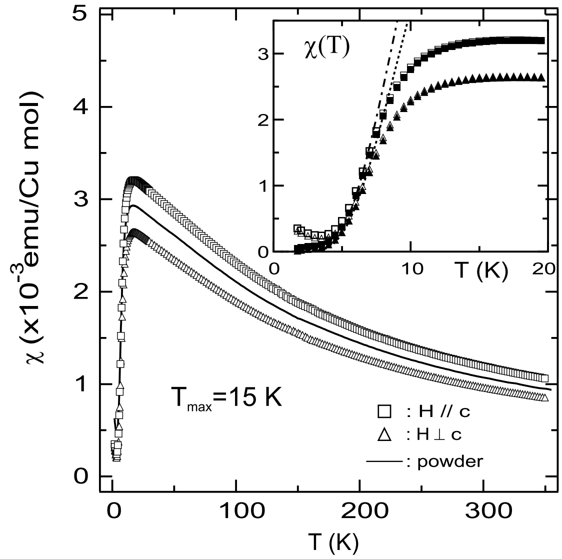

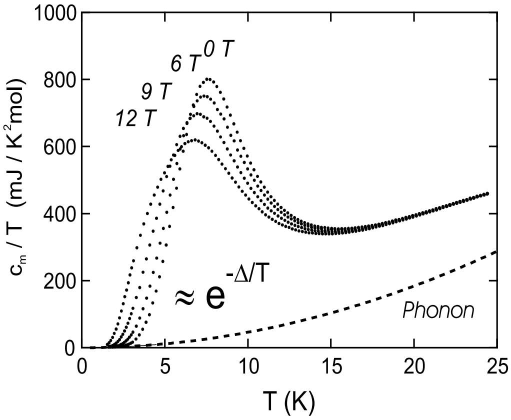

Fig. 2.13. Magnetic susceptibility of $SrCu_2(BO_3)_2$. The inset shows the low temperature evolution with a fit using a dimer model as a dashed and dotted line [107].

Fig. 2.14. Low-temperature specific heat c/T of $SrCu_2(BO_3)_2$ in magnetic fields up to 12 T. The dashed line corresponds to the estimated phonon contribution to the specific heat [108].

estimated exchange coupling constants $J_1 = 100$ K and $J_2 \approx 68$ K [28]. The resulting ratio $x = 0.68$ is just below the above given value of x_c, placing this material in the dimerized phase, close to the boundary of the Néel state. A more recent analysis of the bandwidth of the triplet branch favors smaller but still comparable values of $x \approx 0.65$ [117]. A further theoretical investigation gives evidence for $x \approx 0.6$ and an unexpected instability in the triplet channel at a critical ratio $x_t = 0.63$ [118].

The localized nature of the triplet excitations in $SrCu_2(BO_3)_2$ also shows up as five consecutive transitions from gapped to gapless phases observed in magnetic fields up to 50 T. The gapped phases are identified as plateaus in the normalized magnetization at $m = 0$, 1/3, 1/4, and 1/8. The corresponding magnetic fields are $H < 20$ T, $H \approx 30$ T and $H \approx 40$ T [107,119]. The plateau at $m = 1/3$ is attributed to a stripe phase of triplets [120]. These experiments are the first observation of a magnetic field-induced “triplet–singlet-lattice” in a 2D spin system. Until recently magnetic phase diagrams of similar complexity have only been discussed for 1D spin systems, e.g., for the frustrated double chain system NH_4CuCl_3. A thorough discussion of these topology-induced quantization phenomena is given in Section 2.6.2.

Investigations of ESR [121], IR [122] and neutron scattering [114] on $SrCu_2(BO_3)_2$ observed triplet excitations with a spin gap of $\Delta = 34$ K and a very small dispersion of only 2 K pointing to their extremely localized character. In addition, a second triplet branch $\Delta'_{01} = 55$ K with an assumed larger dispersion of 17 K was detected. This branch can be interpreted as a triplet bound state of two elementary triplets (see discussion below). Frustration due to the interdimer coupling J_2 can lead to the reduction of the ratio $\Delta'_{01}/\Delta_{01} = 1.62$ below 2 (corresponding to non-interacting magnons) [114]. In recent neutron scattering experiments the dispersion of the second triplet branch could not be confirmed. The **k** dependence of Δ'_{01} is comparable with a set of disrupted sheets with different energies in different regions of **k** space [123]. These lead to an enlarged spectral weight at $\Delta'^{a}_{01} = 58$ K and $\Delta'^{b}_{01} = 75$ K, instead of the earlier single dispersing branch. The origin of these exciton-like levels may be related to DM interaction, strong spin–phonon interaction or their interplay. It should be noted that these experimental results question the earlier determination of the magnetic coupling constants described above. The complexity of these results on a seemingly simple model system with an exact singlet ground state proves one more time the large potential of quantum spin systems for unconventional collective excitations. For these states inelastic light scattering is a valuable complementary experimental tool.

Magnetic light scattering. In Raman scattering experiments on $SrCu_2(BO_3)_2$ a rich excitation spectrum with an additional drastic evolution with temperature has been observed [124]. At high temperatures ($T > \Delta_{01}$) the light scattering spectra show strong quasielastic scattering with a Lorentzian spectral function. For intermediate temperatures this signal is gradually replaced by a broad maximum with a center of spectral weight at 50 cm^{-1}, a frequency comparable with the doubled spin gap. The temperature dependence of the scattering intensities of the respective signals has been mapped on the magnetic susceptibility and the specific heat of the spin system [124]. This kind of mapping has also successfully been used in the case of $CuGeO_3$ and $(VO)_2P_2O_7$ and will further be discussed in Section 5.

The spectrum changes drastically for very small temperatures compared with the spin gap ($T \ll \Delta_{01}$) where the above-discussed scattering intensities are completely suppressed. Four well-defined modes with energies $\Delta^{i}_{00} = 30, 46, 56$ and 70 cm^{-1} appear [124]. It is interesting to note that the splitting of these modes in Raman scattering is comparable to the splitting of the triplet bound state branch observed in neutron scattering. Nevertheless, the modes observed in Raman scattering experiments do not show an appreciable magnetic field dependence in contrast to the triplet states. These experiments will further be discussed in Section 4.4. Examples of the respective Raman data are given in Fig. 4.17.

The above-described bound state scattering is only observable with the electric field vectors parallel to the *ab* plane of the compound. There exist no inter-layer singlet bound states. There is, however, a phonon mode with peculiar properties. This pure inter-layer mode observed in spectra of (*cc*) polarization is strongly anharmonic. As its energy is comparable to the energy scale of the magnetic system it has been investigated in detail. Fig. 2.15 shows the strong softening and broadening of linewidth for temperatures $T > 70$ K with a frequency of only 35 cm^{-1} at $T = 300$ K. In the inset the frequency of this mode is shown as function of temperature. The small decrease observed in the low temperature limit ($T < \Delta = 34$ K) is larger than the experimental error and must be related to an appreciable spin–phonon coupling. Furthermore related second and higher harmonics are displayed in Fig. 2.16. The very small frequency shift of the second harmonic mode points to a negligible dispersion and a large corresponding density of states of the underlying phonon mode. These effects motivated a X-ray study that indeed observed a structural phase transition of $SrCu_2(BO_3)_2$ at $T_c = 395$ K [125]. For $T > T_c$ the compound has an inversion center and completely flat $CuBO_3$ planes. Atomic displacements involved in the transition are directed perpendicular to the *ab*-plane leading to a buckling of the planes for $T < T_c$. In the magnetic susceptibility a small step-like decrease is induced due to a change of the inter-layer couplings that are also frustrated [126,118]. The intra-layer coupling constants and their ratio are not affected.

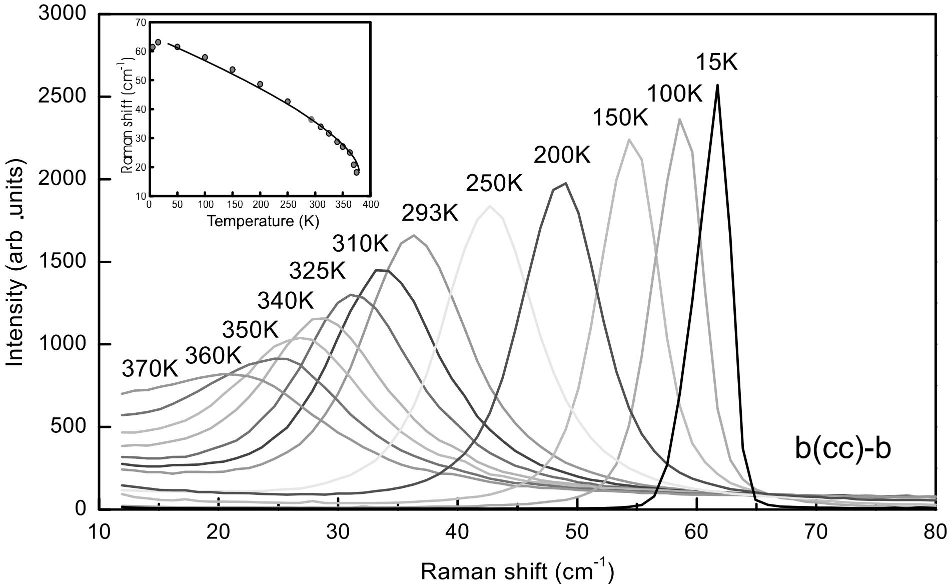

Fig. 2.15. Softening of a phonon mode in $SrCu_2(BO_3)_2$ for (*cc*) polarization as function of temperature. The inset shows the frequency of the mode. The line is a guide to the eye [109].

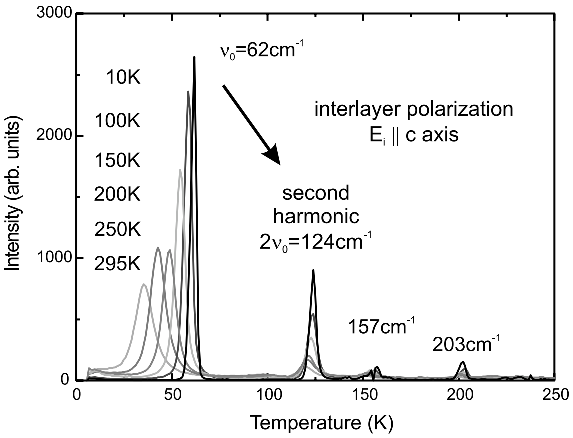

Fig. 2.16. Anharmonicity of the interlayer phonon mode at 62 cm^{-1} in $SrCu_2(BO_3)_2$ and the related second harmonic mode as function of temperature [109].

The phonon spectrum of the alternating chain system $(VO)_2P_2O_7$ has some similarities to the scenario found in $SrCu_2(BO_3)_2$ as discussed in Section 2.5.2 and displayed, e.g., in Fig. 2.32. In $(VO)_2P_2O_7$ the frequency of the phonon at 123 cm^{-1} softens by 10%. Comparing the behavior of $(VO)_2P_2O_7$ with $SrCu_2(BO_3)_2$ a relation to the high symmetry crystallographic phase of $(VO)_2P_2O_7$ might be appropriate. This phase is stabilized under high pressure and has a higher symmetry and a smaller number of independent alternating spin chains within one unit cell [127,128]. Also strong spin–phonon coupling has been discussed as the primary origin for the observed anharmonicity of optical phonons in $(VO)_2P_2O_7$ [129].

2.3.3. *High temperature superconductors*

In contrast to the 2D systems with strongly frustrated or unconventional exchange topology, the "pseudo-gap" observed in underdoped high HTSC for $T > T_c$ cannot be attributed to the exchange topology. Here the CuO_2 planes form a "conventional" square lattice. The opening of this gap as a partial and anisotropic suppression of the excitation spectrum is observed together with crossover-like effects [130]. Different experimental techniques have been successfully used to investigate this phenomenon, such as resistivity measurements, Hall effect, Raman [131,132] and IR spectroscopy, angle-resolved photoemission [7], but also NMR spectroscopy [133,134]. Therefore, these effects also involve spin degrees of freedom. The gap formation has often been associated with short-range ordered spin singlets (Zhang–Rice singlets) [46,135–138] and with fluctuating charge ordered stripes (see also the discussion in Section 1) [48].

The model of the "Nearly Antiferromagnetic Fermi Liquid" (NAFL) highlights the role of strong antiferromagnetic spin fluctuations at the so-called "hot spots" of the Brillouin zone ($\mathbf{k} = (\pi, 0)$ and $(0, \pi)$). These points are connected by the AF wave vector $\mathbf{k}_{AF}$ that remains important due to the close lying Néel phase in the temperature-doping phase diagram of HTSC. At these hot spots precursors of a damped spin density wave are expected. These may be detectable as a pseudo or spin gap with an energy scale of approximately $\Delta \approx 2\,J$. The NAFL model leads to the same symmetry of the pseudo-gap as observed in angle-resolved photoemission [139,140]. However, it is not clear whether it describes the energy scale of the pseudo-gap correctly. In several experiments pseudo-gaps with $\Delta \approx 300\,K$ have been observed. This energy scale is much smaller than the exchange coupling constants of HTSC. A strong criticism of the NAFL scenario can also be found in Ref. [141].

2.3.4. *The diluted square lattice system $K_2V_3O_8$*

Recently, also vanadates have been searched for new two-dimensional compounds [67]. The inherent flexibility in coordination and electronic configuration of the vanadium ion allows to realize exotic exchange topologies that have never before been investigated concerning their magnetic properties. An interesting candidate of this family of compounds is $K_2V_3O_8$ with an interconnection of magnetic ($s = 1/2$) $V^{4+}O_4$ pyramids and non-magnetic ($s = 0$) $V^{5+}O_4$ tetrahedra. The topology shown in Fig. 2.17 leads to a diluted square lattice with reduced exchange couplings ($J = 12.6\,K$). Due to a next neighbor exchange path with missing inversion center in between two V^{4+} sites, this system has an appreciable DM interaction and an additional c-axis anisotropy. The resulting weak ferromagnetism and field-induced spin reorientation leads to a pronounced and sharp increase of the magnetization for $T \leqslant T_N = 4\,K$ with fields parallel to the plane [142]. The ordered moment at low temperatures is $0.72\mu_B$, i.e. reduced from the expected $1\mu_B$.

Raman data of this system in Fig. 2.18 show scattering continua at low energies that might tentatively be attributed to two-magnon scattering [143]. In 2D antiferromagnets two-magnon scattering gives a dominant contribution in the B_{1g} scattering geometry. The underlying local exchange process between sublattices is also allowed at elevated temperatures above the Néel transition. Therefore this scattering intensity is not limited to low temperatures.

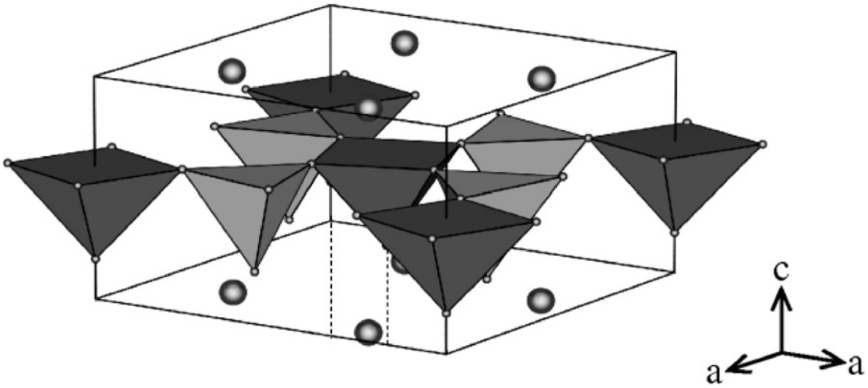

Fig. 2.17. Crystal structure of $K_2V_3O_8$ showing a plane of interconnected $V^{4+}O_4$ pyramids and $V^{5+}O_4$ tetrahedra (darker and brighter shaded, respectively) [142]. Dark spheres correspond to K^- ions, while the vanadium sites are omitted.

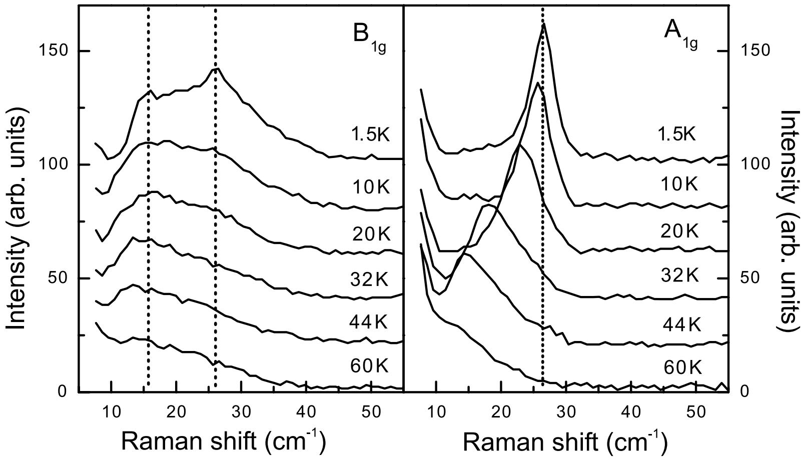

Fig. 2.18. Low-energy Raman spectra of $K_2V_3O_8$ in B_{1g} and A_{1g} symmetry. The maxima are marked by dashed lines. In B_{2g} symmetry no low-energy scattering has been observed [143].

In $K_2V_3O_8$ the scattering intensity is also observed in the symmetry-forbidden A_{1g} geometry. The presence of a symmetry-forbidden signal may be ascribed to the breakdown of the selection rules due to a non-secular term like the DM interaction. Unlike the cuprates, however, no evidence for the existence of a two-magnon signal in B_{2g} symmetry has been found. The double maximum in the B_{1g} scattering geometry remains also unexplained in this scenario. Neutron scattering experiments do not give evidence for a splitting of zone-boundary magnon branches of similar magnitude [145]. Compared to this neutron data the peak position of the continuum at 27 cm^{-1} corresponds to 3 J, a relation that matches a classical estimate for an exchange process in 2D. For a quantum, $s = 1/2$ spin system a factor 2.7 is expected especially if the reduced ordered moment is taken into account.

With increasing temperature the peak frequency of the spectrum shifts to lower frequency while the linewidth increases for both symmetries. The magnetic scattering persists at least up to $\sim 10T_N$ which is unprecedented for two-magnon scattering in similar quantum spin systems. In Fig. 2.19 the

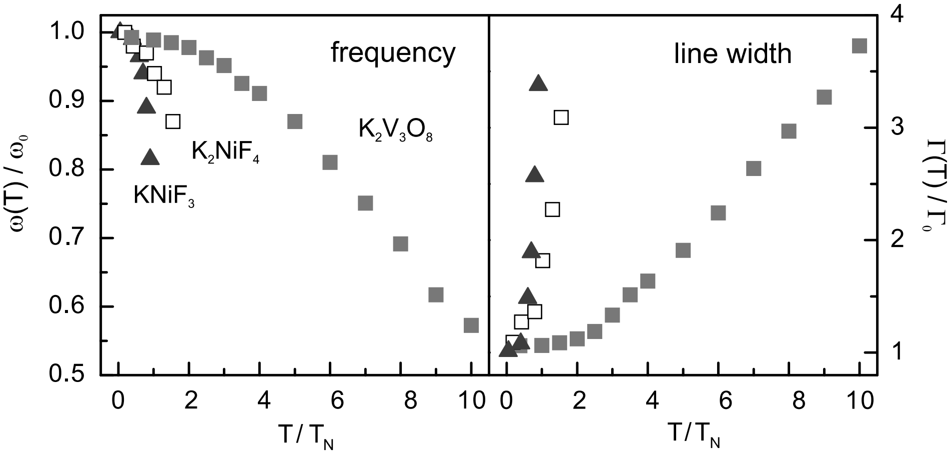

Fig. 2.19. Temperature dependence of linewidth and frequency of the scattering maxima in $K_2V_3O_8$ (full squares) in comparison with the 2D K_2NiF_4 (open squares) and the 3D antiferromagnet $KNiF_3$ (full triangles) [143,144].

temperature dependence of linewidth and frequency of the two-magnon scattering is compared with the earlier data from the typical two-dimensional and three-dimensional antiferromagnets K_2NiF_4 and $KNiF_3$, respectively [143,144]. The seemingly ineffective thermal fluctuations point to an involved energy scale which is different from that of the spin system. As a candidate orbital degrees of freedom should be discussed. The square pyramidal local symmetry of the V^{4+} is compatible with an orbital degeneracy and low energy spin–orbital coupled modes [146,147]. Phonon–orbital coupled modes have, e.g., been discussed to explain Raman scattering results in the undoped manganites $LaMnO_3$ [148].

2.4. Low-dimensional cuprates: new compounds related to high-temperature superconductors

While searching for new cuprates that are related to HTSC in their structural and electronic properties a very fascinating class of materials has been discovered. These compounds might show a similar tendency toward superconductivity [14,15,24]. Lightly doped two-leg and three-leg ladders should in their spin and charge degrees of freedom represent a minimal model for underdoped HTSC. Following the prediction of Rice and Sigrist [22,23], superconductivity was discovered in the Sr cuprate $Sr_{0.4}Ca_{13.6}Cu_{24}O_{41}$ at $T_c = 12$ K and with a pressure $P = 3.5$ GPa [150]. Fig. 2.20 shows the crystal structure of this compound containing CuO_2 chains and Cu_2O_3 ladders.

It is important not to overemphasize the similarity between the quasi-2D HTSC and the 1D Sr cuprates discussed here [151]. The HTSC parent compounds are antiferromagnetic insulators, the parent compound of the superconducting ladder material instead is a non-magnetic Mott insulator with a well-defined spin gap. This difference is partly related to the crystallographic structure. The HTSC are dominated by 2D CuO_2 square planes, the ladder compounds are built, on the other hand, by layers of low-dimensional Cu–O networks with a variety of different coordinations as shown in Fig. 2.1 [66]. Additional Sr or (La,Ca) layers separate these networks and provide a layered character of the crystal structure. The magnetic properties of these systems are only similar to HTSC in the sense that the Cu–O–Cu superexchange path is of comparable strength. The Cu–O-networks lead

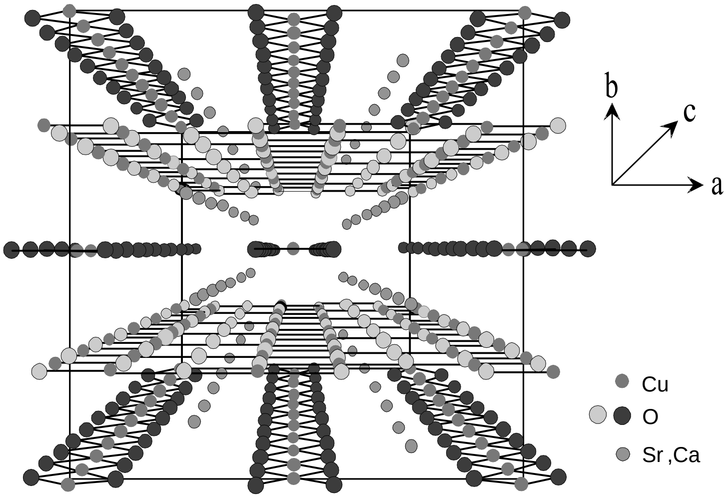

Fig. 2.20. Lattice structure of $(Sr,Ca)_{14}Cu_{24}O_{41}$ with CuO_2 chains and Cu_2O_3 ladders [149].

to a quasi-one-dimensional exchange that suppresses magnetic order [2]. To soften the above given statement it should be remarked that the compound $Sr_{14-x}Ca_xCu_{24}O_{41}$ which is the only example of a superconducting low-dimensional Sr cuprate also shows Néel ordering. However, the transition temperature is small and the ordered moments are observed on the Cu sites in the chain sublattice. Further details will be discussed in Section 2.4.2.

Other important examples of Sr cuprates are the two-leg ladder $SrCu_2O_3$, the three-leg ladder $Sr_2Cu_3O_5$ [152], the zig-zag chain $SrCuO_2$ (corner-sharing double chain) and the linear chain system Sr_2CuO_3 [153,154]. In angle-resolved photoemission experiments on the zig-zag chain $SrCuO_2$ [155] and later on the linear chain system Sr_2CuO_3 [156] spin–charge separation into spinon and holon branches have been observed. In the linear chain system Sr_2CuO_3 a picosecond switching of the optical absorption has been observed and related to the genuine electronic properties of the 1D Mott insulator [157].

It has not been possible to induce free carriers in bulk samples of these compounds. On the other hand, they play an important role as model systems [151,158]. In contrast, using a field-effect device with an insulating Al_2O_3 oxide barrier on a thin film, doping and superconductivity has been achieved near the interface with a CuO_2 infinite-layer [159] and a Cu_2O_3 ladder system [160]. In the case of the infinite-layer system, the electric-field induced doping enabled hole and electron conductivity with a respective maximum superconducting transition temperatures of $T^{\mathrm{h}}_{c-\mathrm{max}}$=89 K and $T^{\mathrm{e}}_{c-\mathrm{max}} = 34$ K just by tuning the gate voltage of the device [159]. In the ladder system $[CaCu_2O_3]_4$ field-induced hole doping led to a transition temperature $T^{\mathrm{h}}_c = 14$ K, similar to the pressure-induced superconductivity in the spin ladder system $(Sr,Ca)_{14}Cu_{24}O_{41}$. The properties of this compound will be discussed in detail in Section 2.4.2.

2.4.1. The two-leg ladder $SrCu_2O_3$

The two-leg ladder system $SrCu_2O_3$ is an extensively studied cuprate. For this exchange topology a singlet ground state and a large (≈ 0.5 J) gap to triplet excitations is expected [13,15]. Unfortunately, this compound is only available as powder samples. Therefore, most system parameters show a quite large variation in the published literature.

The exchange coupling constants parallel and perpendicular to the ladder direction are $J_{\|} = 850$–2000 K and $J_{\perp} = 750$–1000 K [154]. The existence of a spin gap with $\Delta_{01} = 280$–400 K has been verified (380 K in neutron scattering) [154,161,162]. In following experimental [43,163,164] as well as theoretical studies [37,38,40–42] the influence of substitutions on the gap and the spin–spin correlations has been investigated. Antiferromagnetic 3D long-range order with a maximum $T_N = 8$ K for $x = 0.04$ has been observed in $Sr(Cu_{1-x},Zn_x)_2O_3$. Even for very small Zn and Ni substitution levels, e.g., for $x = 0.01$, this order is still well-defined [164,165].

Neutron scattering investigations on the singlet–triplet gap have shown that its size is independent of the Zn substitution x. The spectral weight of the singlet–triplet transitions decreases monotonically with x [163]. This observation is compatible with the existence of a finite in-gap density of states which increases with x and also corresponds to the observed linear contribution to the specific heat [165]. For larger substitution levels ($x = 0.04$) almost all singlets are destroyed. Therefore, the spin gap closes. A simple estimation using the minimum k value of a finite chain and the des Cloizeaux–Pearson dispersion of triplets [5] leads to the critical concentration $x_{cr} = 2\Delta_0/\pi^2 J$ as function of the unrenormalized spin gap and the exchange coupling J [166]. NMR investigations have shown that an impurity induces a localized magnetic moment at the impurity site and small staggered moments in the entire region near the impurity [43]. These experimental observations confirm the expected changes of the excitations scheme of a spin ladder in the presence of spin vacancies.

2.4.2. The chain/ladder system $(Sr,Ca)_{14}Cu_{24}O_{41}$

The compound $Sr_{14-x}Ca_xCu_{24}O_{41}$ is a complicated system with both CuO_2 chains and Cu_2O_3 ladders. A substitution of Sr by the isovalent Ca as well as applied pressure lead to a transfer of holes from the chains to the ladders and their delocalization. Superconductivity under pressure is observed with a maximum transition temperature of $T_c = 12$ K in the doped system [150,168].

Structural considerations and Ca substitution. The crystal structure of this compound is shown in Fig. 2.20. This almost commensurate system is built up by sublattices of chains and ladders in the *ac*-plane. The sublattices are given by the dashed rectangles in Fig. 2.21. The *c*-axis lattice parameter corresponds approximately to $c_{\text{lattice}} \approx 10 \cdot c_{\text{chain}} \approx 7 \cdot c_{\text{ladder}} \simeq 27$ Å. With isovalent Ca substitution and with applied pressure the *b*- and *c*-axis parameters decrease leading to strong changes of the electronic properties, e.g., a reduction of the anisotropy in the resistivity [169]. In Fig. 2.22 the resistivity of a single crystal with $x = 11.5$ is shown as a function of temperature and pressure. Increasing pressure the anisotropy of the resistivity ρ_a/ρ_c at $T = 50$ K decreases from 80 ($P = 0$) to 10 ($P = 4.5$ GPa) [169].

Magnetic properties. The static magnetic properties of $Sr_{14}Cu_{24}O_{41}$ for $T < 300$ K are dominated by the chain system as the second gap originating from the ladder sublattice is much larger. Using magnetic susceptibility a singlet–triplet gap $\Delta_{\text{chain}} = 140$ K has been determined [170]. The gap in the ladder has been investigated using NMR, neutron and Raman scattering. The respective gap values are $\Delta_{\text{ladder}} = 550$ K in NMR or $\Delta_{\text{ladder}} = 375$ K in neutron scattering [154,171]. The Raman scattering data support the neutron scattering results [60].

A similar disparate variation of the gap values from NMR and neutron as well as Raman scattering is found for the dependence of the ladder gap on Ca substitution. While in NMR experiments a strong

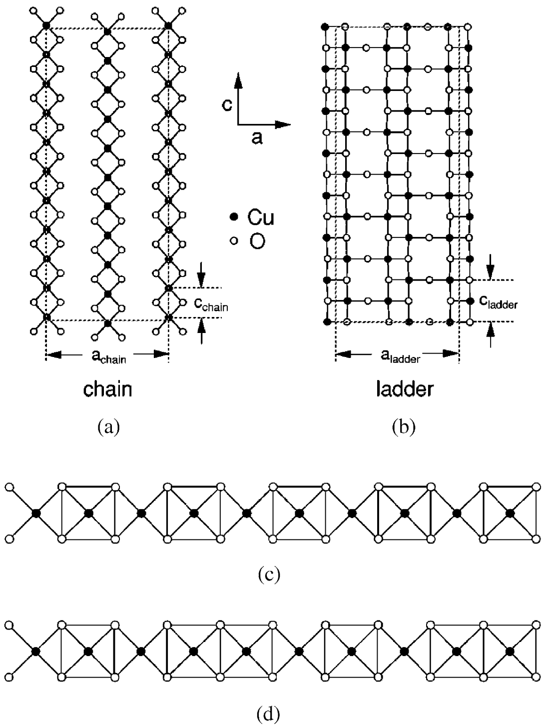

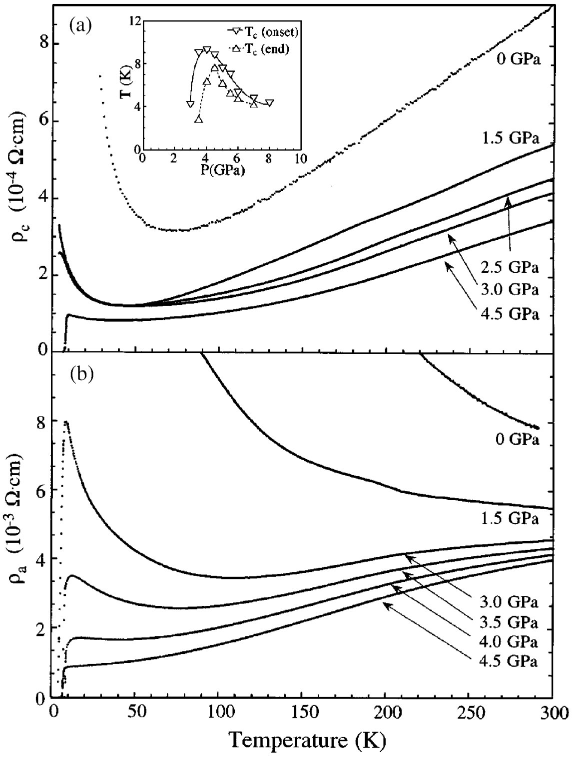

Fig. 2.21. Structure of (a) the chain and (b) the ladder sublattice in $(\mathrm{Sr,Ca})_{14}\mathrm{Cu}_{24}\mathrm{O}_{41}$ in the ac-plane and with the c-axis lattice parameters c_{chain} and c_{ladder} indicated. (c) and (d) depict two models for charge ordering in the CuO_2 chains as described in the text [167]. Squares in (c) denote dimers due to Zhang–Rice singlets and double squares in (d) denote extended singlets.

Fig. 2.22. Effect of pressure on the resistivity of $\mathrm{Sr}_{14-x}\mathrm{Ca}_x\mathrm{Cu}_{24}\mathrm{O}_{41}$ with $x = 11.5$ (a) along the ladder direction (ρ_c) and (b) perpendicular to the ladder (ρ_a). The inset shows the pressure dependence of T_c [169].

decrease of the gap on substitution from $\Delta_{\mathrm{ladder}} = 550$ to 270 K ($x = 11.5$) has been observed [154], the corresponding neutron experiments have not indicated any change [171]. A similar behavior is found in Raman scattering [60]. Fits to the triplet dispersions measured by neutron scattering have been used to determine the exchange coupling constants in the ladder. They are $J_{\|} = 1500$ K, $J_{\perp} = 830$ K ($J_{\|} = 1040$ K, $J_{\perp} = 750$ K) for $x = 0$ ($x = 11.5$) [171,172].

Optical spectroscopy. In measurements of the optical conductivity the substitution of Ca for Sr leads to a rapid transfer of the spectral weight from the high to the low energy region. This behavior is similar to observations in HTSC with increasing hole concentration [173]. In $\mathrm{Sr}_{14-x}\mathrm{Ca}_x\mathrm{Cu}_{24}\mathrm{O}_{41}$ it is the consequence of a charge redistribution from the chains to the ladders as the substitution is isovalent. The transferred spectral weight has been used to estimate the hole density in each structural element. This is given in the inset of Figs. 2.23 and 2.24. A later study using polarization-dependent X-ray absorption spectroscopy found a less pronounced charge transfer with substitution and a significant contribution from orbitals on the rungs of the ladders [176].

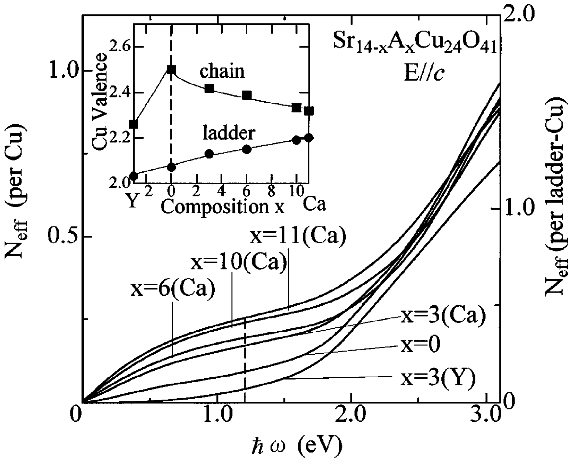

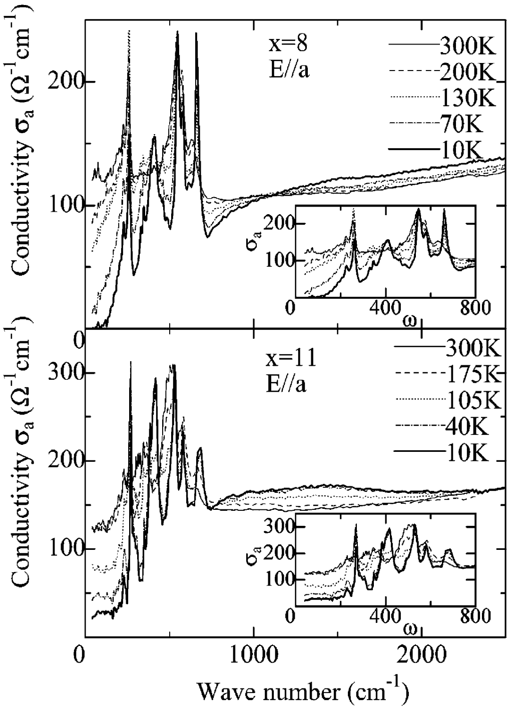

Fig. 2.23. The effective electron number per Cu (left-hand scale) of $Sr_{14-x}A_xCu_{24}O_{41}$ determined from an optical conductivity sum rule is plotted as a function of energy at $T = 300$ K. N_{eff} per ladder Cu is indicated on the right-hand scale. The valencies of Cu on both chain and ladder sites are given in the inset [173].

Fig. 2.24. The a-axis optical conductivity of $\sigma_a(\omega)$ $Sr_{14-x}Ca_xCu_{24}O_{41}$ is shown at various temperatures for $x = 8$ (upper panel) and $x = 11$ (lower panel). In the inset the low-frequency spectra are shown [174].

In recent experiments the observation of a "pseudo-gap" and a collective mode in the optical conductivity of $Sr_{14-x}Ca_xCu_{24}O_{41}$ with $x = 8$–11 has been claimed [174]. This is based on the diminishing of spectral weight for frequencies below 600 cm^{-1} ($x = 11$) and 1100 cm^{-1} ($x = 8$) with decreasing temperature for polarization parallel to the a-axis. The term "pseudo-gap" has been used for this phenomenon as it resembles the optical conductivity of underdoped HTSC [130]. However, there are also important differences. The energy of the pseudo-gap in HTSC does not strongly depend on doping. Furthermore, the derived gap energies for the chain/ladder compound do neither correspond in their magnitude nor in their dependence on Ca substitution to the neutron scattering results. Therefore, and as a gap of primary spin character is observed here in the charge degrees of freedom, conclusions based on IR absorption data are not unambiguous.

In addition, optical conductivity in c-axis polarization shows a doping-dependent peak at 50 cm^{-1} ($x = 11$) and 100 cm^{-1} ($x = 8$) [174]. FIR investigations on samples with $x = 0$ identified a pronounced frequency dependence in the optical conductivity forming a peak at 2 cm^{-1} for temperatures up to 150 K [177]. This peak may be connected with slowly fluctuating charge dynamics or a charge density wave instability.

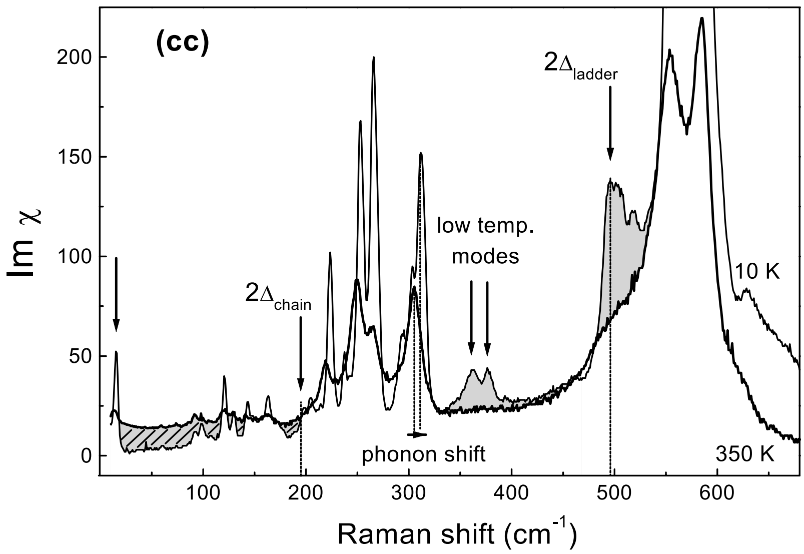

Fig. 2.25. Raman light scattering spectra of $Sr_{14}Cu_{24}O_{41}$ in intraladder (*cc*) polarization at 10 K (thin line) and 350 K (thick line). The gap features, low temperature modes, and the frequency shift of the phonon at 312 cm^{-1} that is sensitive to charge ordering are marked by arrows. The spectra are corrected for the Bose factor and show the imaginary part of the susceptibility [60,175].

In Raman scattering experiments on non-substituted $Sr_{14}Cu_{24}O_{41}$, shown in Fig. 2.25, a decrease of the scattering intensity below 200 cm^{-1} and an enhancement of a shoulder near 490 cm^{-1} have been observed upon cooling [60,175]. This renormalization of scattering intensity for frequencies smaller than 200 cm^{-1} (290 K) and 490 cm^{-1} (700 K) corresponds to $2\Delta_{\mathrm{chain}}$ and $2\Delta_{\mathrm{ladder}}$. These values are in good agreement with the above-discussed neutron scattering and susceptibility data. Furthermore, charge ordering in the chain system is evident as a shift of a phonon mode from 306 to 312 cm^{-1} and the appearance of additional side bands at lower energy for $T = 10$ K. These observations will be discussed further below.

In Fig. 2.26 it is shown that with Ca substitution the gap feature of the ladder system near 490 cm^{-1} is smeared out but does not vanish or decrease in energy. In contrast, the smaller gap in the chain sublattice near 200 cm^{-1} is destroyed for $x \geqslant 5$. This supports the negligible substitution dependence of the spin gap in the ladder system investigated in neutron scattering. The anomalies of the phonon mode at 312 cm^{-1} related to charge ordering in the chains are completely suppressed on substitution.

In addition, a very low-frequency mode is observed near 14 cm^{-1} at $T = 10$ K that disappears in the substituted samples. Instead, quasielastic scattering is observed. The origin of this signal is unclear and it may be related to an additional modulation of the charge density. Additional medium energy modes are induced for lower temperatures in the frequency range 350–400 cm^{-1} corresponding to $1.5\Delta_{\mathrm{ladder}}$. They are marked by arrows in Fig. 2.25 [60]. The intensity of these modes vanishes with increasing temperature with a power law and faster than the intensity of the gap-related shoulder at $2\Delta_{\mathrm{ladder}}$ [175]. No magnetic field dependence of the above described features has been observed in fields up to 6 T. A room temperature investigation of the scattering intensity at higher frequencies

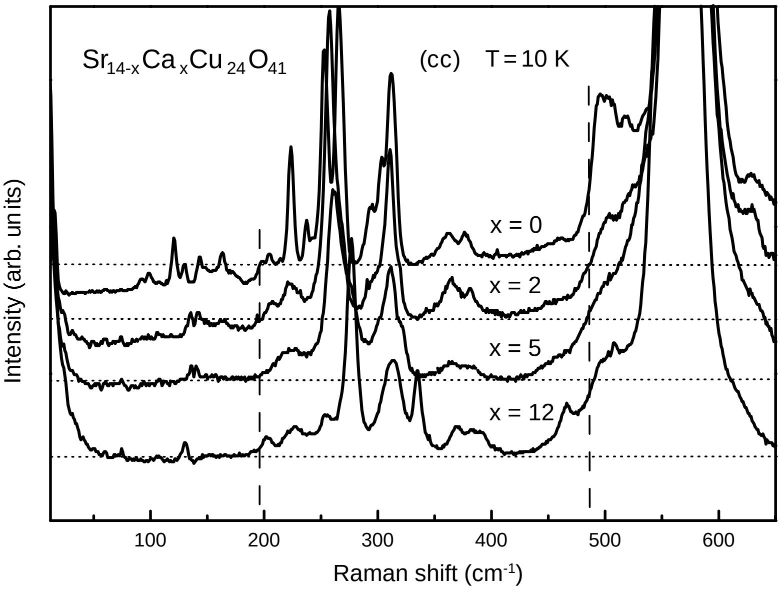

Fig. 2.26. Raman light scattering spectra of Ca-substituted $Sr_{14-x}Ca_xCu_{24}O_{41}$ with $x=0$–12 in intraladder (cc) polarization. The dashed lines are guides to the eye. The background of the scattering intensity is indicated by a dotted line [60].

and in dependence of La and Y substitution may be found in Ref. [178]. In these experiments additional modes have been proposed to originate from IR-active phonons.

The high-energy regime of the Raman spectra in $Sr_{14-x-y}Ca_xY_yCu_{24}O_{41}$ has intensively been investigated and analyzed by several groups as function of substitutions and in a resonance study. Important parts of the corresponding results will be discussed in Section 3.5. Early studies found a very sharp peak in $Sr_{14}Cu_{24}O_{41}$ in (cc) polarization at 3003 cm^{-1} with a high-energy shoulder forming two broader maxima at 3700 and 4300 cm^{-1} [179,180]. A similar maximum in (aa) polarization is weaker in intensity and the high-energy peaks are missing. From these peak positions exchange coupling constants $J_{\|} = 1000\ cm^{-1}$ and $J_{\perp} = 950\ cm^{-1}$ of the ladder system have been estimated. These experimental data have been theoretically reanalyzed by Freitas et al. [181,182] and Schmidt et al. [77] concerning coupling constants and higher order Raman scattering effects. In Fig. 3.7 some of the results for the undoped $La_6Ca_8Cu_{24}O_{41}$ are compiled together with model calculations [77].

It has very early been highlighted that the two-magnon signal shows an anomalously small linewidth at low temperatures, i.e. only about 1/10 of the corresponding linewidth of roughly $1000\ cm^{-1}$ in 2D systems [179,180]. Comparing these results with the undoped compound $La_6Ca_8Cu_{24}O_{41}$ it is clear that the small lineshape must somehow be related to the doping of the system. This observation is in some objection to the localization of the holes on the spin chain sub-system at ambient pressure and the given substitution levels. Recently the two-magnon scattering has been reinvestigated and confirmed, showing that the intensity and lineshape of the two-magnon peak is strongly dependent on the energy of the incident light [183]. These resonance effects are proposed to result from the proximity of the charge-transfer gap to the incident energy. A final understanding of the small linewidth and related phenomena is still missing.

Properties of the chain system. While even in $Sr_{14}Cu_{24}O_{41}$ the Cu valency is $+2.25$ the charge carriers are localized in the chain sublattice. The compound is an insulator [185]. This localization is connected with a dimerization and charge ordering in the chains. Corresponding superstructure peaks are observed in X-ray scattering. Their intensities increase for temperatures below 50 K and completely vanish only for temperatures up to room temperature [167].

The corresponding dimers are formed in the chains between the copper spins that are separated by 2 times the nearest neighbor Cu–Cu distance between the nearest neighbor copper ions, while the interdimers separation is 4 times that distance. The dimerization is discussed to originate from the formation of ordered Zhang–Rice singlets (see Fig. 2.21(c) or (d)) [167]. Here, the squares and double squares denote a Zhang–Rice singlet (Cu^{3+}) and an extended singlet, respectively. In NMR experiments the existence of both Cu^{2+} and Cu^{3+} in the chains has been verified [53]. The signal of the Cu^{3+} state splits into two peaks for $T < 200$ K.

In neutron scattering investigations the observed triplet dispersion along the c-axis is described by an antiferromagnetic intradimer coupling $J_{\mathrm{nnn}} = 134$ K between next nearest neighbor Cu ions and a ferromagnetic interdimer coupling $J_2 = -13.2$ K [172]. A second neutron study found two triplet branches of the chains system, an acoustic and an optic branch. This leads to an intradimer coupling as given above, an interdimer coupling along the c-axis $J_c = 9$ K, and an interdimer coupling along the a-axis $J_a = 8.6$ K. The dimer configuration indicates a quasi-2D hole ordering of the states with $s = 1/2$ and $s = 0$. The latter $s = 0$ spin states are due to Zhang–Rice singlets [186].

The charge ordering-induced phonon anomalies in $Sr_{14}Cu_{24}O_{41}$ can easily be correlated with the gap formation in the chain subcell as both quantities are determined simultaneously by a Raman scattering experiment. In Figs. 2.25 and 2.26 it is evident that in the energy regime of 250–350 cm^{-1} modes shift with temperature and form additional satellite peaks. This temperature dependence can precisely be mapped on the temperature dependence of superstructure peak intensities from X-ray scattering experiments [167]. The phonon frequencies are therefore related to the order parameter of charge ordering in the chain system. Fig. 2.27 shows the evolution of the A_1 mode at 304 cm^{-1} that shifts to 312 cm^{-1} at lower temperatures with the formation of additional split-off modes at 294 and 303 cm^{-1}. Noteworthy is the non-monotonous change of frequency with the largest slope at approximately $T \approx 150$ K for $Sr_{14}Cu_{24}O_{41}$. This mode has recently be assigned to an O-vibration of the chain along the diagonal of the ab plane [187]. Comparing these shifts with respective results on substituted samples a coherence length of charge ordering of only 27 Å at $T = 150$ K can be estimated using the averaged distance between the substitution sites in the chain.

Following a simple model developed for similar phonon anomalies in NaV_2O_5 due to the Coulomb energy contribution to the lattice force constant [188], see Section 2.52, the shift of the phonon frequency is given by a Coulomb contribution δ_{cou} leading to $v = \sqrt{(\kappa + \delta_{\mathrm{cou}})/M}$. Additional modes may be activated due to a back-folding of phonon branches by the 5-time increase of the chain unit cell [186]. On the other hand, supposing that the mode at 304 cm^{-1} is an in-phase vibration, then in the case of charge asymmetry, the normal coordinates are linear combinations of the in-phase and out-of-phase vibrations, and therefore new “in phase” modes appear in the Raman spectra. If this mixing is strong enough, each of the new modes can be interpreted as a vibration of one Cu ion. In NaV_2O_5 such a mixing of in-phase and out-of-phase modes has been identified to explain the observed phonon anomalies due to charge ordering and charge transfer [189,188].

The gradual increase and smooth crossover of the phonon frequency displayed in Fig. 2.27 points towards short range fluctuations typical for charge ordering in quasi-1D systems. It has not only been

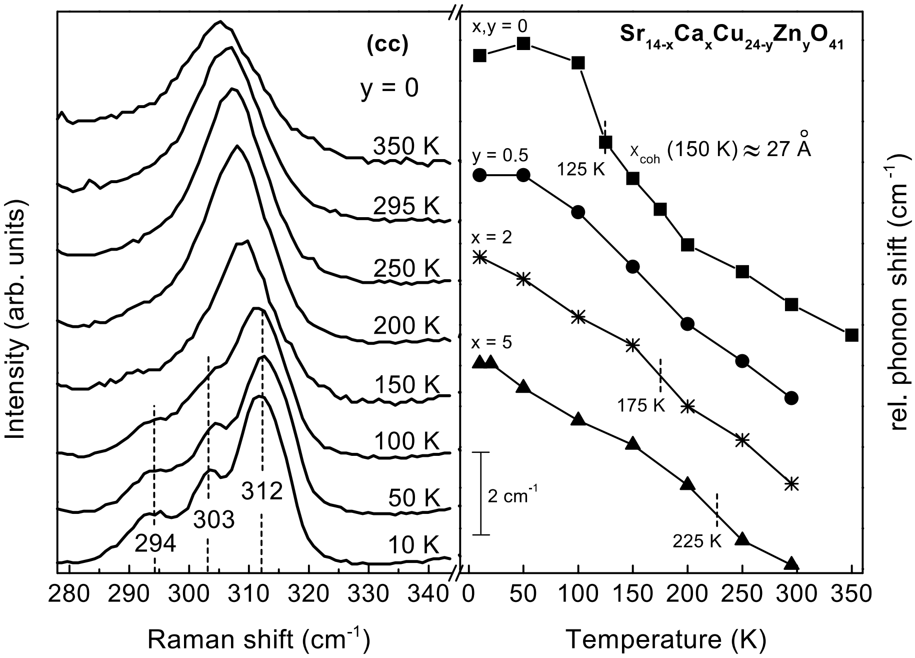

Fig. 2.27. Enlarged view on the phonon anomaly at 312 cm^{-1} in $Sr_{14}Cu_{24}O_{41}$ in interchain (aa) polarization (left panel). The right panel shows the phonon frequency as function of temperature for a pure ($x = y = 0$) sample as well as for Ca ($x \neq 0$) and Zn ($y \neq 0$) substituted samples. Crossover temperatures (T^*) are indicated by dashed lines [184].

observed in the present compound and in NaV_2O_5 but also in the stripe ordering of charge and spin in $La_2NiO_{4+\delta}$ [188–190]. The phonon frequency in $Sr_{14}Cu_{24}O_{41}$ shows a sudden increase of slope at a certain temperature ($T \approx 200$ K). This effect must be related to an increase of the coherence length and induced by an additional interchain or magnetoelastic coupling. These details have not been resolved in the X-ray experiments as incoherent scattering is lost. Therefore, the phonon-probe is more sensitive to local charge ordering [167].

The effect of different substitutions on the phonon mode at 312 cm^{-1} is presented in Fig. 2.28. While Ca substitution suppresses the appearance of the split-off modes quite fast, i.e. already at a Ca content of $x = 2$ these modes are strongly reduced in intensity, Zn and Ni substitution on the Cu site do not suppress the split-off modes at all. This is based on the charge transfer from the chains to the ladders induced by Ca substitution. This charge transfer suppresses the charge ordering and the dimerization of the spins in the chain subsystem. Thereby also the evolution of the spin gap in the chain system is suspended. However, even at high Ca substitutions $x \geqslant 5$ still a frequency shift of the phonon is observable while the spin gap is not detectable anymore (right panels of Fig. 2.28). This is related to the different coherence lengths of the spin and the lattice system. The non-linear dependence of the spin gap in the chain system on the charge ordering/transfer estimated by the integrated and normalized phonon shift demonstrates clearly that this gap formation needs a well-established coherence of charge ordering.

Effect of pressure and the phase diagram. Under applied pressure holes are transferred from the chain to the ladder system [154,170]. The carriers are delocalized with further pressure. The

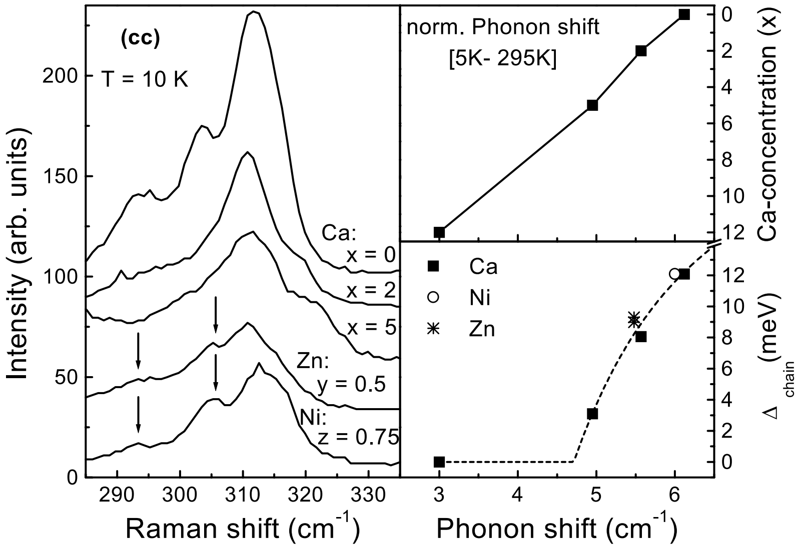

Fig. 2.28. Effect of Ca, Zn and Ni substitution on the phonon anomaly at 312 cm^{-1} in $\mathrm{Sr}_{14}\mathrm{Cu}_{24}\mathrm{O}_{41}$ (left panel). In the right panels the temperature-induced integrated frequency shift of the phonon at 312 cm^{-1} is taken as a measure of the charge ordering and related to the spin gap of the chain system [184].

effects observed in resistivity shown in Fig. 2.22 are discussed as a dimensional crossover to a two-dimensional system [169]. Superconductivity appears in $\mathrm{Sr}_{0.4}\mathrm{Ca}_{13.6}\mathrm{Cu}_{24}\mathrm{O}_{41}$ at $T_c = 12$ K and an applied pressure of $P = 3.5$ GPa [150]. NMR experiments on a sample with $x = 12$ indicate a collapse of the gap to a "pseudo-spin gap" under pressure [191] as shown in Fig. 2.29. This is meant to describe a reduced but not completely diminished density of states. In contrast, preliminary neutron scattering experiments under pressure do not support this result [192].

The different behavior of the ladder spin gap observed in neutron scattering and NMR may be related to the fact that the former method probes a coherent singlet–triplet transition while the latter samples low-energy relaxations via partly localized states in the gap. The experimental results therefore indicate a more complex low-energy spectrum than resolved by neutron scattering. This spectrum may contain magnetic bound states [60] and collective modes [174] as evidenced in optical experiments. However, a limited amount of sample inhomogenities that would not show up in neutron scattering experiments may also explain the inconsistencies.

Recently an additional AF order (10^{-1}–$10^{-2}\mu_B$) of Cu moments on the chain and ladder site has been found in Ca substituted $(\mathrm{Sr},\mathrm{Ca})_{14}\mathrm{Cu}_{24}\mathrm{O}_{41}$. Long range ordering is also observed in $(\mathrm{Ca},\mathrm{La})_{14}\mathrm{Cu}_{24}\mathrm{O}_{41}$ that shows no superconductivity under pressure. The Néel temperature is $T_N = 2$ and 10 K for $(\mathrm{Sr},\mathrm{Ca})_{14}\mathrm{Cu}_{24}\mathrm{O}_{41}$ and $(\mathrm{Ca},\mathrm{La})_{14}\mathrm{Cu}_{24}\mathrm{O}_{41}$, respectively. In the former compound T_N increases strongly for further Ca substitution $x \geqslant 12.5$. Therefore, in $\mathrm{Sr}_{14-x}\mathrm{Ca}_x\mathrm{Cu}_{24}\mathrm{O}_{41}$ the two phases of superconductivity and antiferromagnetism are separated only by pressure [193,194]. Recent neutron scattering and μSR experiments on samples with $x = 11.5$ and ambient pressure observe a coexistence of the singlet state and antiferromagnetism with an inhomogeneous distribution of the internal fields [195].

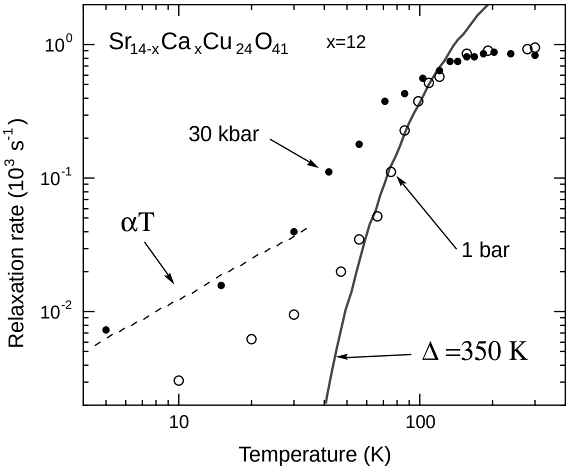

Fig. 2.29. Effect of pressure on the NMR relaxation rate and the spin gap in $Sr_{14-x}Ca_xCu_{24}O_{41}$ with $x = 12$. The measurements at ambient pressure (open circles) show a fit (full line) expected for a spin gap of the ladder with $\Delta_{\mathrm{ladder}} = 350$ K. For a pressure of 30 kbar (full circles) a weaker temperature dependence is observed (a power law is shown as a dashed curve) [191].

The above discussed investigations are very important as they try to clarify whether superconductivity in $Sr_{14-x}Ca_xCu_{24}O_{41}$ is induced in a low-dimensional gapped spin liquid state or whether applying pressure "simply" increases the dimensionality. In the latter case this compound would better be characterized as a quasi-two-dimensional system. This approach is somewhat supported by estimates of the upper critical field H_{c2} that show only a weak anisotropy in the ladder plane [196]. From the present experimental status, however, the scenario of a doped spin liquid should be favored. Recently a further spin ladder compound, β'-$Cu_{0.66}V_2O_5$, showing evidence of superconductivity under pressure has been found [197]. This compound and related low-dimensional vanadates will be discussed in the following paragraph.

2.5. Low-dimensional vanadates

There exist an even larger number of low-dimensional vanadium–oxygen compounds than of cuprates as more diverse coordinations and a broader composition range are accessible [67]. Many systems show effects of strong electronic correlations, e.g., charge and/or orbital ordering, Mott metal–insulator transitions and spin density wave ground states. Important parameters of the phase diagrams are temperature, magnetic field, composition and pressure [198]. Recently vanadium compounds have been systematically searched for interesting low-dimensional spin systems [199].

Vanadates allow different coordinations with oxygen going from VO_4-tetrahedra with V^{5+} to VO_5-pyramids, where both V^{4+} and V^{5+} valence states are observed, to VO_6-octahedra with distinct V^{3+} ions. Especially for the pyramidal coordination small, seemingly negligible changes of the local coordination may lead to drastic changes of the electronic state of vanadium, i.e. a valence change from a non-magnetic V^{5+} to the $s = 1/2$ state V^{4+}. This opens up interesting aspects of correlated charge ordering and lattice instabilities as, e.g., realized in the quarter-filled spin ladder compound

α'-NaV_2O_5. The above given geometrical elements can be arranged to form chains, ladders or more complicated 2D arrangements, leading to a multitude of possible vanadium oxides [67].

2.5.1. The AV_2O_5 family of compounds

The system AV_2O_5, with A = Li, Na, Cs, Mg and Ca is a family of V compounds that covers a broad range of low-dimensional systems such as spin chains and ladders.

The compound CaV_2O_5 is described best as a two-leg spin ladder [99,200]. The resulting singlet ground state has a spin gap of $\Delta_{01} = 500$ K. The compound MgV_2O_5 represents a two-leg spin ladder with an additional strongly frustrated coupling between the ladders [201,202]. The respective gap $\Delta_{01} = 15$ K is much smaller. The compound CsV_2O_5 has static dimers each formed by two $V^{4+}O_5$ edge-sharing square pyramids and a gap $\Delta_{01} = 160$ K [83,199]. In contrast, LiV_2O_5 is a quasi-1D anisotropic-chain system [203] without a spin gap [200,83,204].

The quarter-filled two-leg spin ladder α'-NaV_2O_5 attracted considerable interest from both experimental as well as theoretical side [205–208]. This compound is one of five existing $Na_xV_2O_5$ phases at ambient conditions. In the following it is denoted as NaV_2O_5 as its earlier determined room temperature non-centrosymmetric structure Pmn2_1 proved to be wrong [205]. On the contrary, the centrosymmetric structure Pmnm is presently used [209]. NaV_2O_5 shows a singlet formation with $\Delta_{01} = 85$ K for $T < T_{SP} = 34$ K accompanied by a lattice instability. It is therefore often assigned to spin–Peierls materials. It will be discussed in more detail in Section 2.7.2. The correlation between structural parameters, the exchange coupling constants and the exchange topology of the AV_2O_5 family is described in Refs. [199,202].

The related beta-bronzes β-$A_{0.33}V_2O_5$ with A = Na, Ag, Li as well as with A = Sr and Cu that have been investigated in the 1980s in the context of bipolaron formation have recently found a renewed interest [210–212]. The crystal structure of these compounds contains three different V sites (two zig-zag chain sites and one ladder site). In addition, there exist “channels” containing the mono- or divalent cations.

For the series with monovalent cations A = Na, Ag and Li charge ordering ($T_{CO} = 136$, 90 and 180 K) of V^{4+}: $s = 1/2$ on one chain site is observed [210] at low temperatures. This charge ordering is extremely sensitive to the cation stoichiometry. All other V-sites remain non-magnetic (V^{5+}). For even lower temperatures Néel ordering takes place ($T_N = 24$, 27 and 7 K). Transport experiments at room temperature show a quasi-1D metallic behavior. The charge ordering transitions are observed as kinks and an abrupt increase of the resistivity. Evidence for an additional structural instability exists for A = Na at approximately $T_c = 250$ K. In this latter system superconductivity under hydrostatic pressure of $P = 7$ GPa has been observed with a maximum transition temperature of $T_c = 9$ K [197].

The beta-bronzes with divalent cations are even more spectacular since for A = Sr, Ca and Cu charge ordering of V^{4+}: $s = 1/2$ is expected on the ladder sites and experimentally evidenced by NMR experiments [213,210]. Therefore in these compounds a doped spin ladder is realized. In β'-$Cu_{0.66}V_2O_5$ transport experiments under pressure ($P = 4.5$ GPa) show evidence of superconductivity with $T_c = 5$ K [197]. In this compound Cu^{1+}, that partly occupies several distinct sites in the channels of the crystal structure, plays the role of a non-magnetic dopant of the system. The structural ambiguity of the Cu site complicates the determination of the electronic structure and the effect of charge transfer from the channel to the ladder sites. Further experimental and theoretical studies on these compounds are underway.

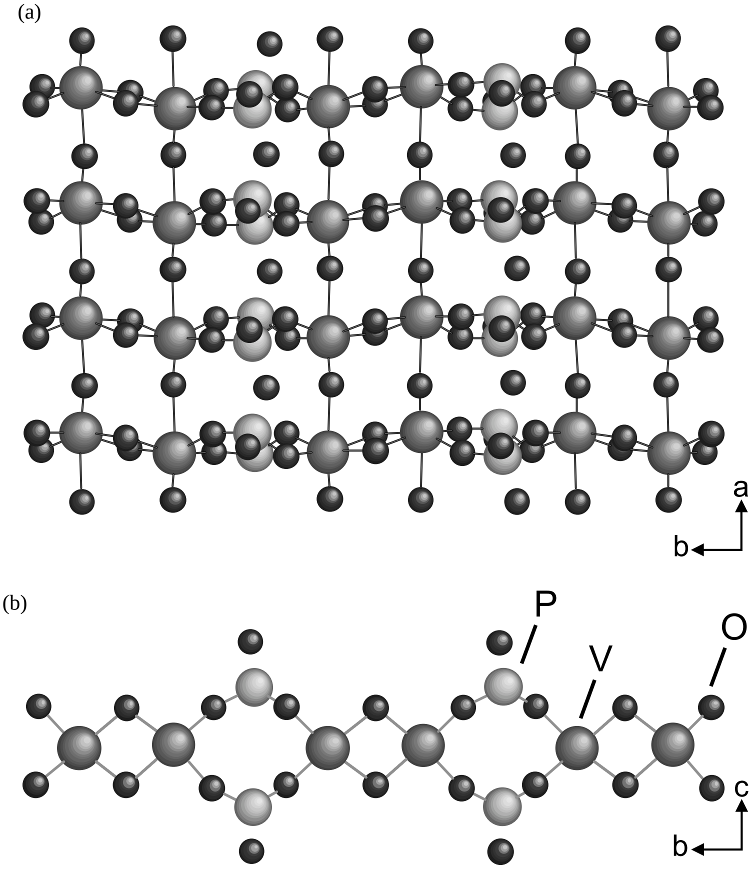

Fig. 2.30. Projected view on the crystal structure of $(VO)_2P_2O_7$ in *c*-axis and *a*-axis direction showing (a) the ladder and (b) the alternating chain, respectively. V ions are shown in grey, P in light gray and O in black [214].

2.5.2. The alternating chain system $(VO)_2P_2O_7$

In Fig. 2.30 the crystal structure of $(VO)_2P_2O_7$ (vanadyl pyrophosphate) is shown. This compound consists of chains along the *b*-axis direction with a double V–O–P–O–V link through phosphate groups alternating with a V–O–V link between edge-sharing VO_5 square pyramids. In *a*-axis direction a ladder with double V–O–V legs is formed. The magnetic susceptibility of this compound shows a maximum at 74 K and a rapid decrease at lower temperatures. Together with neutron scattering experiments on powder samples low-dimensional spin fluctuations, a singlet ground state and a gap in the excitation spectrum have been deduced [215]. However, since it was not possible to resolve the dominant exchange path direction the structural element along the *a*-axis lead to the erroneous interpretation of $(VO)_2P_2O_7$ as a spin ladder compound [15,216].

Recently, neutron scattering experiments on a batch of aligned single crystals proved the *b*-axis direction to be the dominant exchange path [217–219]. The triplet dispersion is strongest in this direction. This leads to the assignment of $(VO)_2P_2O_7$ as a chain system with a strong static alternation of the exchange coupling. Perpendicular to the chains a negligible dispersion with **k** along

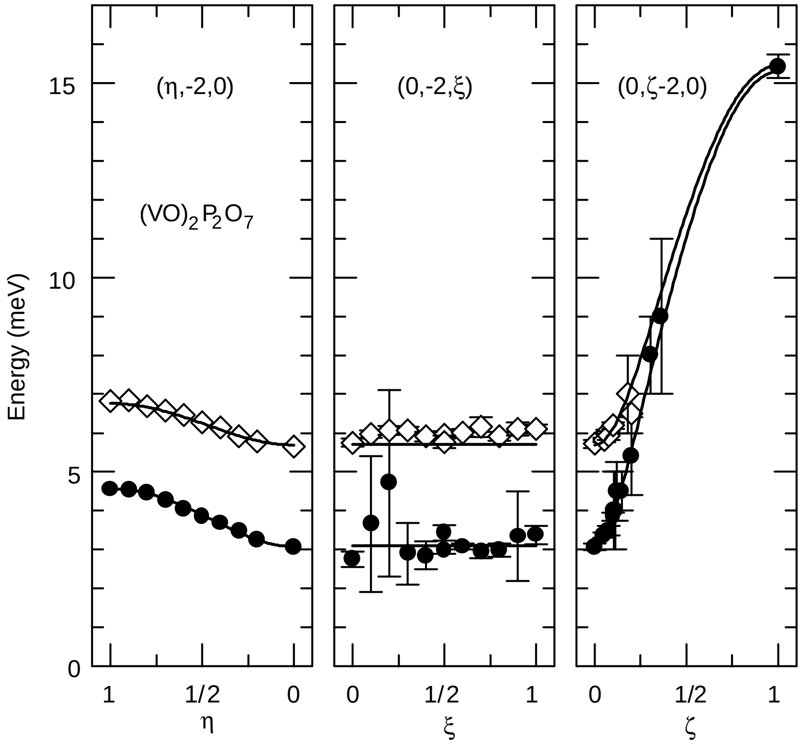

Fig. 2.31. Triplet dispersion in $(VO)_2P_2O_7$ determined by neutron scattering experiments. The first and the second triplet branch with $\Delta_{01} = 37$ K and $\Delta'_{01} = 69$ K are shown with filled and open symbols, respectively [217].

the c-axis and a weak ferromagnetic dispersion along the a-axis, i.e. parallel to the ladders, are observed.

A spin wave fit to the triplet dispersion results in exchange coupling constants of $J_1 = 120$ K and $J_2 = 100$ K along the chains (b-axis direction) and a singlet–triplet excitation gap of $\Delta_{01} = 37$ K. The zone-boundary energy of this branch is $E_{ZB} = 180$ K [220]. The larger coupling (J_1) is realized via the phosphate groups. The static alternation $\delta = (J_1 - J_2)/(J_1 + J_2) = 0.09$ is much larger compared to spin-Peierls compounds where values of only $\delta = 0.015$–0.05 are reported for $T < T_{SP}$. ESR investigations on $(VO)_2P_2O_7$ later supported by NMR point to even larger values of δ=0.2 [220,221]. Therefore, the understanding of the properties of $(VO)_2P_2O_7$ in comparison with spin-Peierls systems is important. Theories of dimerized spin systems using numerical approaches are often more practical for larger alternations [29]. For these calculations $(VO)_2P_2O_7$ may be used as a model system.

The main peculiarity of the excitation spectrum of $(VO)_2P_2O_7$ is the observation of a second triplet branch $\Delta'_{01} = 69$ K in neutron scattering experiments with a comparable dispersion as the first lower-energy triplet branch. This dispersion is shown in Fig. 2.31. The second triplet branch has been assigned tentatively to a triplet bound state of a strongly alternating chain [217]. This would have been the first experimental observation of such a signal reported in literature. Later experimental investigations, however, found evidence for two chain systems with different alternations within one unit cell of this compound. This will be discussed further below.

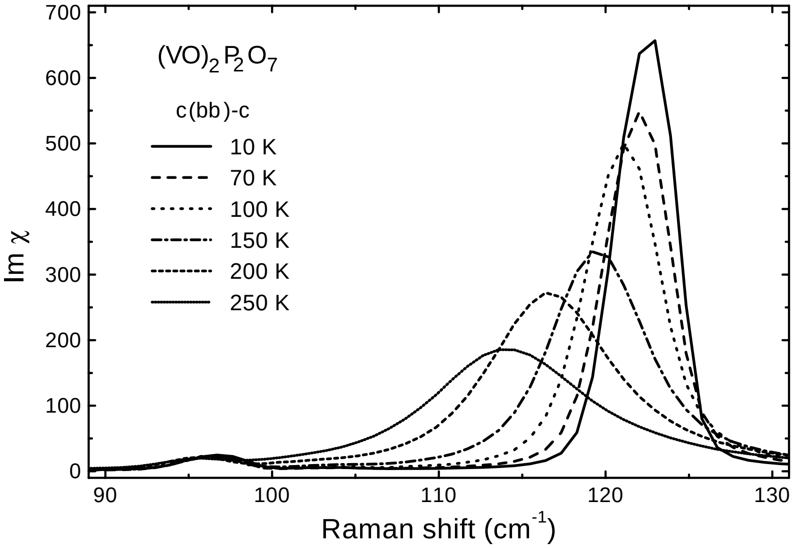

Fig. 2.32. Phonon anomalies of $(VO)_2P_2O_7$ in intrachain (*bb*) light scattering polarization [214].

The second branch has considerable intensity over the whole Brillouin zone as shown by neutron scattering. Therefore, the assignment to a triplet bound state has been criticized. Calculations show that the spectral weight of such a bound state should be dominant at the zone boundary and not at the Γ point of the Brillouin zone. This inconsistency may be solved by an additional interaction, i.e. a more complicated exchange topology [222]. Indeed, an additional frustrating interchain exchange term across the phosphate group can increase the spectral weight of the triplet bound state [31,223].

In a detailed Raman scattering study this problem has been investigated experimentally [214]. Here, no sign for strong frustration has been detected as it should manifest itself in a large binding energy and spectral weight of a singlet bound state. Respective data are discussed in Section 4.3. However, there is evidence for strong spin–phonon coupling showing up as fluctuation-induced quasielastic scattering and phonon anomalies [214]. A further Raman and IR scattering study concentrating on phonons and the respective symmetry analysis can be found in Ref. [224].

In Fig. 2.32 low-energy Raman spectra are shown. A strong anharmonicity of a phonon of $(VO)_2P_2O_7$ at 123 cm^{-1} is observed. This mode most probably corresponds to the phosphate group that mediates the exchange along the alternating chain. Its energy coincides with the energy $\Delta_{01}(\mathbf{k})$ at the zone-boundary $E_{ZB} = 180$ K $\equiv$ 125 cm^{-1}. The frequency shift of this and a second anomalous phonon mode at 70 cm^{-1} is shown in Fig. 2.33. The observed softening of the phonon frequency corresponds to a decrease of the corresponding force constant by 20%. In interchain (*aa*) scattering configuration the effects of spin–phonon coupling are similar drastic, leading to a complete vanishing of the phonon intensity of the 123 cm^{-1}-mode for temperatures $T > 80$ K (see Fig. 2.34). This temperature is comparable to $2\Delta_{01} = 72$ K. The strong spin–phonon interaction has been taken as an alternative reason for a large spectral weight of the tentative triplet bound state Δ'_{01} in the center and at the boundary of the Brillouin zone [129,214].

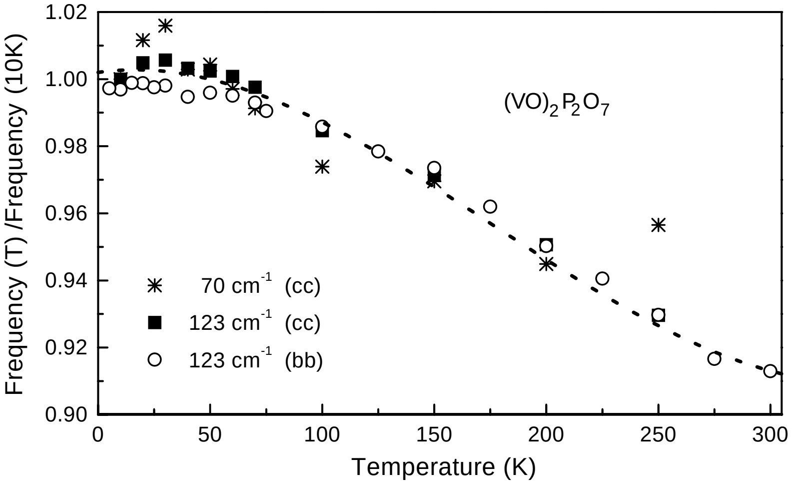

Fig. 2.33. Anharmonic temperature dependence of the frequency of the phonons in $(VO)_2P_2O_7$ at 70 and 123 cm^{-1} in intrachain (*bb*) and interchain (*cc*) polarization on a normalized frequency scale [214].

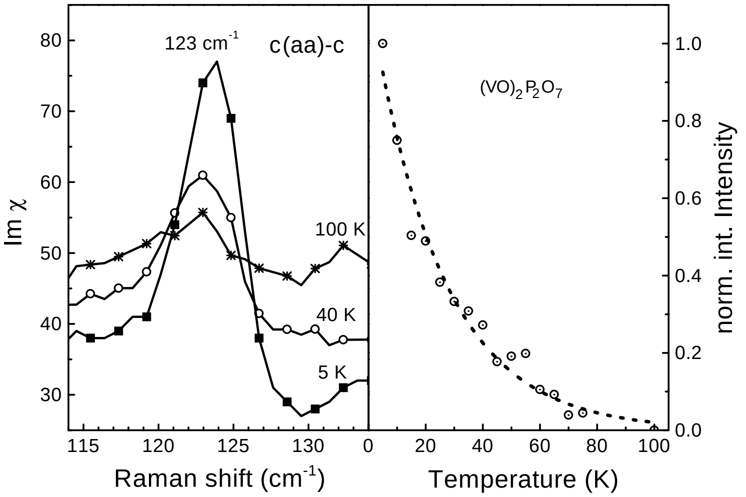

Fig. 2.34. Phonon anomalies in Raman spectra of $(VO)_2P_2O_7$ in interchain (*aa*) polarization in dependence of temperature (left panel). The intensity of the mode at 123 cm^{-1} is shown in the right panel as a function of temperature. The dashed line is a guide to the eye [214].

Strong spin–phonon coupling is also observed as fluctuations of the energy density of the spin system (see Section 5). These are detected as strong quasielastic light scattering and have been used to determine the magnetic contribution to the specific heat. A comparison of these results for VOPO with a DMRG calculation [225] leads to a quantitative agreement supporting strongly the alternating chain model with strong spin–phonon coupling for $(VO)_2P_2O_7$.

Table 2.1
Spin gaps and intrachain exchange interactions of two spin subsystems A and B in $(VO)_2P_2O_7$

Spin subsystem	Δ (K)	J_1 (K)	J_2 (K)	δ
Chain A	68	136	92	0.19
Chain B	35	124	103	0.09

The data are derived from ^{31}P and ^{51}V NMR experiments. The data of the subsystem B correspond to the parameters derived from neutron scattering experiments as explained in the text [220].

As discussed in Section 2.3.2 the existence of a high symmetry phase at elevated pressure and/or temperature may also play an important role in inducing anharmonicity and enhancing spin–phonon coupling. Phonon anomalies in $SrCu_2(BO_3)_2$ have been undoubtedly attributed to a structural phase transition into a centrosymmetric phase for $T > T_c = 395$ K. In $(VO)_2P_2O_7$ a transition into a high pressure phase is observed at a pressure of $P = 3$ GPa and temperatures between 400 and 500 K [127,128]. This transition is certainly related to the observed anomalies. In this scenario it is understandable that the high-pressure phase of $(VO)_2P_2O_7$ does not show evidence for phonon anomalies at low temperatures [226].

The triplet bound state tentatively observed in neutron scattering motivated a detailed NMR study [220] that raised doubts concerning this interpretation. The temperature dependence of ^{31}P and the ^{51}V NMR shows two independent components leading to two different spin gaps. The gaps are determined to be $\Delta^A = 68$ K and $\Delta^B = 35$ K. These data are in excellent agreement with the branches observed in neutron scattering. See Table 2.1 for important parameters that have been derived from these measurements. The NMR data are understandable taking two independent magnetic subsystems with distinct propagating triplet branches into account. The doubling of the gap in the second spin system with respect to the first due to a different chain alternation is therefore proposed to be accidental.

The spin subsystems are associated with two crystallographically inequivalent V chains along the b-axis. The inequivalence is proposed to be based on a very small difference in the V–O–V distances ($\Delta d = 0.02$ Å) [220]. The two branches observed in neutron scattering are therefore the result of a large unit cell (with eight formula units and four chains) with two chain systems, A and B, differing in the alternation of their exchange coupling (see Table 2.1). It is important to notice that the weak ferromagnetic coupling in a-axis direction acts between the same kind of chains. Therefore both chain systems stay decoupled. Furthermore, the larger alternation ($\delta = 0.19$) is identical to the value reported in ESR experiments [221].

2.6. Low-dimensional halides and pnictides

In contrast to oxides, many low-dimensional halides show more or less distinct spin–orbit coupling that enforces the description of their magnetic subsystem as Ising or XXZ-models with either easy-axis or easy-plane anisotropies. We will discuss here only compounds with negligible spin anisotropies. Examples are $KCuF_3$, the $ACuCl_3$ family of compounds, the Haldane system $CsNiCl_3$ and a rare earth compound, Yb_4As_3.

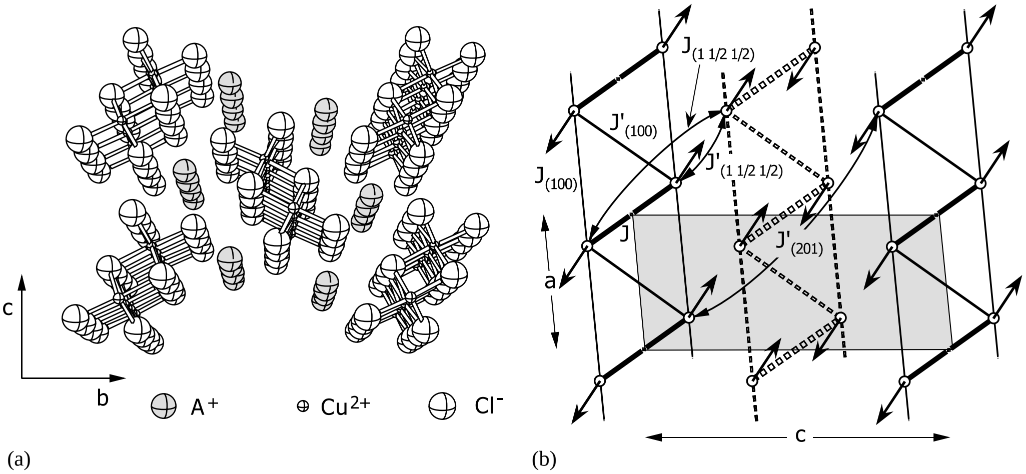

Fig. 2.35. Crystal structure and spin topology of ACuCl$_3$, with A = Tl, K: (a) projection of the crystal structure along the *a*-axis, (b) exchange coupling constants of the three-dimensional dimer topology [232].

2.6.1. The chain system KCuF$_3$

The compound KCuF$_3$ represents a one-dimensional Heisenberg antiferromagnet in the sense of small interchain exchange interactions and negligible spin anisotropies. In spite of the large intrachain exchange coupling $J_{\parallel} = 196$ K, 3D Néel ordering is observed only at $T_N = 39$ K. The specific heat of the spin system shows a maximum at $T = 180$ K due to one-dimensional spin fluctuations [227].

This compound played an important role in the first spectroscopic investigations of the spinon continuum using neutron scattering [228,229]. Experiments were successfully compared to the Müller ansatz, an analytic solution for the two-spinon contribution of the Bethe solution [230]. If no additional interaction, e.g. next nearest neighbor coupling, exists the 1D Heisenberg Hamiltonian commutes with the Raman exchange light scattering operator. Therefore, in light scattering experiments, in contrast to, e.g. CuGeO$_3$, no spinon continuum has been observed. Instead, intrachain polarized quasielastic light scattering has been detected with an intensity $I(T)$ which strongly increases with temperature. This contribution can be described by a correlation function of the magnetic energy density and its fluctuations. (See Section 5 for a detailed discussion.) The renormalized intensity $I(T)/T^2$ has successfully been compared with the magnetic contribution to the specific heat determined by birefringence measurements [227]. In more recent neutron scattering experiments evidence for a longitudinal magnon has been found [231]. This mode is observed in the antiferromagnetically ordered phase of the spin-1/2 quasi-one-dimensional system and signals a crossover from one-dimensional to three-dimensional behavior. Furthermore it indicates a reduction in the ordered spin moment of the spin-1/2 antiferromagnet that has successfully been compared to quantum field theory calculations.

2.6.2. The ACuCl$_3$ family of compounds

The copper halides KCuCl$_3$, TlCuCl$_3$ and NH$_4$CuCl$_3$ share a monoclinic structure with the space group P2$_1$/c. The exchange topology consists of double chains of edge-sharing CuCl$_6$ octahedra running parallel to the crystallographic *a*-axis, which are separated by the cations as shown in Fig. 2.35. The magnetic system has earlier been modelled using 3 coupling constants, describing the intrachain and a frustrating interchain coupling of the system [234]. This chain has been mapped on the exchange topology of a strongly dimerized spin chain with next nearest neighbor exchange interaction [235,236]. Recently, the former two compounds are discussed within a 3D coupled spin dimer model using 6 exchange coupling constants [237–240,232]. While $KCuCl_3$ and $TlCuCl_3$ definitely have a singlet ground state and a spin gap as expected for a dimer system, the appropriate exchange topology and the low-energy model Hamiltonian for NH_4CuCl_3 are still under debate.

In $KCuCl_3$ the triplet dispersion for **k** parallel and perpendicular to the chains is comparable to the smallest gap $\Delta_{01}(\mathbf{k}) = 32$ K of the triplet branch at $\mathbf{k} = (1, 0, 1)$ [237,238,241,242]. The intradimer interaction has been determined to be $J \approx 48$ K. The dimers themselves are weakly 3D coupled with the largest interdimer coupling given by $J_\perp \approx 5.2$ K. The magnetic susceptibility shows a maximum at $T^\chi_{max} = 30$ K and a pronounced drop toward lower temperature. This dependence has been fitted successfully for $T < 15$ K to $\chi(T) \approx (1/\sqrt{T}) \cdot \exp(-\Delta/k_B T)$, with $\Delta = 35$ K [234]. This expression has earlier been derived for antiferromagnetically coupled spin ladders [243]. From recent high field magnetization data coupling constant that are a factor 0.8–0.9 smaller compared to the above given values have been determined for $TlCuCl_3$ [232].

With rising temperature neutron scattering experiments show a flattening and decrease of bandwidth of the triplet branches while keeping the spin gap approximately constant. In addition, a thermally activated broadening of the triplet branch (lifetime $\Gamma \approx \exp(-\Delta_{01}/k_B T)$) and a loss of its intensity is observed for temperatures up to 30 K. These effects are interpreted as an effective diminishing of the interdimer coupling as function of temperature due to thermally induced triplet–triplet interaction or due to spin–phonon interaction [244]. In μSR experiments free electron spins are observed for temperatures down to 6 K, followed by a spin-glass-like slowing down of the dynamics at lower temperatures [245,246].

In $TlCuCl_3$ the maximum in the magnetic susceptibility is observed at $T^\chi_{max} = 38$ K a value similar to $KCuCl_3$. However, neutron scattering experiments resolve a smallest gap of only $\Delta_{01} = 7$ K at $\mathbf{k} = (1, 0, 1)$. An analysis of the triplet dispersion leads to an intradimer interaction $J \approx 60$ K while the interdimer exchange coupling constant $J_\perp \approx 18$ K is a factor 3 larger compared to the respective coupling constant in $KCuCl_3$ [247,239,240]. The much larger bandwidth of the triplet branches compared with the gap is therefore attributed to a breakdown of the weakly coupled dimer model for $TlCuCl_3$ [239]. Treating the interdimer interactions in mean field, the magnetic susceptibility can be modelled by the expression $\chi(T) \approx (\beta/(3 + \exp(\beta J + \beta J'))$ for effective independent dimers, with $\beta = 1/(k_B T)$ and J' the sum of the interdimer interactions. Using this expression the ratio $J/(k_B T^\chi_{max}) = 1.6$ leads to $J + J' = 60$ K in good agreement with the analysis of the neutron scattering experiments [239].

In light scattering experiments on $KCuCl_3$ and $TlCuCl_3$ magnetic continua with energies comparable to the exchange coupling constants are observed. In addition multiphonon scattering intensities with energies above the single phonon frequency spectrum show up [233]. In Fig. 2.36 respective spectra in $TlCuCl_3$ are shown at 4 and 293 K in (aa) and (cc) polarization. The anomalous scattering intensities are only observed in the interdimer (aa) polarization. With increasing temperature the maximum at 46 cm^{-1} in $TlCuCl_3$ shifts to higher energy and is strongly reduced in intensity. In $KCuCl_3$ in addition to the maximum at 56 cm^{-1} a second maximum is observed at elevated temperatures and an energy of 34 cm^{-1}.

For $KCuCl_3$ and $TlCuCl_3$ transitions into gapless 3D ordered magnetic phases are induced by magnetic fields as well-defined cusp-like minima in the magnetization at $H_c = 22.3$ and 5.7 T

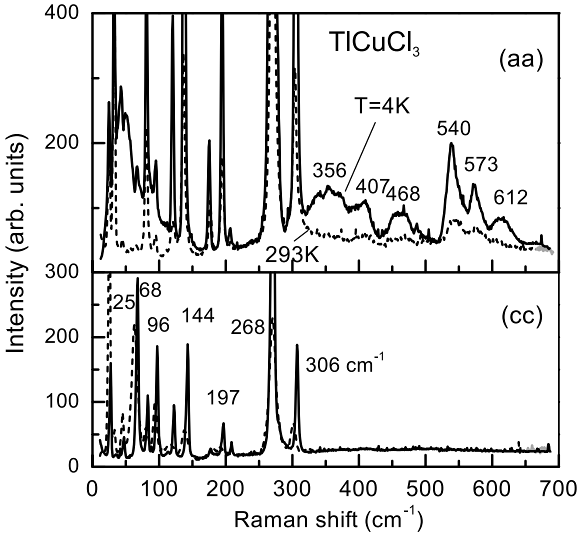

Fig. 2.36. Raman spectra of the spin dimer system TlCuCl$_3$ in (aa) and (cc) polarization. A scattering continuum and several multi-phonon modes are observed in (aa) polarization and at low temperatures (full line) [233].

[247,248,232], respectively. For $H > H_c$ the slope of the magnetization $m(H)$, i.e. the magnetic susceptibility, is finite. These transitions do not depend on the orientation of the magnetic field with respect to the crystallographic axes. Furthermore, the phase lines show an upward curvature towards higher fields for higher temperature. For both systems the field-induced transition has been described as a Bose–Einstein condensation of dilute magnons [249]. This is based on the scaling of the critical temperature with magnetic field, $T_c(h) \propto |h - h_c|^{1/\phi}$, with $\phi = 2.3$ and 2.1, respectively. The description of an isotropic Bose–Einstein system with a Hartree–Fock model would lead to $\phi \approx 3/2$. In the mixed system $(Tl_{1-x}K_x)$CuCl$_3$ with exchange bond randomness, the field-induced magnetic ordering is suppressed [240]. Recent NMR and ultrasonic experiments point to an appreciable lattice distortion and first-order-like character of the transition [250]. The sharp peak observed in the ultrasonic attenuation as function of magnetic field or temperature shows a hysteresis [251].

Finally, NH$_4$CuCl$_3$ is believed to have a magnetic (triplet) ground state in contrast to the singlet ground state of the other two copper halides. This distinction is tentatively attributed to interchain interaction [252]. However, as also supported by the magnetic phase diagram, the triplet ground was proposed to result from the combined effect of interchain interaction and dimerization [16]. In measurements of specific heat evidence for a three-dimensional magnetic ordering with $T_N = 1.3$ K has been found that is suggested to involve only 1/4 of the spins. The remaining spins are proposed to remain in a singlet state. The magnetic entropy at this transition is very small as the magnetic correlations are well-developed at this low temperature [253].

The magnetic phase diagram of NH$_4$CuCl$_3$ is of special interest as it contains gapped phases induced by a magnetic field. These phases originate from quantum effects and not from magnetic anisotropies. The magnetization shows a sequence of five well-defined transitions ($H_c = 5, 12.8, 17.9, 24.7, 29.1$ T) and plateaus at $m = 1/4, 3/4$ and 1, with m per copper site in units of $g\mu_B$ [16,236,252]. For small fields and in between the plateaus the magnetization $M(H)$ increases roughly linear.

In contrast, the magnetization of the spin chain system copper benzoate shows a continuously field-induced gap as a transition-like increase of the magnetization. This gap is related to a staggered magnetization that is again attributed to an alternating g-tensor and a DM interaction [254,255]. In this phase magnetic bound states with energies $E \leqslant 3\ \text{cm}^{-1}$ are theoretically predicted.

Theoretically, the plateaus observed in NH_4CuCl_3 and in some other 1D $s = 1/2$ spin systems correspond to a topologically induced quantization (similar to the quantum hall effect) denoted as a "field-induced Haldane gap" or "triplet–singlet-lattice" phase. They should fulfill the Oshikawa–Yamanaka–Affleck condition $n(s - m) = \text{integer}$, with n the spatial period of the spin ground state (number of spins per unit cell), s the magnitude of the spin and m the magnetization [256]. Recent theoretical studies have shown that in dependence of the coupling parameters plateaus may be observed for $m = 0$ and $1/3$ in three-leg ladders, for $m = 0$ and $1/2$ in two-leg ladders and in frustrated alternating Heisenberg chains [256–259].

Following these arguments the plateau at $m = 1/4$ in NH_4CuCl_3 cannot correspond to a diluted dimer ordering of a frustrated alternating Heisenberg chain as suggested in Ref. [258]. Here, the proposed division of the spin system into a triplet and a singlet portion as evidenced form specific heat data might explain the phase diagram [253]. Recently two other arguments have been used in connection with the complicated behavior of NH_4CuCl_3 in a magnetic field: The up to now ignored orientational transition of the NH_4-tetrahedra at $T_{\text{orient}} = 70$ K [260] may induce an additional modulation of the exchange coupling constants or an enlargement of the unit cell. Furthermore, it has been suggested that a weak coupling of two different ladder topologies may be helpful to suppress a plateau at $m = 1/2$ [261].

2.6.3. The Haldane system $CsNiCl_3$

The Haldane gap of an integer-spin Heisenberg chain is besides dimerization, frustration and ladder topology another route to a gapped excitation spectrum [71,72]. A Haldane gap has first been observed in $CsNiCl_3$, which contains $s = 1$ Ni^{2+} chains [73,262,263]. This compound has exchange coupling constants of $J_{\|} = 16.6$ K and $J_{\perp} = 0.29$ K for intra- and inter-chain exchange respectively. These values and a small easy axis anisotropy of $D = -0.62$ K have been determined for temperatures below $T_N = 4.4$ K using the dispersion of magnon branches in the 3D Néel ordered phase. The observed singlet–triplet gap $\Delta_{01} = 15.4$ K and the 2π-periodicity of the triplet branch in the disordered phase ($T > T_N$: no symmetry of the chain is broken) are solely due to the "hidden order" described by Haldane.

2.6.4. Yb_4As_3

In the mixed-valency and semi-metallic rare earth compound Yb_4As_3, charge ordering ($T_{CO} = 290$ K) leads to $s = 1/2$ Yb^{3+} chains that are only weakly coupled. Charge ordering in a quantum spin system is also realized in NaV_2O_5 and plays a role in $Sr_{14}Cu_{24}O_{41}$. In Yb_4As_3 a very large linear specific heat contribution has been observed at low temperatures [264]. This contribution is related to fermionic spinon excitations on the chains as the carrier concentration is very small for $T < T_{CO}$ [265]. Indeed, in neutron scattering experiments a gapless spinon dispersion has been observed as expected for a $s = 1/2$ Heisenberg chain system with $J_{\|} = 40$ K [266–268]. It has therefore been emphasized that this compound realizes a "novel route" to Heavy Fermion systems [269].

The physical picture of Yb_4As_3 got another twist when inelastic neutron scattering experiments [270] found a gap to (all) magnetic excitations. This gap opens in the presence of an external magnetic field, confirming a prediction [271] by Schmidt et al. based on an interpretation of previous specific heat data [264]. Several proposals have been made in order to explain this unusual behavior [272]. The first model [273] is based on the observation that a staggered DM interaction, which generates an effective staggered g-tensor, is allowed [274,275] in this $4f$-compound. It is known that a staggered g-tensor leads to a gap in an external field [254,255]. The second model [272], based on a mean-field analysis of the anisotropic spin-chain, proposes that a gap opens in the presence of a uniform transversal magnetic field.

Raman light scattering experiments on Yb_4As_3 show quasielastic scattering for intrachain polarization while in crossed polarization a gap-like decrease of the scattering is observed for $\Delta\omega < 100\ \mathrm{cm}^{-1}$ [184]. In addition, multiphonon excitation due to spin–phonon coupling exist. These latter results are comparable to observations in the zig-zag chain compound $SrCuO_2$ and in the chain system Sr_2CuO_3 [276].

2.7. Inorganic systems with spin-Peierls and related instabilities

The Peierls instability of one-dimensional *metals* was introduced by Sir R. Peierls in his textbook "*Quantum Theory of Solids*" [277]. It is based on the divergence of the electronic susceptibility at $\mathbf{k} = 2\mathbf{k}_F$ and the instability to a periodic distortion of the chain. The resulting opening of an energy gap and insulating ground state overcompensates the energy loss due to the lattice distortion [3].

The spin-Peierls transition of one-dimensional *insulating spin systems* is the magnetic analogue of the Peierls transition. The gain of energy results from a dimerization of the spin degrees of freedom. The coupling of the spin to the phonon system leads to the formation of a non-magnetic singlet ground state in a dimerized system. The observation of a singlet–triplet gap in the magnetic excitation spectrum as well as a lattice distortion is a critical proof of this ground state. This transition was first investigated in the 1970s in the organic compounds $(MEM)(TCNQ)_2$ [278] or (TTF)(Cu-BDT) [279,280] and later in charge transfer salts [281]. For an introduction to the phenomenology of the spin-Peierls transition and respective compounds we refer to the review article of Bray [282].

The discovery of a spin-Peierls transition at $T_{SP} = 14.3$ K in $CuGeO_3$ by Hase et al. [283] and of a spin-Peierls like transition (combined with charge ordering) at $T_{SP} = 34$ K in NaV_2O_5 by Isobe et al. [207] opened up a much broader range of experimental methods and investigations. This led to a fruitful extension of this field from both experimental as well as theoretical point of view [284].

The compound $CuGeO_3$ represents a system with considerable relative strength of competing interactions [285,286]. This is due to AF next nearest neighbor exchange interaction along the spin chain (frustration). The later found NaV_2O_5 shows a quarter-filled ladder structure [287] with a dimerization instability that is more complicated due to the interplay of hopping and intersite Coulomb interaction. Both compounds are interesting and important to study. Their properties and magnetic parameters will be discussed in the following.

2.7.1. $CuGeO_3$

The compound $CuGeO_3$ crystallizes in an orthorhombic structure (Pbmm) with the lattice parameters $a = 4.81$ Å, $b = 8.43$ Å, and $c = 2.95$ Å [288]. A classification of the $\mathbf{k} = 0$ vibrational modes can

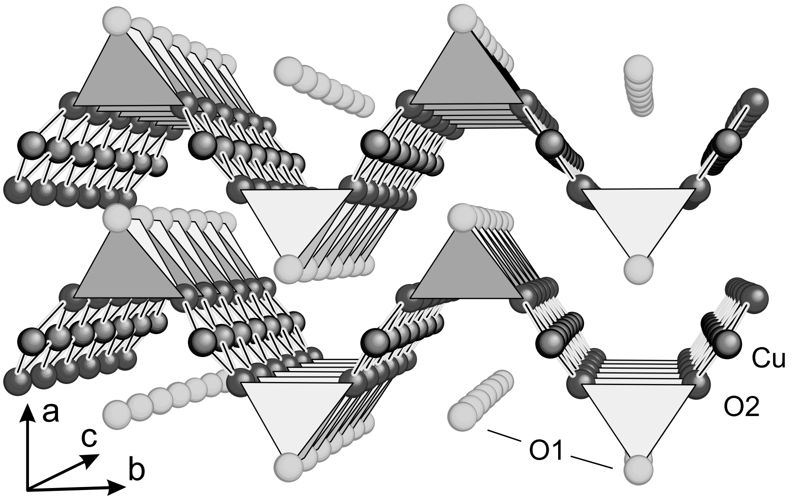

Fig. 2.37. Lattice structure of $CuGeO_3$. The CuO_2 chains are formed by O2 and Cu. The Ge site is hidden within the GeO_4 tetrahedron.

be found in Refs. [289,290]. The compound may be described by ribbons of CuO_2 and GeO_4 chains sharing one oxygen atom (O1) in the *bc*-plane, as shown in Fig. 2.37. The CuO_2 chains (including O2) that are aligned along the *c*-axis provide a superexchange path via a Cu–O–Cu bonding angle very close to 90° [61,291]. This special exchange path leads to a weakening of the nearest neighbor exchange J^c_{nn} compared to, e.g., a 180°-exchange in Sr-cuprates and a considerable strength of the next nearest neighbor exchange J^c_{nnn} along the *c*-axis. This antiferromagnetic exchange to the next nearest neighbor leads to a frustration of the spin system with the frustration parameter $\alpha = J_{\mathrm{nnn}}/J_{\mathrm{nn}}$.

The relevance of frustration is supported by magnetic susceptibility measurements that show a much too broad maximum at $T_m = 60$ K [283] in comparison with the Bonner–Fisher prediction [292] for a Heisenberg spin chain. Considering a finite J^c_{nnn} a much better agreement with experiment is found [293,294]. Using the above mentioned susceptibility data and neutron scattering results [295,296] exchange constants of $J^c_{\mathrm{nn}} = 150$ K, $J^c_{\mathrm{nnn}} = 30$ K with $\alpha = 0.2$ have been found [293,294]. Frustration-induced Raman scattering [97] discussed in Section 3.4 leads to a rough estimate of $J^c_{\mathrm{nn}} = 150$ K and $\alpha = 0.24$ [97] while a careful analysis of susceptibility and magnetostriction data points to a larger frustration and corresponding exchange parameters, $\alpha = 0.35$–0.37 and $J^c_{\mathrm{nn}} = 160$ K, respectively [297,298].

A further origin of frustration in $CuGeO_3$ is the coupling of the spin system to so-called “hot phonons” that have a frequency close to J^c_{nn} [299]. This non-adiabatic coupling adds an effective frustration term to the Hamiltonian of the magnetic subsystem.

Singlet formation and transition-induced modes. A drop in the magnetic susceptibility [283] and the observation of superstructure reflections in X-ray [300,301] or neutron scattering experiments [302] mark the spin-Peierls transition at $T_{\mathrm{SP}} = 14.3$ K. The accompanied lattice distortion has a wave vector $\mathbf{k}_{\mathrm{SP}} = (1/2, 0, 1/2)$. This means a doubling of the lattice cell parameters in *a*- and *c*-axis direction. While this vector describes the new periodicity of the phonon system $\mathbf{k}_{\mathrm{AF}} = (0, 1, 1/2)$ gives the periodicity of the magnetic system. In Fig. 2.38(a) a sketch of the two vectors in the Brillouin

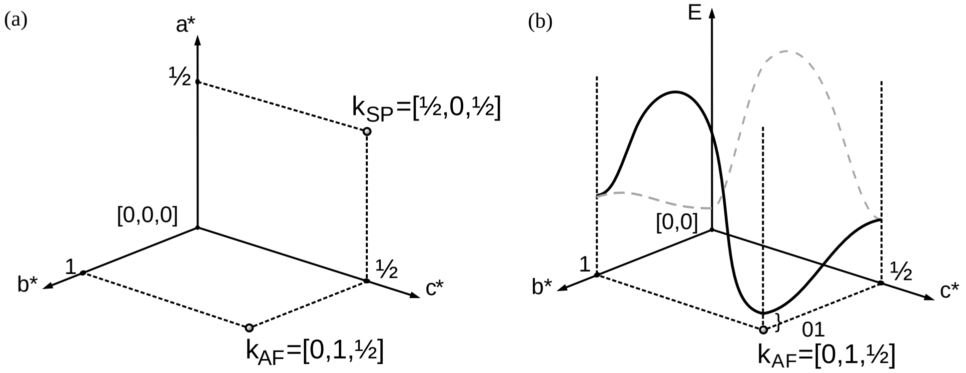

Fig. 2.38. (a) Sketch of the relevant **k**-vectors and (b) the neutron dispersion of the acoustic triplet branch in the dimerized phase of $CuGeO_3$.

zone and in Fig. 2.38(b) the periodicity of the triplet dispersions observed in neutron scattering are shown [303,304]. In $CuGeO_3$ the dimer positions alternate perpendicular to the c-axis direction, i.e. are staggered along the b-axis of the unit cell. This has been concluded from a careful analysis of the intensity of the superstructure reflections [305] and has important consequences for the observation of an incommensurate magnetic phase in an applied magnetic field [16].

The lattice displacements of the atomic positions connected with the spin-Peierls transition may be described as due to an alternating rotation of the GeO_4 tetrahedrons around the Ge atoms or around the O1–O1 axis, which induces displacements of Cu atoms along the c-axis and a twisting of the CuO_2 ribbons around the c-axis. All atomic displacements are smaller than 2×10^{-3} [284,301]. Therefore, the superstructure reflections are very weak in intensity.

There are four constituting phonon modes of the CuO_2 chain dimerization, as shown in Fig. 2.39. A calculation of their microscopic spin–phonon coupling constants is given in Ref. [306]. The modes Ω_1 and Ω_2 have the largest values as they efficiently modulate the Cu–O–Cu bonding angle of the CuO_2 chains. Three of these modes are observable in Raman scattering for temperatures below T_{SP} as they are zone-folded from the high symmetry Brillouin zone boundary $(1/2,0,1/2)$ to the zone center at 107, 370 and 821 cm^{-1} [308]. The fourth mode nearly coincides in frequency with a high-energy cut-off of a density of states at 224 cm^{-1} observed in Raman scattering (see Fig. 3.3). This high-energy cut-off may originate from a two-magnon density of states [309] as it is close to the maximum of the c-axis dispersion of magnon-like triplets observed in neutron scattering [295,296] for temperatures below T_{SP} at $E(1/2,0,1/4)\approx 170\ K = 118\ cm^{-1}$. Due to strong spin–phonon coupling the density of states observed in Raman scattering may also be of mixed spin–phonon origin as it is equally well described by a Fano-like lineshape [310] of a single phonon coupled to a continuum of magnetic excitations.

The soft mode problem. In spite of the enormous experimental effort linked to the spin-Peierls transition in $CuGeO_3$ no anomalous phonon behavior could be detected. It is therefore now well established that especially no phonon soft mode exists close to T_{SP} [291,302,307,311,312]. This peculiarity is not easy to understand as a lattice instability may be based on a macroscopic population of a phonon branch Ω_q^{SP}. This is easy to achieve with $\Omega_q^{SP}\rightarrow 0$ for $T=T_{SP}$.

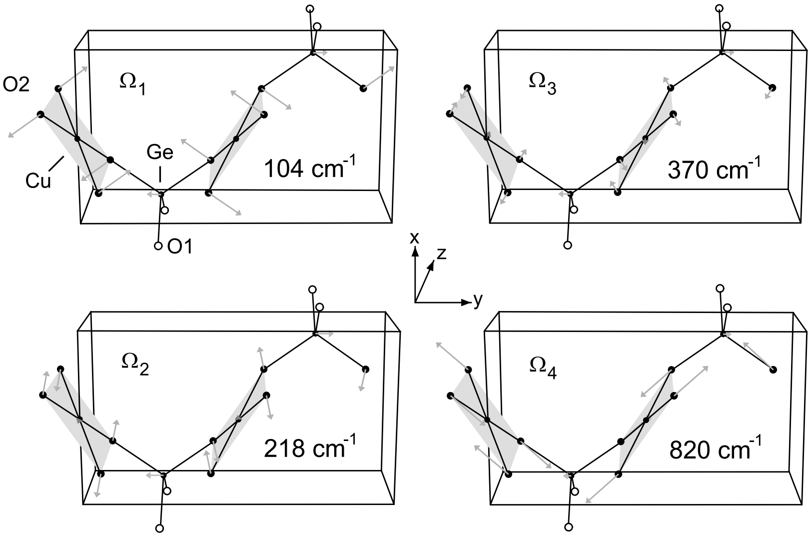

Fig. 2.39. Displacement patterns of the T_2^+ eigenmodes in $CuGeO_3$ involved in the spin-Peierls distortion for $T < T_{SP}$. The shaded areas are the CuO_4 plaquettes which form the Cu chains. The Cu atoms are in the center of each plaquette, the corners are formed by oxygen (O2). The oxygen (O1) are represented by the open circles with the Ge ions in between them. The given frequencies correspond to zone center optical phonons and have been determined by a force constant model to the phonon dispersions [306,307].

The spin-Peierls-induced Raman mode of $CuGeO_3$ at $30\,cm^{-1}$ has been proposed to be the soft mode of this system as its energy as function of temperature scales with the square root of the superstructure reflection intensities observed in elastic neutron and X-ray scattering [313]. However, this mode goes soft approaching the spin-Peierls temperature only from low temperatures. For $T > T_{SP}$ it does not exist. In general, and taking phonons in the adiabatic limit into account, the spin-Peierls transitions of the considered systems have been predicted for arbitrary small spin–phonon interaction [314]. On the other hand, optical phonons in an anti-adiabatic (high frequency) limit lead to a transition only above a critical coupling. It has been suggested that in this limit the mechanism of the transition is different and no soft modes should be observable [299,315]. It has also been proposed that in $CuGeO_3$ the four phonon modes (Ω_1–Ω_4) with T_2^+ symmetry (see Fig. 2.39) involved in the spin-Peierls distortion prevent the observation of a soft mode [307].

In a paper of Gros and Werner following an extended Cross–Fischer approach [314] these problems have been reconciled. Only phonons involved in the lattice instability and with a bare frequency less than a critical value completely soften. Phonons with frequencies $\Omega_q^{SP} > \Delta_{01}$ do not soften but harden slightly in frequency. This effect has indeed been observed experimentally in $CuGeO_3$ for $T \approx T_{SP}$ [316]. The earlier investigated organic spin-Peierls compounds have generally a much softer phonon spectrum and are therefore always in the limit $\Omega_q^{SP} < \Delta_{01}$ with pronounced phonon soft modes [299,317].

The magnetic excitation spectrum. For $T < T_{SP}$ well-defined magnon-like triplet branches develop out of a spinon continuum observed above T_{SP} [318]. Fig. 2.38(b) shows a sketch of the neutron scattering results. They exhibit a 3D dispersion with a **k**-dependent singlet–triplet gap Δ_{01} and a splitting in an applied magnetic field of the expected magnitude ($g \approx 2$) [295,296]. The dispersion of Δ_{01} along the b-axis points to a non-negligible interchain interaction with an exchange coupling $J^b \approx 0.1J^c$. The observation of these well-defined triplet branches on the other hand proves that the spinon excitations definitely change their character with the dimerization of the spin system [29]. The magnon-like modes should now be understood as triplets that consist of bound spinons.

A further binding effect below T_{SP} is observed in the triplet spectrum as a gap of magnitude comparable to Δ_{01} now separating the triplet branch from a continuum of free unbound spinons. The spectral weight of the latter, however, is reduced for $T \leqslant T_{SP}$ [319]. The binding effect on the spinon excitations to form triplets mainly depends on dimerization. However, magnetic and magnetoelastic interchain interaction [32] and frustration [29] are also important factors, as will be discussed in Section 4.

Taking the available neutron scattering data [295,319,320] and the **k**-vectors $\mathbf{k}^{\Gamma} = (0,0,0), \mathbf{k}_{SP} = (1/2,0,1/2)$, and $\mathbf{k}_{AF}{=}(0,1,1/2)$ illustrated in Fig. 2.38, the singlet–triplet gap of $CuGeO_3$ at the high symmetry points has the following values: $\Delta_{01}^{\Gamma} = 24$–$30\ \mathrm{K} = \Delta_{01}^{\mathbf{k}_{AF}}$ and $\Delta_{01}^{\mathbf{k}_{SP}} = 65$ K. ESR-experiments [321] on thermally excited transitions in the Zeeman-split triplet branch ($H \neq 0$) observe a gap with a size similar to $\Delta_{01}^{\mathbf{k}_{AF}}$, while infrared absorption experiments [322] observe a gap comparable to the size of $\Delta_{01}^{\mathbf{k}_{SP}}$. Theoretical 1D models neglect the magnon-dispersion perpendicular to the chain along c, the spin-Peierls gap of theoretical 1D models need therefore to be identified with the average gap $(\Delta_{01}^{\Gamma} + \Delta_{01}^{\mathbf{k}_{SP}})/2 = 4\ \mathrm{meV} = 46.4$ K. The reduced gap ratio $2\Delta_{01}^{\Gamma}/k_B T_{SP} = 3.4$ is close to the weak coupling "BCS"-value.

Evidence for Dzyaloshinskii–Moriya interaction. This inconsistency is based on an anisotropy of the spin interaction that manifests itself most directly in a second optical triplet branch observed only recently in neutron scattering experiments [323]. The second branch has a considerable spectral weight in the whole Brillouin zone and may be constructed by folding the so-far known acoustic triplet branch along the b- and c-axis about the middle of the Brillouin zone. It may originate from an additional and so far not considered antisymmetric part of the exchange Hamiltonian, e.g., a DM interaction [324,325]. The DM interaction is compatible with the absence of an inversion center in between two copper sites along the b-axis direction of $CuGeO_3$. Deviations from the assumed centrosymmetric Pbmm structure have been observed in Raman scattering [326] and X-ray scattering experiments, and have been discussed in this context [324]. Also ESR experiments point into the same direction [327].

In X-ray scattering experiments unexpected superstructure reflections compatible with the point group $P2_12_12$ have been found in carefully annealed single crystals. This proposal corresponds to a superstructure with a non-centrosymmetric copper site in the unit cell $2a_p \cdot b_p \cdot 4c_p$, with $a_p \cdot b_p \cdot c_p$ the pseudo-unit cell of the Pbmm structure. This superstructure is based on a coherent arrangement of differently distorted CuO_6 octahedra along the c-axis. It can only be verified experimentally if the corresponding structural coherence length is large enough [325].

The singlet bound state. In inelastic light scattering experiments gap excitations are visible due to frustration-induced exchange light scattering [97]. Similar to the usual two-magnon scattering in 3D antiferromagnets combining two magnons with opposite **k**, in $CuGeO_3$ a singlet bound state of two strongly interacting triplet states is formed. This bound state shows in contrast to spin–orbit coupling-induced one-magnon scattering no splitting in an applied magnetic field [313] and defines the singlet–singlet gap as $\Delta_{00} = 30\ \mathrm{cm}^{-1} = 43.2$ K. The energy of this singlet corresponds to $2\Delta_{01}^{\Gamma}$ renormalized to lower energy by a binding energy of the triplets [328]. Following calculations of Bouzerar et al. [29] the energy and spectral weight of this singlet bound state strongly support an

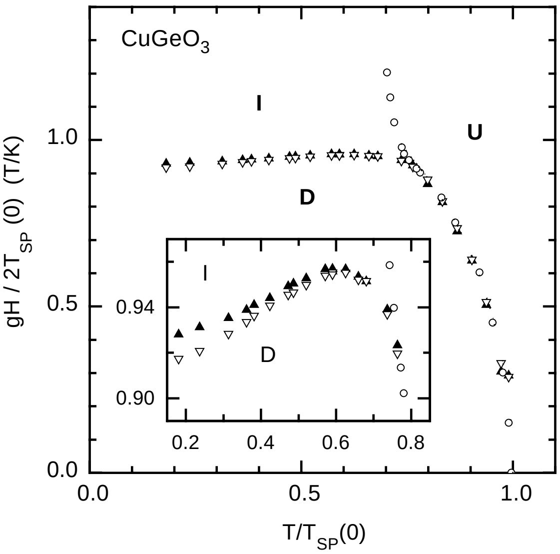

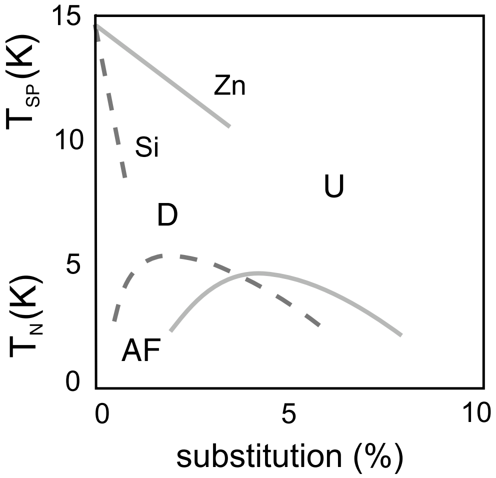

Fig. 2.40. Magnetic-field vs. temperature phase diagram of $CuGeO_3$ on a reduced scale showing the uniform (**U**), the dimerized spin-Peierls (**D**) and the magnetic field-induced incommensurate phase (**I**). The inset shows the hysteresis at the **D**/**I** phase boundary observed in magnetostriction experiments [329].

Fig. 2.41. Schematic phase diagram of substituted $CuGeO_3$ with the uniform (**U**), dimerized spin-Peierls (**D**), and 3D antiferromagnetic phase (**AF**). The solid and the dashed lines give the phase boundaries for Zn and Si substituted samples, respectively.

exchange constant of $J^c_{\mathrm{nn}} = 150$ K and a frustration parameter $\alpha = 0.24$. A further discussion of the properties of magnetic bound states is given in Section 4.

The incommensurate phase in a magnetic field. Applying a magnetic field at low temperatures a first-order transition to an incommensurate (**I**) magnetic phase is observed. The tricritical point is at $T_c = 11$ K and $H_c = 12.25$ T [330]. The phase diagram including the uniform (**U**), the dimerized (**D**) spin-Peierls, and the magnetic phase is shown in Fig. 2.40 [329]. The lattice distortion in the **I** phase is described by a soliton-like lattice close to the **D**/**I** phase boundary with a continuous change to a sinusoidal distortion at higher fields. Further aspects of the **I** phase are discussed in Refs. [68–70,322,329].

Substitutions and long-range AF order. A very fascinating aspect of this compound is the possibility of substitutions. Several extensive studies of substitution effects of transition metals on the copper site (Ni [331–333], Co [334], Mg [335], Zn [328,336–341]) and Si on the Ge site [57,328,338,340,342–344] have been performed and summarized in Refs. [58,333,345,346]. With a few percent of substitutions the spin-Peierls transition is suppressed drastically and finally disappears. On the contrary, in the magnetic susceptibility a Curie–Weiss contribution proportional to the defect concentration is observed. At lower temperature and even for very small substitution levels long-range AF ordering is induced ($T_N \leqslant 5$ K) with the easy axis along the crystallographic c-axis. For small x this order is in coexistence with the dimerization [339]. For higher concentration levels the superstructure peaks corresponding to the spin-Peierls phase exhibit increasing disorder. Finally the magnetic ordering disappears again as shown in Fig. 2.41.

Applying hydrostatic pressure the decrease of the singlet–triplet gap and T_{SP} can partially be undone. This is caused by an increasing frustration α with pressure that localizes the triplet excitations and restricts the suppression of the order parameter to a smaller region near the impurity [306,348]. There exists no critical concentration for the observation of long-range order with Zn substitution. In carefully prepared single crystals of $Cu_{1x}Zn_xGeO_3$ with $x \leqslant 5 \times 10^{-3}$ a minimum Néel temperature of 0.0285 K has been observed. This indicates that the dimerization sustains the coherence of the antiferromagnetic phase of the spin polarization in impurity-doped systems and is consistent with the theory of the impurity-doped spin-Peierls systems [347].

In contrast for Mg and Ni substitution a first-order transition from a dimerized AF to a pure homogeneous AF is observed with a critical concentration of x_c=0.02 [335,332]. At this concentration T_{SP} is zero and T_N jumps to a higher value.

The occurrence of 3D long-range magnetic order in a quasi-one-dimensional system may be explained in the simple picture of cut chain segments that weight the interchain interactions stronger than in the infinite chain. However, this argument would not explain why this ordering disappears again at higher concentration levels. On the other hand magnetic ordering due to disorder is a phenomenon observed in geometrically frustrated spin systems [285,349]. A proper theoretical description of this behavior has to include that even a very small substitution level in a spin chain drastically changes its excitation spectrum. In a dimerized, non-perturbed system a gapped state with exponentially decaying spin–spin correlations is realized. A local substitution or disorder induces algebraically decaying spin–spin correlations as a transition to a quantum critical state. This transition is described as a quantum critical point. Strongly simplifying, the observed Néel ordering results from a shift of this quantum critical point from $T = 0$ to finite temperature due to interchain interaction [39,42].

Theoretical studies of non-magnetic impurities in spin chains and ladders found general interest as a step toward understanding the effect of doping mobile carriers in quantum spin systems [37–42]. Earlier Monte Carlo studies showed an enhanced four-spin susceptibility and therefore an enhancement of the spin-Peierls instability in random or disordered spin chains [350,351]. Non-magnetic impurities in strongly dimerized spin chains create loose $s = 1/2$ spins which randomly introduce states within the magnetic excitation gap. These states should be observable as low-energy excitations (doped spinons) that form a weakly dispersing impurity branch inside the gap. For smaller dimerization many-body $s = 1/2$ states are spread over several lattice spacings enhancing the spin–spin correlation at short distances [39,42]. The above mentioned scenario has been discussed to explain substitution-induced Néel ordering in the spin ladder $Sr(Cu,Zn)_2O_3$ (Section 2.4.1) and in $CuGeO_3$.

Enhanced short-range dimer fluctuations [37] have also been studied in Zn as well as Si substituted $CuGeO_3$ using Raman scattering of a dimerization-induced phonon mode at 370 cm^{-1} and neutron scattering of the superstructure reflections [328,339,341,352]. The intensity of the phonon mode at 370 cm^{-1} as function of (decreasing) temperature shows an increase for $T \lessapprox T_{SP}$. This has been investigated in a Zn-substitution study (x=0) depicted in Fig. 2.42 [328]. With finite substitution level the maximum intensity of this mode is suppressed. In samples that do not show a thermodynamic phase transition ($x = 0.06$), however, the intensity stays finite. Its onset shifts to higher temperature with increasing substitution levels. As for $x = 0.06$ an onset of the dimerization-induced mode at

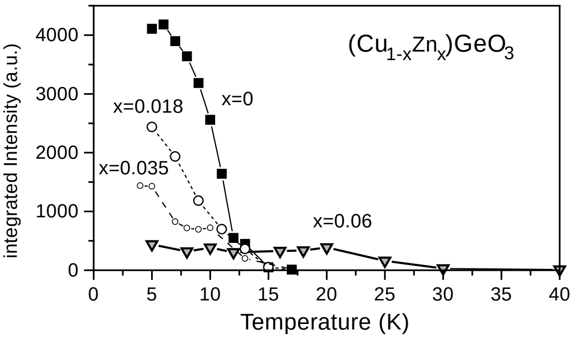

Fig. 2.42. Effect of Zn substitution in CuGeO$_3$ on the intensity of a dimerization-induced phonon mode at 370 cm^{-1} [328].

$T_{\rm onset} \approx 25$ K is observed, i.e. at a temperature above the spin-Peierls temperature of the pure samples, this shift is understood as a fingerprint of locally enhanced dimer fluctuations. Similar but more pronounced effects have been observed in Si-substituted samples. In consistency with X-ray studies Si substitution on the germanium site induces lattice strains and enhances drastically the amount of disorder in the lattice cell [328,344].

A further effect of substitutions is the introduction of defect-induced bound states in the singlet–triplet gap of the excitation spectrum. This has been observed in light scattering spectra of CuGeO$_3$ as a well-defined mode at about half the energy of the singlet bound state of the pure samples as described in Section 4.1.2 [32,36,353].

Concluding the discussion of the magnetic parameters and properties, it should be obvious that CuGeO$_3$ is not an ideal representative of a spin-Peierls system. Especially the deviations of the spin system from the Heisenberg Hamiltonian, i.e. a non-negligible interchain interaction and intrachain frustration, evidence for a DM interaction and the complicated spin–phonon coupling prevent its closed-up and unambiguous description within a set of a few parameters.

2.7.2. NaV$_2$O$_5$

The compound NaV$_2$O$_5$ shows a phase transition at $T_{\rm SP} = 35$ K with combined spin-Peierls and charge-ordering characteristics [207,208]. It is formed by edge-sharing VO$_5$ square pyramids in the *ab* plane separated by chains of sodium ions located between the *ab* layers. If the superexchange via the oxygen square pyramids along the *b*-axis is taken as the dominant exchange path, the compound may be understood as an arrangement of weakly coupled (90° exchange) ladders. As only one electron (spin) per two vanadium sites is available the ladders are quarter-filled [287].

A complete charge ordering on a linear chain of V^{4+} ($s = 1/2$) and a chain of V^{5+} ($s = 0$) with distinguishable vanadium sites leads to the earlier reported non-centrosymmetric Pmn2$_1$ structure [205]. However, this is in disagreement with structural investigations at room temperature using synchrotron X-ray diffraction, neutron scattering [209], and also with recent NMR experiments [354,355]. Presently a centrosymmetric structure Pmnm is used for the high-temperature phase [209], shown in Fig. 2.43.

In NMR experiments for temperatures above $T_{\rm SP}$ only one vanadium site is observed whereas below $T_{\rm SP}$ two sites are resolved. The structure of the low-temperature phase is under discussion.

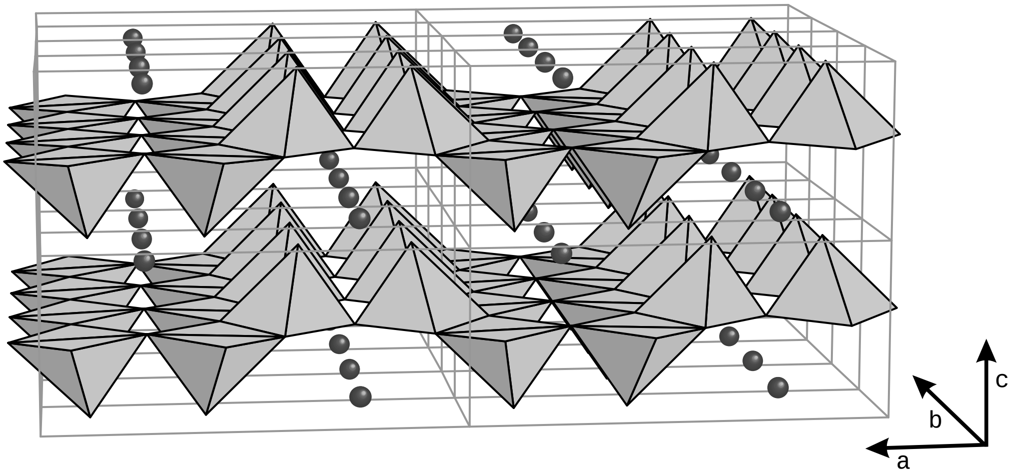

Fig. 2.43. Lattice structure of NaV_2O_5. A ladder along the *b*-axis is formed by two rows with mixed $V^{4.5+}O_5$ square pyramids that share corners. This ladder is only weakly coupled to a neighboring ladder as corresponding V-ions are shifted by half a unit cell. These pyramids share edges. The site of vanadium (omitted here) is in the basal plane center of each pyramid and slightly shifted towards the respective apical oxygen. The rows of black spheres denote sodium chains.

The acentric Fmm2 point group or one of its subgroups are proposed [355,356]. The Fmm2 point group is built by an alternation of non-distorted and distorted, charge ordered chains. A corresponding $V^{4.5}$-site, however, is not observed in NMR [354,355,357]. A similar structure has been investigated theoretically in the more general context of a coexisting charge-density wave and spin-Peierls order [358]. Van Smaalen et al. have proposed [359] that stacking disorder in the low-temperature phase of α'-NaV_2O_5 of plane with only zig-zag charge ordering, as illustrated in Fig. 2.49, may lead to an average space group Fmm2, as observed by X-ray. This route would then reconcile the various experimental results discussed above, in particular the transverse magnon splitting observed by neutron scattering [360].

Symmetry analysis and room temperature Raman spectra. At room temperature the $\mathbf{k}=0$ vibrational modes of NaV_2O_5 with the space group Pmnm (D_{2h}^{13}) can be classified [189]:

$$\Gamma_{\text{vib}} = 8A_g \oplus 3B_{1g} \oplus 8B_{2g} \oplus 5B_{3g}$$

$$3A_u \oplus 7B_{1u} \oplus 4B_{2u} \oplus 7B_{3u} \ ,$$

where the *even* modes are Raman active and the *odd B* modes are infrared active. For the space group $Pmn2_1$ (C_{2v}^7) with two distinguishable crystallographic vanadium sites the result is [361]:

$$\Gamma_{\text{vib}} = 15A_1 \oplus 8A_2 \oplus 7B_1 \oplus 15B_2 \ .$$

Room temperature Raman spectra of NaV_2O_5 for interladder (*cc*) polarization and all light scattering polarizations accessible in the *ab* plane are shown in Fig. 2.44 [189,362]. The experiments in the temperature range from room temperature to T_{SP} are clearly incompatible with the space group $Pmn2_1$ and confirm the proposed centrosymmetric space group Pmnm, which exhibits one vanadium site. However, in these spectra some other unusual features exist. There is quasielastic scattered light

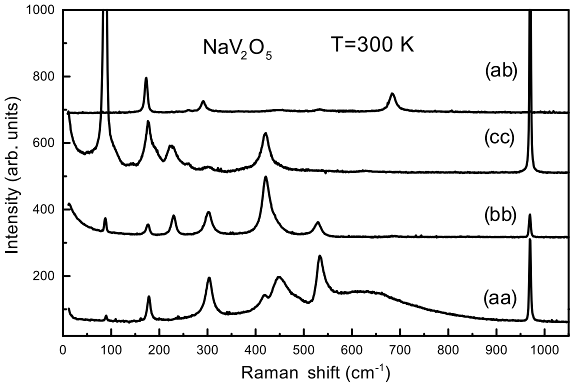

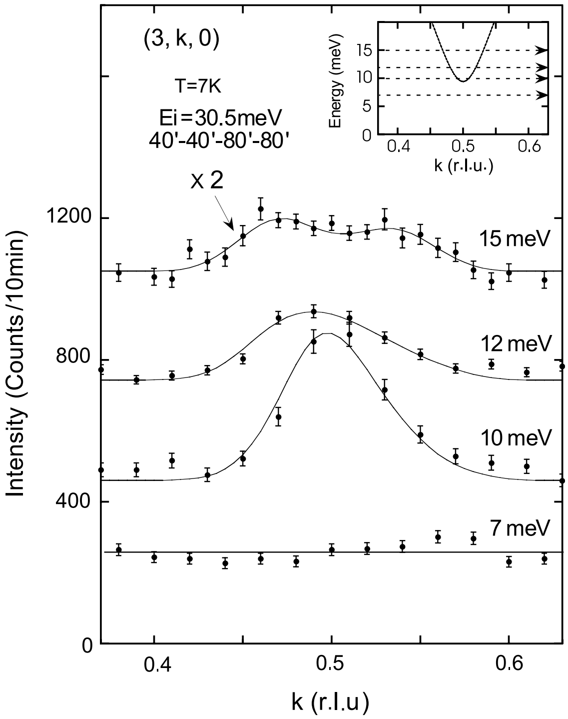

Fig. 2.44. Room temperature Raman light scattering spectra of NaV$_2$O$_5$ for interladder (*cc*) polarization and all light scattering polarizations accessible in the *ab* plane. The broadened central peak in (*cc*) polarization is due to the experimental setup [189,362].

Fig. 2.45. Triplet dispersion in NaV$_2$O$_5$ along the *b*-axis determined by neutron scattering. The points mark the results of $(3, \mathbf{k}, 0)$-scan profiles with fixed energy transfer. The solid lines are resolution convoluted fits. The corresponding dispersion is shown in the inset [373].

in intraladder (*bb*) scattering configuration, i.e. with the polarization of the incident and scattered light along the effective chain direction. This scattering is not observed in other polarizations. It vanishes upon cooling the sample below $T = 100$ K. In other quantum spin systems a comparable scattering contribution has been observed and attributed to fluctuations of the magnetic energy density. This will be discussed further in Section 5. The broad maximum observed in (*aa*) polarization at 640 cm^{-1} has been discussed in the context of light scattering on charge kinks [363]. A second transition-induced quasielastic light scattering contribution in crossed (*ab*) polarization will be described below.

Magnetic properties and the singlet ground state. In magnetic susceptibility measurements a broad maximum in $\chi(T)$ is observed at $T_m \approx 300$ K. This temperature dependence is in agreement with the Bonner–Fisher prediction for a dominant 1D exchange path ($J_{\mathrm{nn}} = 560$ K) [207]. Band structure calculations for a quarter-filled ladder show that the spin degrees of freedom involve effective orbital spins of two neighboring V sites on the ladder. These orbital spins indeed form an effective spin chain with respect to the low-energy excitations as the corresponding charge transfer gap is estimated to be $\varDelta_{\mathrm{CT}} \approx 0.7$ eV [287]. The interchain coupling in this effective spin model is very weak. Therefore, no effect of frustration on the magnetic susceptibility is observed [364]. A detailed discussion of the electronic structure of $\mathrm{NaV_2O_5}$ will be given below.

The singlet formation at T_{SP}=34 K is detected by an exponential drop in the magnetic susceptibility comparable to $\mathrm{CuGeO_3}$. The observation of superstructure peaks in X-ray scattering and zone-folded phonon modes in Raman scattering prove a lattice dimerization with a propagation vector $\mathbf{k}_{\mathrm{SP}} = (1/2, 1/2, 1/4)$, i.e. an increase of the volume of the unit cell by a factor of 16 [208,365–367]. The spin-Peierls nature of the dimerization transition, however, is questionable due to several arguments and experimental findings discussed below, e.g., the very small magnetic field dependence of the transition temperature and the substantial entropy release at T_{SP} [368].

The singlet–triplet gap is estimated using specific heat: $\varDelta_{01} = 67$ and 84 K [369,370], magnetic susceptibility: 85 K [208], ESR: 93.5 K [371], and NMR: 98 and 108 K [357,354]. In recent ESR experiments a magnetic field-induced peak splitting ($g = 1.97$) has been observed, confirming the triplet nature of the excited state [372].

Neutron scattering results and the triplet dispersion. In neutron scattering experiments on powder samples a broad maximum at the energy 115 K is observed as well as hints for dynamic 2D spin correlations [365]. More recent investigations on single crystals confirm $\varDelta_{01}^{\mathbf{k}_{\mathrm{AF}}} = 115$ K, with $\mathbf{k}_{\mathrm{AF}} = (h, 1/2, 0)$ and $h =$ integer. In addition, a steep dispersion of the triplet branch in b-axis direction and a negligible dispersion along the c-axis is detected [373,374]. This determines unambiguously the b-axis as the dominant exchange path direction. Fig. 2.45 shows corresponding scans in $\mathbf{k}$ space at various fixed energies identifying the gap and the steep dispersion [373].

In a-axis direction the dispersion is distinctively smaller. This branch is degenerate at $\mathbf{k}_{\mathrm{AF}}$ and shows an unexpected splitting in the middle of the Brillouin zone. This leads to two singlet–triplet gaps, $\varDelta_a^{h,1/2,0} = 89$ K and $\varDelta_b^{h,1/2,0} = 130$ K, with $h =$ half-integer. In addition, the form factor of this branch has an unusual intensity modulation with h. It changes with the periodicity of 3 reciprocal lattice units [373,374]. A comparable splitting has not been observed in $\mathrm{CuGeO_3}$. Therefore, a simple explanation due to a cell doubling-induced folding of the unit cell in a-axis direction may be excluded. As discussed below, it is compatible [360] with a zig-zag charge ordering of the $2V^{4.5+} \rightarrow V^{4+} + V^{5+}$. Fig. 2.46 shows the corresponding neutron scattering results in dependence on $\mathbf{k}$ [374].

Nature of the transition. There are further experimental observations in $\mathrm{NaV_2O_5}$ that differ from the usual spin-Peierls picture and point toward a charge ordering preceding or accompanying the lattice distortion [375]. The intensity of the superstructure reflections [365] shows a poor agreement with the Cross–Fisher relation [314] $\varDelta_{01} \propto \delta^{2/3}$. Furthermore, the entropy involved with the transition at $T_{\mathrm{SP}} = 34$ K and the value of the reduced gap $2\varDelta_{01}/k_{\mathrm{B}}T_{\mathrm{SP}} = 4.8$–$6.6$ K are much larger compared to $\mathrm{CuGeO_3}$. A conventional spin-Peierls mechanism can also be excluded in view of the very small magnetic field dependence of $T_{\mathrm{SP}}(H)$ [369]. There exists even evidence for an additional first-order transition slightly below T_{SP} from thermal expansion experiments [370]. This additional transition at $T = 33$ K has been interpreted as a charge ordering transition since in NMR experiments two V sites are observed for $T < T_{\mathrm{SP}}$ [354]. Later however, this assignment has been criticized and the anomaly has been attributed to a possible phase separation [375].

Ohwada et al. have studied the nature of the transition under pressure of up to 1.3 GPa and found a “devil’s staircase” of crystallographic transitions [376], which could be modelled accurately by the ANNI-model [377]. The occurrence of the devil’s staircase, see Fig. 2.47, has important implications

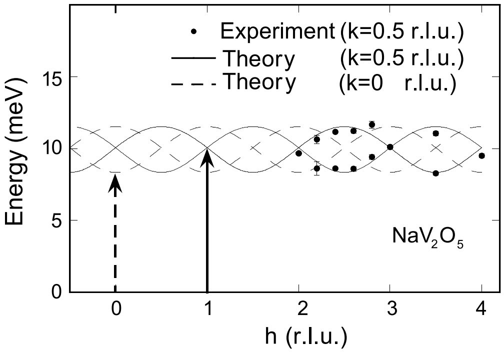

Fig. 2.46. Triplet dispersion in NaV$_2$O$_5$ along the a-axis determined by neutron scattering (full dots). The solid and broken line indicate the calculated dispersions based on a zig-zag charge ordered ground state for $\mathbf{k} = 0.5$ and $\mathbf{k} = 0$ r.l.u., respectively. The solid and broken arrows correspond to possible transitions in neutron scattering and ESR experiments, respectively [373].

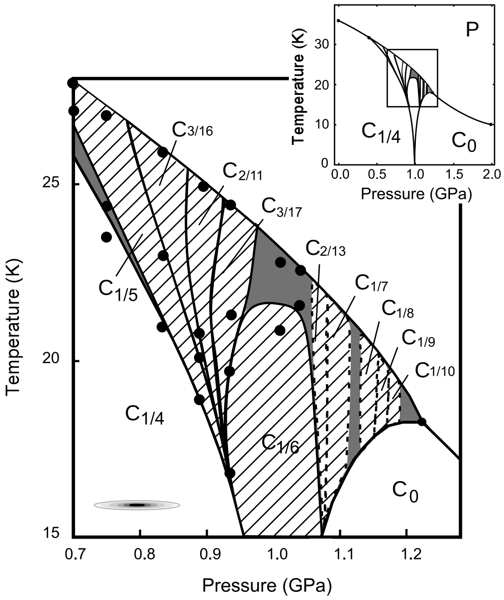

Fig. 2.47. Devil's staircase of crystallographic transitions for NaV$_2$O$_5$ with different ordering pattern C$_{\mathrm{p/q}}$ along the c-direction [376].

for the microscopic description of the underlying crystallographic transitions [376]. Assuming that these crystallographic transitions are driven by different charge-ordering patterns along c, the analysis via the ANNI-model implies in-plane and inter-plane effective coupling constants of the order of 30–40 K. Since the screened V–V Coulomb matrix-elements are of order 0.3–0.4 eV [378], it follows that the effective couplings driving the transition must contain magnetic or elastic components and the assumption [375,379,380] that the Coulomb interaction drives the transition at $T_{\mathrm{SP}} = 34$ K is questionable because T_{SP} is much smaller than the V–V Coulomb matrix-elements.

Microscopic properties of the room-temperature state. The electronic state at room temperature has been studied intensively [287,364,381] and gives a clue towards possible scenarios for the dimerization transition in NaV$_2$O$_5$. The contributions to the electronic Hamiltonian are illustrated in Fig. 2.48 [287,381]. It contains a rung-hopping $t_a \approx -0.35$ eV and two inter-rang hoppings t_b and t_d along the ladder. In the first DFT-analysis t_d was neglected and t_b was found to be ≈ -0.175 eV. Effectively only the combined hopping amplitude $t_b + t_d = -0.175$ eV can be determined from the bands at the Fermi-edge, the anti-bonding bands above the Fermi-edge can be described better [381] assuming a substantial $t_d = -0.12$ eV. The occurrence of a large diagonal hopping t_d opens the possibility of diagonal dimer formation in the low-T phase. The interladder couplings t_1 and t_2 are small and do not influence the character of the charge excitations [382].

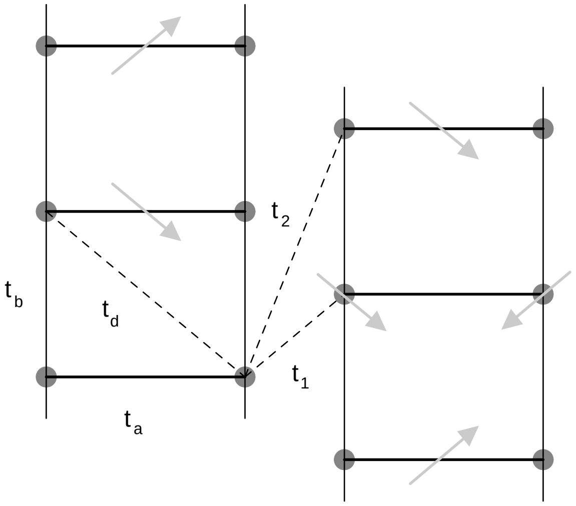

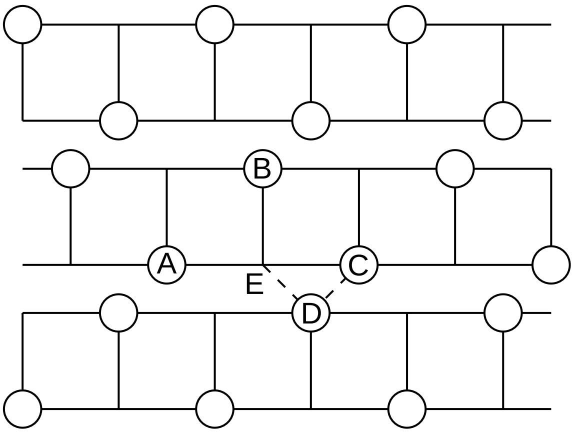

Fig. 2.48. Tight-binding parameters for NaV_2O_5 in the room-temperature state. Note that there is a certain freedom in dividing the effective hopping along the ladder, $t_b + t_d = -0.175$ eV into the leg-hopping $t_b \approx -0.055$ eV and the diagonal part $t_d \approx -0.12$ eV. The other parameters are $t_a \approx -0.375$ eV with t_1 and t_2 being small. One arrow on a V–V rung denotes a spin-1/2 moment, the rungs with two/zero spin illustrate a possible charge-transfer excitation. Another common notation is $t_\perp = t_a$ and $t_\parallel = t_b$ [287,381].

Fig. 2.49. Diagonal zig-zag charge ordering in NaV_2O_5 showing the inequivalence of neighboring pairs of V sites (AB and BC) due to the difference in the V^{4+} occupation (marked as circles) in neighboring ladders. The lines denote t_a and t_b in the ladder while the dashed line marks t_1 (compare Fig. 2.48). Note that the hopping matrix elements ED and DC are in general different [360].

The DFT-estimate [287] for the onsite Hubbard-U of $U \approx 2.8$ eV has been confirmed by cluster-analysis of resonant inelastic X-ray scattering results [383]. The screened V–V Coulomb matrix-elements are of the same order of magnitude [378,384] 0.3–0.8 eV as the hopping-matrix elements, but the effective Coulomb rung–rung interaction has been shown [378] to be reduced by a factor $1 - 1/\sqrt{2} \approx 0.3$. It is therefore to be expected, like in LiV_2O_5 (see discussion further below), that the degree of charge ordering in the low-T phase is less than complete [203].

Please note that in this model the transition temperature $T_{SP} = 34\,K = 2.93$ meV is small in comparison with the above given parameters. It is therefore still under discussion whether interladder frustration [375] is responsible for the reduction of the transition temperature. The effectively one-dimensional spin structure of NaV_2O_5 is caused by the occupation of a bonding state of a rung by one electron with the energy $-t_a$. Considering the strong on-site Coulomb repulsion the cost for an electron transfer to the next rung is at least $\Delta_{CT} = 2t_a$ (see Fig. 2.48 for an illustration).

Nature of the charge ordering in the low-temperature state. Charge ordering phenomena and other instabilities like spin density wave transitions or transitions to commensurate or incommensurate antiferromagnetic ground states are a general property of quarter-filled quasi-one-dimensional systems [358,379,385]. Especially charge disproportionation as observed in many organic conductors (charge transfer salts with metallic countercations) is driven by intersite Coulomb interaction [386].

The energetically preferred ground state configuration is a zig-zag charge ordering with dimers diagonal to the ladder. This configuration minimizes the intraladder Coulomb energy and takes contributions due to lattice distortions in the *ab* plane of NaV_2O_5 into account [375,379,380]. Fig. 2.49 shows a sketch of zig-zag charge ordering. This type of charge ordering has been predicted [360] from an analysis of the splitting of the neutron triplet branch in *a*-axis direction and has been confirmed by subsequent X-ray analysis studies [359].

Possible consequences resulting from the zig-zag charge ordering shown in Fig. 2.49 are [375]:

- The charge transfer gap may be increased to $\Delta_{CT} \approx U_1$, with U_1 the next nearest neighbor (intersite) Coulomb repulsion inside ladders [360,375]. An electronically driven transition has been predicted to occur [387] for $U_1 > 2t_\perp$ but not found in direct diagonalization-studies [388] for $U_1 \approx 2t_\perp$.
- The effective spin-exchange coupling J_b along the ladder is reduced. This effect is experimentally observed comparing the coupling constants from fits to magnetic susceptibility for $T > T_{SP}$ (560 K) with $T < T_{SP}$ (440 K) [360,381].
- An alternation of this coupling along the ladder and thereby the opening of the singlet–triplet gap may be induced by the inequivalence of the sites (see Fig. 2.49 [375]). The formation of diagonal singlets or dimers either as interladder or intraladder singlets is discussed controversially [375,379].
- The larger V^{4+} pushes out neighboring oxygen and thereby stabilizes an occupation of the neighboring plaquettes with the smaller V^{4+}. These in-plane lattice distortions considerably stabilize the charge ordering [360,375].
- kink-like excitations coupled to the lattice can appear in Raman scattering [363]

Pretransitional fluctuations. The existence of an apical oxygen in NaV_2O_5 is additionally noteworthy as it leads to an enhancement of electronic intersite correlations [188]. The asymmetry of the elementary cell with the apical oxygen of the VO_5-pyramid either above or below the V site and a relatively small distance of this oxygen to the V ($d_a \approx 1.61$ Å) lead to a large Coulomb field at the V sites. As a result a charge redistribution between the V ions is followed by a lattice displacement (see Fig. 2.50). Realized in an out-of-phase vibration of the V ions within one rung this displacement couples the bonding and antibonding states discussed above as an origin of the effective chain (their energy separation is $2t_\perp$). In the charge ordered state the Coulomb force contribution of this displacement feeds back to the charge disproportionation, thereby stabilizing it. In other words, the field of the apical oxygen enhances the asymmetry of the V ions arising due to correlations and modulates the effective exchange coupling. Estimates show that strong phonon-driven charge and spin fluctuations are expected as well as the appearance of a new Raman-active mode [188].

In $CuGeO_3$ only few hints exist [389,390] for dimer or structural fluctuations far above the spin-Peierls transition. This is related to the fact that its transition is governed by long-range magnetoelastic interactions leading to a mean-field like behavior. However, in NaV_2O_5 the case is different as in quarter-filled systems the influence of intersite Coulomb interaction is stronger. Therefore, the experimental evidence for pretransitional fluctuations or charge ordering, that will be discussed now, should be taken very seriously. This evidence is found both in thermodynamic as well as in spectroscopic data: A longitudinal mode of the sound velocity shows a transition-related anomaly that persists in a temperature range $0.8T_{SP} \leqslant T \leqslant 2T_{SP}$ [391,392]. In IR absorption a transition-induced

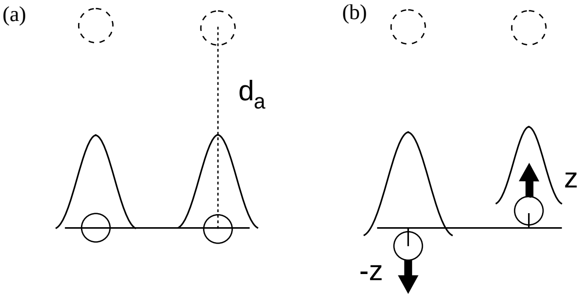

Fig. 2.50. Sketch of the charge disproportionation in NaV_2O_5 due to an V ion displacement ($\pm z$) along the c-axis in the field of the apical oxygen. The distance of the apical oxygen to the vanadium is given by d_a. The dashed circle (full circle) denotes the oxygen (vanadium) site. In (a) the situation in the homogeneous high temperature and (b) in the charge ordered phase is shown. The square pyramid oxygen sites are omitted [188].

phonon at 722 cm^{-1} is observed for temperatures up to $2T_{SP}$ [393]. In Raman scattering experimental spectra in crossed (ab) polarization show unexpected phonons of A_{1g} symmetry for temperatures $T_{SP} < T \leqslant 80$ K. This observation is compatible with a breaking of the inversion symmetry at this temperature. In X-ray diffraction the superstructure peaks allow to determine correlation lengths that show a crossover from 3D to 2D lattice fluctuations at about 50 K [394].

Fluctuations are also evident in NaV_2O_5 as a quasielastic light scattering intensity that shows a pronounced temperature dependence far above but also below T_{SP}. This broad feature, as shown in Fig. 2.51, is observed in crossed (ab) polarization [189]. Its intensity increases (with decreasing temperatures) below $T_{CO} \approx 80$ K, with T_{CO} defined as a fluctuation or crossover temperature of the electronic system. The intensity then drops again sharply with decreasing temperature below T_{SP}. As discussed below, in this temperature range the intensity of magnetic bound states start to rise. The quasielastic scattering contribution is therefore assigned to magnetic light scattering as it competes with the scattering intensity of the bound states [189,362].

A comparable effect is observed in (bb) polarization as a broad scattering continuum in the frequency range $50\ cm^{-1} \leqslant \Delta\omega \leqslant 160\ cm^{-1}$. It has a similar intensity as function of temperature, however, in this polarization the fluctuations close to the dimerization transition have a gapped spectrum, i.e. there is no scattering contribution for frequencies $\Delta\omega < 50\ cm^{-1}$ [189].

The phonon system shows more direct evidence for the onset of charge ordering at $T > T_{SP}$. A distinct phonon anomaly exists in A_{1g} symmetry at 422 cm^{-1}. This excitation displayed in Fig. 2.52 is very likely the phonon mode discussed above which is coupled to intersite charge fluctuations [189,188]. It shows a hardening below the transition, remarkable changes of the phonon lineshape and finally the evolution of a distinct second mode at 394 cm^{-1} for the lowest temperatures. The onset of the frequency dependence with lowering temperature is again at $T_{CO} = 80$ K.

The temperature dependence of the phonon energy in Fig. 2.52 shows a continuous, gradual change at T_{CO} instead of a transition. This behavior is attributed to the low dimensionality of the system. A similar "soft crossover" identified as a charge ordering has been observed in $La_2NiO_{4.133}$. For this 2D compound with a Ni–O square plane, stripe order into 1D domains of charge and spin is discussed. The intensity of the charge-order superstructure peak sets in for $T < T_{CO} = 200$ K triggering the magnetic order at $T_m = 110$ K [51]. In addition to the very similar temperature dependencies of

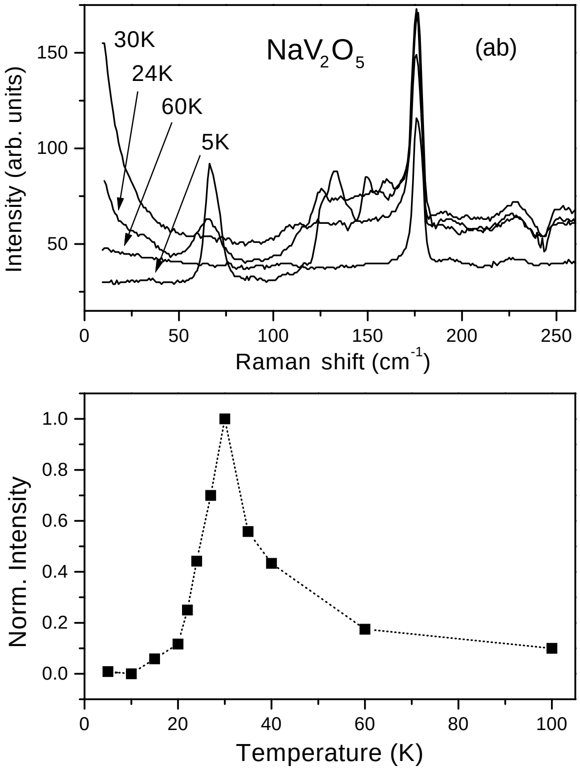

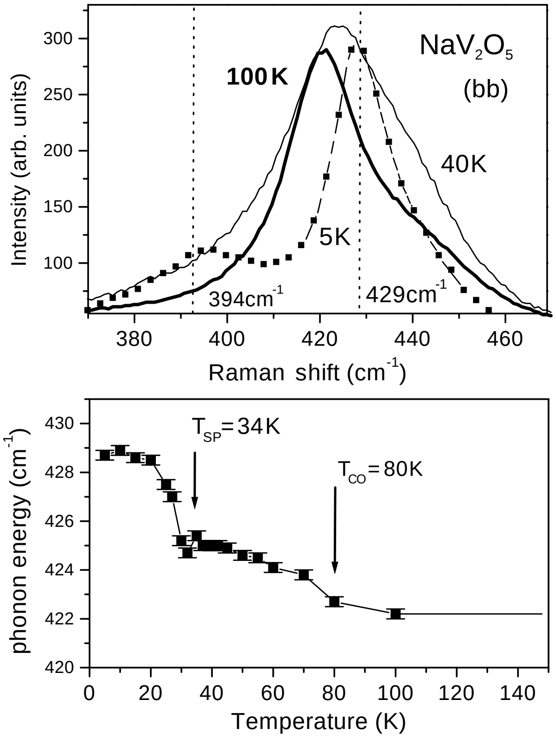

Fig. 2.51. Quasielastic light scattering in NaV$_2$O$_5$ in crossed (*ab*) polarization and its normalized intensity as function of temperature [189].

Fig. 2.52. Raman light scattering spectra of NaV$_2$O$_5$ (upper panel) and excitation energy of a A$_{1g}$ phonon at 422 cm^{-1} in intraladder (*bb*) polarization (lower panel). The onset of the phonon hardening (T_{CO}) and the transition temperature (T_{SP}) are marked by arrows [189].

the superstructure intensities of charge ordering in both compounds also the reduced energy scales $T_{\mathrm{CO}}/T_m = 1.81$ and $T_{\mathrm{CO}}/T_{\mathrm{SP}} = 2.4$ are comparable.

Fluctuations in the spin and phonon system of NaV$_2$O$_5$ support a scenario for the singlet ground state that is motivated by the observation of three magnetic bound states in Raman scattering experiments [189,362,366]. These states poses mixed polarization selection rules. A dynamic superposition of several energetically nearly degenerate dimer configurations is compatible with this observation. The configurations should also include diagonal dimers on the ladder. This scenario resembles the dynamic pseudo-Jahn–Teller effect or an RVB model, emphasizing either the importance of phonons or electronic correlations [362]. The observation of gap-related excitations with energies that depend on the time or frequency scale of the respective experiment would be a critical proof. The large variation of the gap values determined by different measurement techniques at least suggests such non-adiabatic effects in NaV$_2$O$_5$. For a complete discussion of the bound state properties motivating this approach see Section 4.

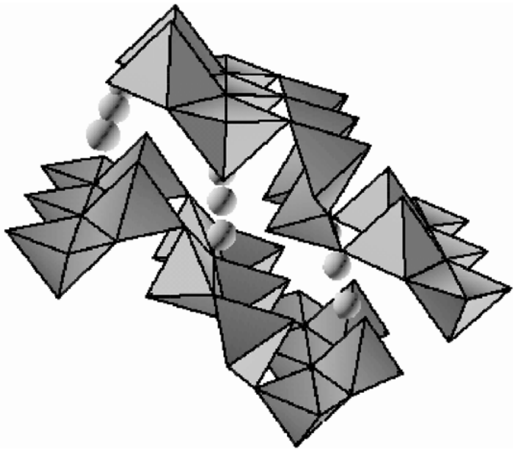

Fig. 2.53. Crystal structure of γ-LiV_2O_5. Shown are the two equivalent xy-planes. There are two kinds of VO_5 square-pyramids, containing the V(1) and V(2)-ions, respectively. Note the substantial corrugation of the xy-plane, compare with the lattice structure of NaV_2O_5 presented in Fig. 2.43.

Comparison with LiV_2O_5. Since NaV_2O_5 is an insulator, it was initially thought [83,206] to contain two inequivalent V-ions, with electronic configuration $(3d)^0$ and $(3d)^1$ and with the V-$(3d)^1$ ions forming zig-zag spin-1/2 chains. Refined crystallographic data analysis at room temperature [209,287,395] showed the existence of only one equivalent V-ion in a mixed-valence $(3d)^{0.5}$ configuration. It was then shown by DFT-calculation [287,364] that the insulating nature of NaV_2O_5 arises from a bonding–antibonding splitting of V–O(1)–V orbitals. The moment-carrying bonding orbital is there delocalized, giving rise to the possibility of further charge ordering phenomena at lower temperatures, as discussed in the previous section.

LiV_2O_5 is, on the other hand, charge ordered at all temperatures [396,397] and has a very similar lattice structure as NaV_2O_5 (see Fig. 2.53). A refined DFT-analysis has shown that the degree of charge ordering is not complete, but roughly 70:30 [203]. The degree of charge ordering determines the nature of the underlying physical model: A 50:50 charge distribution (no ordering like in the high-temperature phase of NaV_2O_5) implies a quarter-filled ladder compound. Complete charge ordering 0:100 would imply, on the other hand, a zig-zag chain compound. The DFT-result for LiV_2O_5 of a 70:30 charge-ordering implies, on the other hand, an asymmetric-ladder model [203] with Coulomb coupling in between adjacent ladders [388]. These findings suggest that the degree of charge-ordering in the low-temperature phase of NaV_2O_5, which is to date not known [398,399], would have substantial influence on the underlying physical model.

2.8. Magnetic parameters of selected spin systems

In Table 2.2 magnetic parameters of selected spin systems are summarized. Due to frustration, exchange topology or spin–phonon coupling many compounds prefer other ground states than long-range magnetic order.

Table 2.2
Selected inorganic one-dimensional spin systems and their magnetic parameters

Compound	$J_{\parallel}$	$J_{\perp}$	Δ_{01}	α	δ	T_N	T_{SP}	System
$YBa_2Cu_3O_6$	1400	1400	—	—	—	≈ 500	—	2D square plane
$SrCu_2(BO_3)_2$	70	—	34	0.6	—	—	—	2D frustrated
$KCuF_3$	187–203	—	—	—	—	39	—	Chain
Sr_2CuO_3	1300	—	—	—	—	11	—	Chain
$SrCuO_2$	2100	—	—	—	—	—	—	Zig-zag chain
$SrCu_2O_3$	850–2000	750–1000	280–420	—	—	—	—	Ladder
$Sr_{14-x}Ca_xCu_{24}O_{41}$	1050–1500	750–830	120–133;550–270	—	—	2–4	–	Ladder+chain
$(VO)_2P_2O_7$	100–120	—	37, 69	—	0.09, 0.19	—	—	Alternating chains
$CuGeO_3$	120–160	15	24–30	0.24–0.37	0.012–0.05	—	14.3	Spin-Peierls
NaV_2O_5	440–560	15	84–110	—	0.03–0.09	—	34	1/4–filled ladder

All units are in [K]. $J_{\parallel}$ denotes the exchange coupling constants along the chains and ladders, $J_{\perp}$ the exchange coupling perpendicular to the chain or ladder, α and δ are parameters of frustration and dimerization. For $CuGeO_3$ the magnitude of the dimerization is still under discussion [306]. The transition temperatures for Néel and spin-Peierls ordering (T_N, T_{SP}) are given. In the case of $Sr_{14-x}Ca_xCu_{24}O_{41}$ the singlet–triplet gaps for the CuO_2 chain and the Cu_2O_3 ladder sublattice are given. For this compound we include the variation of the parameters due to Ca substitution or different experimental techniques. For $SrCu_2(BO_3)_2$ the values given under $J_{\parallel}$ and α correspond to the larger intradimer exchange coupling (J_1) and the ratio of the coupling constants (J_2/J_1) with J_2 the interdimer coupling constant. References for the data are given in the respective sections to be found above.

3. Magnetic light scattering

Light scattering in magnetic compounds is a well established method. The study of spin waves or magnons in ferromagnetic and antiferromagnetic compounds has been used extensively to determine coupling constants, anisotropies and magnon–magnon interaction. A review of the principal effects and basic theory can be found in the textbook "*Light Scattering in Magnetic Solids*" by Cottam and Lockwood [400].

The coupling of light to elementary excitations of a solid is described by a differential scattering cross section. Its calculation reduces to the determination of the correlation function $\langle (\chi_k^{\alpha\beta})^* \chi_k^{\mu\nu} \rangle$ and is therefore based on the determination of the general susceptibility tensor $\chi(\mathbf{r})$ [400]. This leads to an effective Raman Hamiltonian

$$\mathscr{R}' = \sum_{\mathbf{r}} \sum_{\alpha,\beta} \mathbf{E}_I^{\alpha} \chi^{\alpha\beta}(\mathbf{r}) \mathbf{E}_S^{\beta} \,, \tag{3.1}$$

with the electric field vector $\mathbf{E}_I$ and $\mathbf{E}_S$ of the incident and scattered light, respectively. Expanding the susceptibility $\chi(\mathbf{r})$ in powers of spin operators [401] we obtain:

$$\begin{aligned} \chi^{\alpha\beta}(\mathbf{r}) = {} & \chi_0^{\alpha\beta}(\mathbf{r}) + \sum_{\mu} K_{\alpha\beta\mu}(\mathbf{r}) S_{\mathbf{r}}^{\mu} + \sum_{\mu,\nu} G_{\alpha\beta\mu\nu}(\mathbf{r}) S_{\mathbf{r}}^{\mu} S_{\mathbf{r}}^{\nu} \\ & + \sum_{\boldsymbol{\delta}} \sum_{\mu,\nu} M_{\alpha\beta\mu\nu}(\mathbf{r}, \delta) S_{\mathbf{r}}^{\mu} S_{\mathbf{r}+\delta}^{\nu} + \text{higher order terms} \,. \end{aligned} \tag{3.2}$$

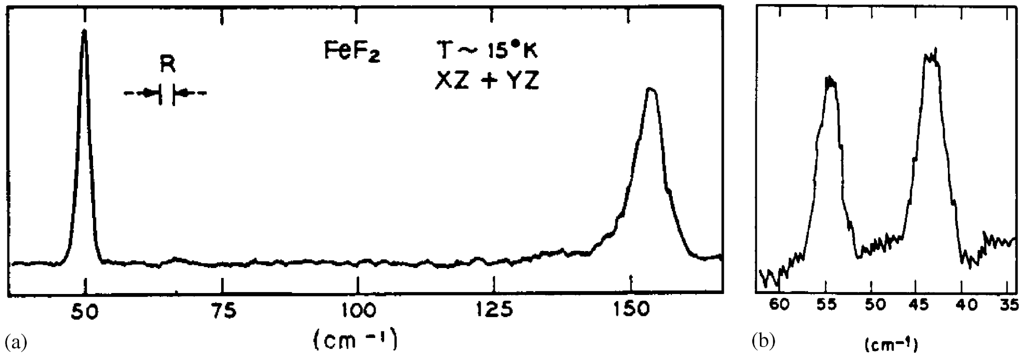

Fig. 3.1. Magnetic Raman scattering of the 3D antiferromagnet FeF_2. (a) Both one- and two-magnon scattering are observed at 50 and 155 cm^{-1}, respectively ($T = 15$ K). (b) Measurements in an applied magnetic field of 5.2 T show a splitting only of the one-magnon signal ($T = 20$ K).

The first term in Eq. (3.2) corresponds to Rayleigh scattering, the second and third term are linear and quadratic in the spin operators and induce spin flips at a *single* ionic site **r**. The complex tensors K and G determine the strength of the coupling of light to the spin system associated with spin–orbit coupling. They may be evaluated using Faraday rotation and magnetic linear birefringence. In inelastic light scattering the resulting one magnon signal has off-diagonal and diagonal elements of the susceptibility tensor.

3.1. Two-magnon scattering

Two-magnon scattering which is observed with appreciable intensity in antiferromagnets is induced by the fourth term in Eq. (3.2) that couples spin operators at *different sites* **r** and $\mathbf{r}+\delta$. A pair of excitations of exchange coupled magnetic sites on opposite sublattices with $\Delta S^z = 0$ and wave vectors of similar amplitude but different sign are induced. The effective Hamiltonian reads:

$$\mathscr{R}'' = \sum_{\mathbf{r},\delta}\sum_{\alpha\beta\mu,\nu} \mathbf{E}_{\mathrm{I}}^{\alpha}\mathbf{E}_{\mathrm{S}}^{\beta} M_{\alpha\beta\mu\nu}(\mathbf{r},\delta) S_{\mathbf{r}}^{\mu} S_{\mathbf{r}+\delta}^{\nu} \ . \tag{3.3}$$

In Fig. 3.1 a Raman spectrum of FeF_2 is shown [400]. This Ising-type antiferromagnet ($T_{\mathrm{N}} = 78.4$ K) is one of the rare cases where both one- and two-magnon scattering are observed with comparable intensities. More usual is either the observation of one-magnon scattering in systems with strong spin–orbit coupling or two-magnon scattering in systems that are close to an isotropic exchange. The typical width of the 2-magnon response in 3-dimensional, ordered antiferromagnets is much smaller than the characteristic energy, as evidenced for FeF_2 in Fig. 3.1. This is in contrast to the 2-magnon intensity for quasi one-dimensional systems, which we will discuss further below.

The symmetry of Eq. (3.3) with respect to the spin operators and the electric field vectors leads to special selection rules in the case that the magnetic system has a dominant exchange path. For one-dimensional spin systems two-magnon scattering is observed only in the A_{1g} scattering component, with $\mathbf{E}_{\mathrm{I}}$ and $\mathbf{E}_{\mathrm{S}}$ both parallel to the crystallographic direction of the exchange path. To observe this type of scattering the Raman operator is required not to commute with the exchange

Hamiltonian. Therefore, any additional perturbation of the exchange Hamiltonian, such as a dimerization or frustration of the spin system is helpful. The Raman light scattering intensity I scales with $I \propto J^2$. For 2D antiferromagnets, such as the parent compounds of the high-temperature superconductors, magnetic scattering is allowed only in the B_{1g} scattering component, i.e. with perpendicular in-plane electric field vectors. As the symmetry selection rules described by Eq. (3.3) only apply to non-resonant scattering they may be broken if the energy of the intermediate state matches the energy of some electronic excitation levels.

3.2. Light scattering in high-temperature superconductors

The most prominent and complete examples of light scattering studies in 2D antiferromagnets have been performed on the parent compounds of the HTSC, e.g., $YBa_2Cu_3O_{6+\delta}$ [402,403], La_2CuO_4 [404] or $Bi_2Sr_2(Ca_{1-x}Y_x)Cu_2O_8$ [131,132]. They have been studied to understand the temperature-doping phase diagram, pseudo-gap phenomena and related effects [405,406].

Two-magnon light scattering [144,407] in the Néel phase of the undoped HTSC shows some peculiarities that strongly deviate from the behavior of other antiferromagnets [408–410]. The two-magnon density of states with a maximum at an energy of approximately 2.7 J is not only observed in the B_{1g} light scattering component but also in the B_{2g} and A_{1g} components. Additionally, the maxima of scattering intensity are strongly asymmetric and broadened to higher energy. There are pronounced resonance effects by tuning the energy of the incident light. Although a coupling of the magnons to phonons and strong magnon–magnon interaction might describe this behavior qualitatively, the resonance effects point to an electronic origin. A triple resonant scattering in the virtual intermediate state of the Raman process on the charge transfer gap of these compounds has successfully been used to explain the breakdown of the symmetry selection rules and anomalous lineshapes [408,409].

Low-energy correlations in weakly doped HTSC are discussed in the context of stripe-like dynamic charge and spin correlations [50]. These aspects have been studied using light scattering in the isostructural nickelates [411–414]. Commensurate and static charge and spin ordering to stripes is observed in $La_{1.66}Sr_{0.33}NiO_4$ at $T < T_{CO} = 240$ K and $T < T_m = 190$ K, with T_{CO} and T_m the charge and spin ordering temperatures, respectively. The HTSC and nickelates both share the square plane structural element. However, the linear Cu–O–Cu superexchange in HTSC with $J \approx 800$–1700 K is stronger compared with the Ni–O–Ni superexchange with $J \approx 350$ K.

3.3. Light scattering in quasi-one-dimensional spin systems

For light scattering in quasi-one-dimensional spin systems other selection rules apply compared to 2D antiferromagnets, see Eq. (3.3). Due to the dominant exchange path along one crystallographic direction only magnetic scattering with the polarization of $\mathbf{E}_I$ and $\mathbf{E}_S$ both parallel to this direction is allowed. Furthermore, the Hamiltonians of magnetic exchange scattering and the magnetic spin system should not commute. This will be explained further in discussing the Hamiltonian of a static spin-Peierls system including frustration. It has been successfully used to model the Raman scattering results on the spin-Peierls compound $CuGeO_3$ for temperatures above and below $T_{SP} = 14.3$ K [97]. The Hamiltonian for a spin-Peierls chain is given by

$$\mathscr{H}_{SP} = J_{nn} \sum_i [(1 + \delta(-1)^i)\mathbf{S}_i \cdot \mathbf{S}_{i+1} + \alpha \mathbf{S}_i \cdot \mathbf{S}_{i+2}] \; . \tag{3.4}$$

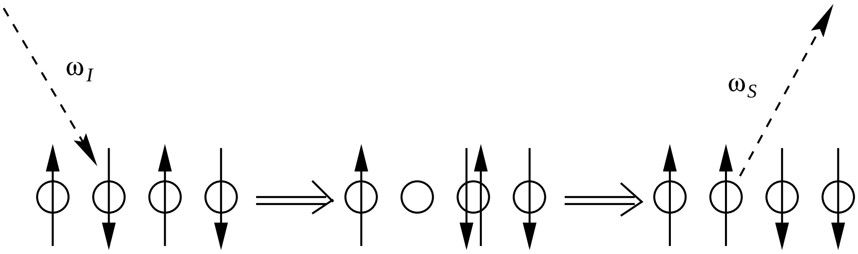

Fig. 3.2. Sketch of an exchange light scattering process on two singlet states on a spin chain. ω_I and ω_S denote the frequency of the incident and scattered photon, respectively.

In Eq. (3.4) the exchange coupling to nearest neighbors $J_{\mathrm{nn}}\mathbf{S}_i \cdot \mathbf{S}_{i+1}$ is modulated for $T \leqslant T_{\mathrm{SP}}$ by the dimerization $\delta \neq 0$. A competing exchange coupling to the next nearest neighbor given by $\alpha\mathbf{S}_i \cdot \mathbf{S}_{i+2}$, with the frustration parameter $\alpha = J_{\mathrm{nnn}}/J_{\mathrm{nn}}$, changes the excitation spectrum and ground state properties considerably as described in Section 1.

For an alternating spin chain with dimerization γ the Raman operator corresponding to Eq. (3.1) has the form:

$$\mathscr{R} = \sum_i (1 + \gamma(-1)^i)\mathbf{S}_i \cdot \mathbf{S}_{i+1} \ . \tag{3.5}$$

We compare the Hamiltonian in Eq. (3.4) with the Raman operator in Eq. (3.5) taking into account a dimerization γ. For $\delta = \gamma = 0$ there is no exchange scattering without the frustration term as $[\mathscr{H}_{\mathrm{SP}}(\alpha = 0), \mathscr{R}] = 0$. With $\alpha \neq 0$, the model (Eq. (3.4)) leads to magnetic Raman scattering which has been observed experimentally in the spin-Peierls compound $\mathrm{CuGeO_3}$ [97,308,309,415].

3.3.1. The limit of large dimerization

In the limit of large dimerization δ the exchange light scattering process in 1D spin systems may be illustrated on a small system of four spins $\mathbf{S}_1$, $\mathbf{S}_2$, $\mathbf{S}_3$ and $\mathbf{S}_4$ [416]. The singlet ground state $|s,s\rangle$ is formed by a product of two singlets $\mathbf{s}_{12}$ and $\mathbf{s}_{34}$.

The Raman operator (3.5) for this system simplifies to $\mathscr{R}_{23} = \mathbf{S}_2 \cdot \mathbf{S}_3$. Using the usual spin operators $S_i^z, S_i^+ = S_i^x + \mathrm{i}S_i^y$, and $S_i^- = S_i^x - \mathrm{i}S_i^y$ leads to

$$\mathscr{R}_{23} = S_2^z S_3^z + (1/2)(S_2^+ S_3^- + S_2^- S_3^+) \ . \tag{3.6}$$

The exchange Raman process is then given by

$$\mathscr{R}_{23}|s,s\rangle = (1/4)(-|t_0,t_0\rangle + |t_1,t_{-1}\rangle + |t_{-1},t_1\rangle) \ , \tag{3.7}$$

where $t_{0,\pm 1}$ denotes the triplet state with the corresponding S^z component. The total spin before and after the application of $\mathscr{R}_{23}$ is zero. Two elementary magnons are created in the spin system. This is sketched in Fig. 3.2 [410]. Note, that the two magnons are created (in the limit of large dimerization) on adjacent dimers.

3.3.2. Non-zero temperature

For $T \neq 0$ the lowest triplet branch may be thermally populated. Achieving this situation in a spin-Peierls systems means that the reduced gap ratio $2\Delta_{\mathrm{SP}}/T_{\mathrm{SP}}$ should not be too large, e.g., not larger than the mean field value 3.5. This requirement is fulfilled in the case of $CuGeO_3$ and $(VO)_2P_2O_7$ but not in the case of NaV_2O_5. We study a situation where the Raman process uses $|t_0, s\rangle$ as an initial state [416]. This leads to

$$\mathcal{R}_{23}|t_0, s\rangle = (1/4)(-|s, t_0\rangle + |t_1, t_{-1}\rangle - |t_{-1}, t_1\rangle) \ . \tag{3.8}$$

Here, the total spin before and after the application of $\mathcal{R}_{23}$ is unity as requested by the exchange light scattering process. The first term in (3.8) does not change the number of triplets in the system. The other terms induce a transition from one to two triplets. Therefore, this process is called three-magnon scattering since it involves a magnon in the initial state and two magnons after the scattering process [416].

3.3.3. Defect-induced light scattering

An interesting aspect of dimerized quantum spin systems is the substitution of a magnetic site by a non-3d ion creating a spin vacancy. In principle every substituted site breaks up one dimer and frees one spinon [37,417]. This is noticeable as a Curie–Weiss contribution to the magnetic susceptibility. The question now arises whether this substitution may lead to similar well-defined bound states as in the pure dimerized phase. Observations using NMR and ESR would support such effects since states in the spin-Peierls gap are induced by the substitution [37].

Furthermore, also a well-defined binding energy may be realized due to a binding effect of the spinon to the defect site [36,353]. Taking a spin system with singlets at the sites $(i-2, i-1)$, a substitution at site $i-2$ leads to a spinon at site $i-1$. The spinon moves freely without changing the number of singlets but changing their position as long as the position of the singlets does not change the energy of the system. In contrast, taking additional interactions into account this motion of the spinon away from the defect site costs energy. In first approximation, i.e. for a sufficiently large frustration, this binding energy is linear in the distance between the spinon and the defect site. In this sense the effect of next nearest neighbor intrachain interaction and interchain or magnetoelastic interaction is expected to be similar [32,353].

From the theoretical side a light scattering process on such a spinon or dopant bound state is possible [416,353]. Starting from the Raman exchange light scattering Hamiltonian in Eq. (3.5) and using the limit of large dimerization the spin system now includes a spinon at site $i-1$. We consider the singlet at site $(i, i+1)$, the relevant part of $\mathcal{R}$ is $\mathcal{R}=(1-\gamma)\mathbf{S}_{i-1}\cdot\mathbf{S}_i$. Applying $\mathcal{R}$ to the $|\uparrow\rangle$-spinon at $i-1$ and the adjacent singlet at $(i, i+1)$ yields

$$\mathcal{R}|\uparrow, s\rangle = (1-\gamma)[(1/4)|\uparrow, t_0\rangle - 1/(2\sqrt{2})|\downarrow, t_1\rangle] \tag{3.9}$$

$$= \frac{1-\gamma}{4}|s,\uparrow\rangle + \frac{1-\gamma}{4\sqrt{2}}[|\uparrow,\uparrow,\downarrow\rangle - |\downarrow,\uparrow,\uparrow\rangle] \ . \tag{3.10}$$

The arrows indicate the S_z component of the spinon and s, t_0 or $t_{\pm 1}$ stand for a singlet and a triplet with $S_z = 0$ or $S_z = \pm 1$ for two spins. The effect of the Raman operator may be summarized in shifting the spinon by one singlet spin pair to the right by two sites (the first term in Eq. (3.10)) and the creation of a n.n.n. singlet (the second term in Eq. (3.10)) in between sites $i-1$ and $i+1$. The total spin of the system remains unchanged.

Thus the Raman operator is able to induce transitions in between different so-called dopant-bound spinons (DBS), e.g. in between the ground-state and the first excited DBS states. This exchange

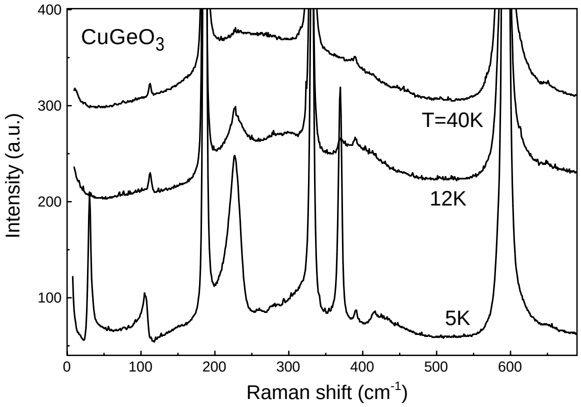

Fig. 3.3. Intrachain (cc) polarized Raman light scattering spectra of $CuGeO_3$ for temperatures above and below $T_{SP}=14.3$ K (the curves have been given an offset for clarity).

scattering mechanism should show no magnetic field dependence since initial and final states are both triplets. Furthermore, the limit of strong dimerization used to facilitate the discussion is not mandatory as a comparable description is also valid in the limit of weak dimerization [353]. Experimental results that are consistent with this scenario have been obtained in Zn-substituted $CuGeO_3$ and will be discussed in Section 4.1.2.

3.4. Spinon light scattering in $CuGeO_3$: experimental results

Intrachain (cc) polarized Raman spectra of $CuGeO_3$ are shown in Fig. 3.3 for temperatures above and below $T_{SP}=14.3$ K [328]. Above T_{SP} (40 K) a broad continuum extending from 150 to 500 cm^{-1} has attributed to spinon scattering. Lowering the temperature the intensity of this signal is suppressed (see Fig. 4.4 (open squares)). On the other hand, transition-induced modes appear that will be discussed in Section 4.1. The continuum is observed only for both incident and scattered light polarizations parallel to the CuO_2 chain direction. These polarization selection rules are consistent with the dominant exchange path of a 1D spin system.

The magnetic Raman light scattering intensity given by Eqs. (3.4) and (3.5) has been modelled using different theoretical approaches [97,418–420]. In Fig. 3.4 typical experimental results of the spinon continuum observed in $CuGeO_3$ in the homogeneous phase $T > T_{SP}$ ($T=20$ K) are compared to theoretical model calculations [97]. Phonon lines have been subtracted from the measurement for clarity. The calculation has used a solitonic mean-field approach to evaluate the Raman intensity at finite temperatures [97,419]. Comparable results have also been obtained by other groups [418,420].

The observed broad continuum in the frequency range 150–550 cm^{-1} is a consequence of the frustration term proportional to α in Eq. (3.4) since the nearest neighbor term in (3.4) conserves the number of spinons. Therefore, this scattering contribution has been named “frustration-induced scattering” [97]. The derived coupling constants that give a qualitative good description of the experimental data ($J = 150$ K, $\alpha = 0.24$) are in agreement with results from fits to the magnetic susceptibility [294]; however, they are smaller than results derived from thermal expansion data [297]. As the model used in Eqs. (3.4) and (3.5) neglects phonon degrees of freedom as well as

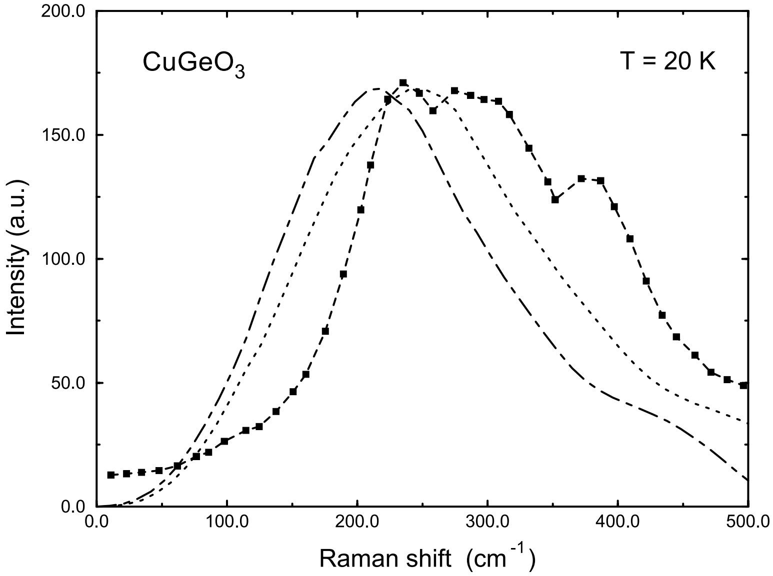

Fig. 3.4. Comparison of experimental Raman spectra (squares) with calculations (lines) for $CuGeO_3$ in the homogeneous phase ($T = 20$ K). Phonon lines have been subtracted for clarity. Theoretical results are determined with $\delta = \gamma = 0$ for (a) $J_{nn} = 150$ K, $\alpha = 0.24$ (dashed dotted line) and (b) $J_{nn} = 170$ K, $\alpha = 0.2$ (dotted line).

interchain interaction the agreement between theory and experiment is promising enough to identify the continuum in Fig. 3.4 as of spinon scattering origin.

For temperatures below T_{SP} the Raman response of the spin-Peierls system changes considerably due to the dimerization δ, as shown in Fig. 3.3 [60,328]. As a reasonable theoretical approach a direct diagonalization of a system of 28 spins has been performed to determine the four-spin correlation function. The calculated excitation spectrum has been approximated analytically. A following study of the dependence on γ in Eq. (3.5) and a comparison with experiment have led to $\gamma = 0.12$.

As shown in Fig. 3.5, the decrease of the intensity of the continuum and the existence of the sharp mode at 30 cm^{-1} is well described. The strong effect of the γ-term on the calculated spectra has been explained by matrix-element effects of the Raman operator (Eq. (3.5)) [97]. An alternative description of the mode at 30 cm^{-1} as a magnetic singlet bound state will be discussed in Section 4.

3.5. Raman scattering from spin-1/2 ladders

The very broad Raman response of spin-1/2 chain compounds like $CuGeO_3$, as evidenced in Fig. 3.4, is due to the 2-spinon-continuum illustrated in Fig. 1.1. The magnetic excitation spectrum of 2-leg ladders is, on the other hand, dominated by magnons (spin-1 excitations). This is illustrated in Fig. 1.4. The magnetic Raman response for a two-leg ladder is therefore quite narrow, especially for small ratios of $J_{\|}/J_{\perp}$. In Fig. 3.6 the Raman response of CaV_2O_5 from Ref. [421] is compared with a fit using $J_{\|}/J_{\perp} = 0.09$, $J_{\perp} = 431$ cm^{-1} (solid line) assuming an experimental resolution of $\Gamma = 3$ cm^{-1}. The long dashed line gives a fit with $J_{\|}/J_{\perp} = 0.125$, $J_{\perp} = 447$ cm^{-1}, $\Gamma = 0$, the thin horizontal line corresponds to the offset of the fits to account for a scattering background [77].

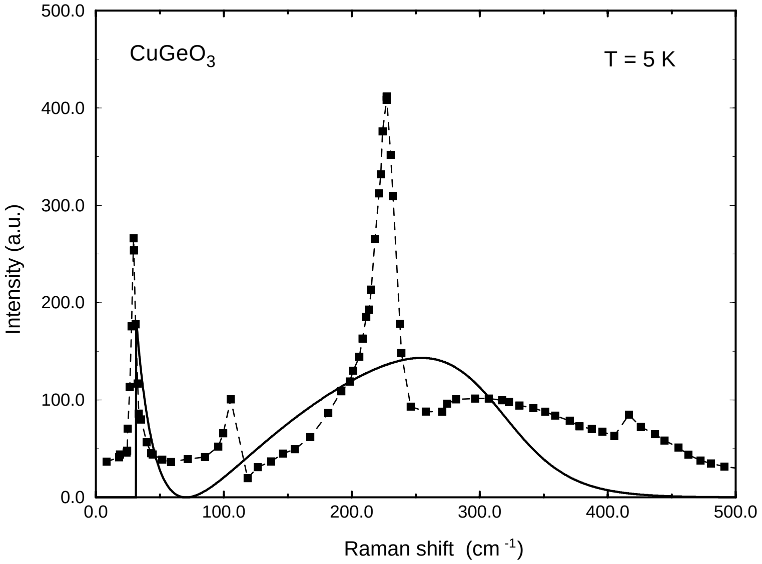

Fig. 3.5. Comparison of experimental Raman spectra (squares) with calculations (bold line) for $CuGeO_3$ in the dimerized spin-Peierls phase ($T = 5$ K). Phonon lines have been subtracted from the spectra with the exception of the spin-Peierls-induced phonon mode at 107 cm^{-1}.

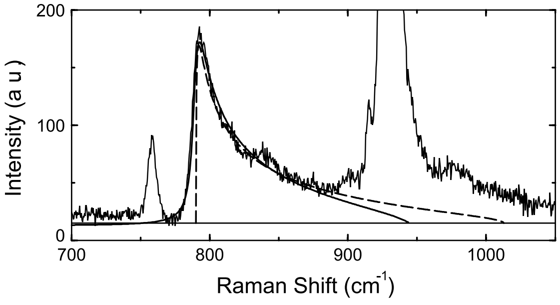

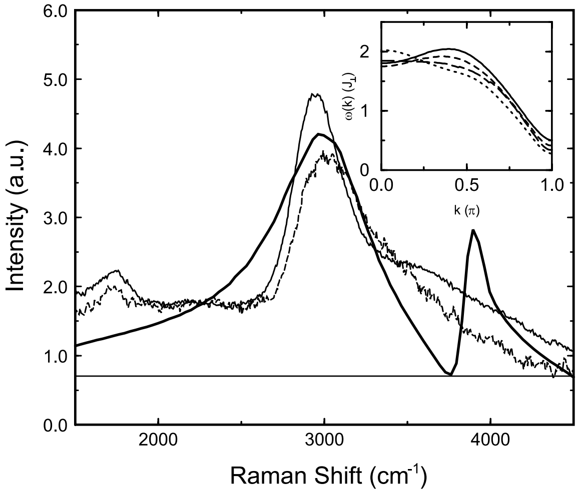

Fig. 3.6. Experimental Raman response of CaV_2O_5 [421] compared with different model calculations as described in the text [77].

Fig. 3.7. Raman response of $La_6Ca_8Cu_{24}O_{41}$. Noisy thin lines: experimental data [179] in (aa) (dashed) and (cc) (solid) polarization scaled to the same constant value between 2000 and 2500 cm^{-1}. The thick solid line represents the theoretical result for $J_{\parallel} = J_{\perp} = 1100$ cm^{-1} and a resolution $\Gamma = 3$ cm^{-1} [77]. The inset gives the 1-triplet dispersions $\omega(k)$ for $J_{\parallel} = J_{\perp}$ and the cyclic 4-spin term parameter $x_{cyc} = 0, 0.05, 0.10, 0.15$ (solid, dashed, long dashed, dotted) [77].

An interesting aspect of magnetic Raman scattering from two-leg ladders is the possible occurrence of two maxima in the response for larger values of the ratio $J_{\|}/J_{\perp}$ due to the minimum in the magnon dispersion relation near $k=0$ (see Fig. 1.4). The theoretically predicted second high-frequency maximum [77] has not yet been observed in Raman experiments. As an example we show in Fig. 3.7 the Raman response of $La_6Ca_8Cu_{24}O_{41}$, which can be modelled by $J_{\perp}=J_{\|}$.

Here, the thick solid line is the theory for $J_{\|}=J_{\perp}=1100\ \mathrm{cm}^{-1}$ and a resolution $\Gamma=3\ \mathrm{cm}^{-1}$ [77]. The thin horizontal line corresponds to an offset of the fit to account for background. The non-observance of the second magnetic Raman peak in the experimental data by Sugai et al. (1999) [179] may be due to an additional cyclic 4-spin term in the Hamiltonian, discussed in the context of spin-1/2 ladders [77,422] or due to overlapping contributions from the two-particle continuum (see Fig. 1.4).

4. Magnetic bounds states

Magnetic bound states of elementary triplets are a general feature of all quantum spin systems with a singlet ground state and a gapped excitation spectrum. The bound state energies are reduced below the energy of the two-triplet continuum. Important parameters concerning this binding effect are spin frustration as given by a competing next nearest neighbor exchange interaction as well as interchain exchange or magnetoelastic interaction. The properties of magnetic bound states such as energy, spectral weight and multiplicity characterize the spin–spin correlations or instabilities of a quantum spin system.

One-dimensional exchange topologies analyzed theoretically concern the dimerized and frustrated spin chain [6,29,423–425], the one-dimensional Hubbard model [426], spin chains with interchain [32] or spin–phonon interaction [33–36], spin ladders [21], and frustrated spin ladders [17,30]. Additional bound states are also induced by defects in spin chain systems with frustration or interchain coupling [36,353].

With respect to 2D systems the strongly frustrated Shastry–Sutherland lattice [118,427,428], the frustrated [429] or 1/5-depleted square lattice [27,28] and the Kagomé lattice [430] have been investigated. The latter and related systems with strong frustration and a degenerate ground state are recently in the center of interest as they exhibit a gapped elementary triplet spectrum coexisting with and filled up with collective singlet ($S=0$) excitations. These non-magnetic excitations may have energies smaller than the gap, depending on a delicate balance of the coupling constants of the systems [431,432,63].

In a dimerized spin chain (purely magnetic 1D model) the magnetic excitation spectrum contains a triplet branch Δ_{01} and a corresponding two-particle continuum of triplet excitations for energies above $2\Delta_{01}(\mathbf{k}=0)$. If a frustration of the spin system due to next nearest neighbor intrachain exchange or an interchain interaction is taken into account well-defined magnetic bound states develop [6,29,32]. These states consist of strongly interacting triplet excitations. The high-energy cutoff of these bound states is again given by $2\Delta_{01}(\mathbf{k})$. Above this energy the bound states dissolve in the two-particle continuum. For a critically frustrated spin chain ($J_2/J_1=\alpha_c=0.24$) one singlet bound state is predicted with an energy $\Delta_{00}=\sqrt{3}\Delta_{01}$. A further triplet bound state with a considerable spectral weight exists only for larger values of J_2 [6,29].

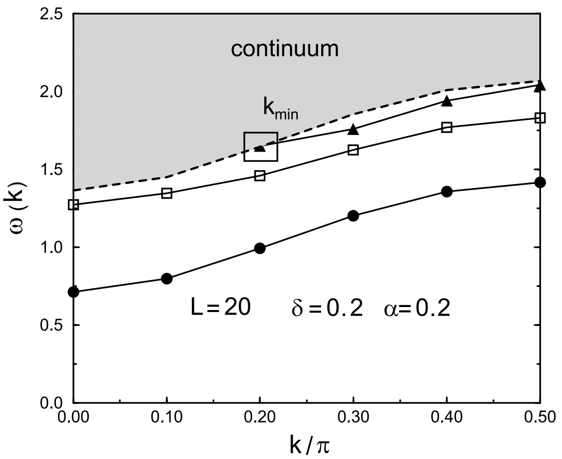

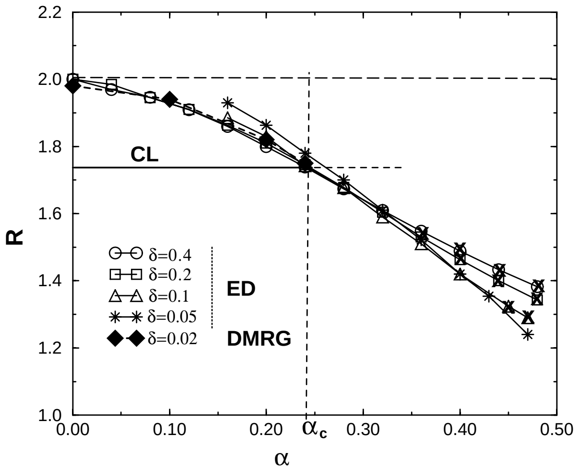

Fig. 4.1. Excitation diagram $\omega(\mathbf{k})$ of a dimerized ($\delta = 0.2$) and frustrated ($\alpha = 0.2$) antiferromagnetic Heisenberg chain [29]. Starting from the singlet ground state with increasing energy a triplet state (full dots), a singlet bound state (open squares) and a second triplet state (closed triangles) with a minimum $\mathbf{k} = \mathbf{k}_{\min}$ have been found.

Fig. 4.2. Effect of the frustration α on the ratio $R = \Delta_{00}/\Delta_{01}$ of the singlet vs. the triplet state energy (for $\mathbf{k} = 0$). Different dimerization levels δ are investigated using exact diagonalization (ED) and density matrix renormalization group theory (DMRG). For $\alpha = \alpha_c = 0.2412$ the "classical limit" with $R = \sqrt{3}$ is recovered.

In Fig. 4.1 the calculated excitation diagram of a frustrated alternating Heisenberg chain is given for moderate frustration [29]. It is evident that the spectral weight of the second triplet bound state is restricted to a smaller phase space with an energy close to the continuum ($2\Delta_{01}$). The ratio $R = \Delta_{00}/\Delta_{01}$ of the singlet vs. the triplet state energy characterizes the binding effect and thereby the triplet interactions. In calculations using exact diagonalization and DMRG (Fig. 4.2) frustration has been found to be the main parameter controlling the binding energy of the singlet bound state vs. the triplet. In these purely one-dimensional systems the dimerization is of less importance for the ratio R. This effect may also be characterized by the "spinon velocity" that is reduced with frustration leading to a larger density of states for $\mathbf{k} \to 0$ [423].

The excitation spectrum of a two-leg Heisenberg ladder is not so well established. In first approximation it may be compared with a single frustrated chain. At least one singlet and one triplet bound state should exist. The strong coupling singlet ground state consists of a dimer on every rung of the ladder [21].

This situation changes drastically with intraladder frustration [17]. In the limit of dominant frustration the system is in a gapped "Haldane" phase, which can be mapped on a $s = 1$ chain. The dimer phase, realized for smaller frustration, and the "Haldane" phase are separated by a first-order transition line (quantum phase transition). Especially for coupling parameters close to the transition a complicated behavior of low-lying singlet and triplet bound states has been discussed [30]. An increasing number of bound states with enlarged binding energy should exist. These states soften below the one-particle triplets [30]. Finally, at the transition, many-particle states form which intermix strongly with each other. This general softening of both singlet and triplet modes at $\mathbf{k} = 0$ and the resulting degeneracy of infinite-particle states mark the quantum phase transition. As the size of the bound states in real space as well as their spectral weight increase dramatically this scenario should also have a profound effect at finite temperature, i.e. an increasing number of bound states should be observable [30].

Further important aspects of bound state formation especially in real systems are interchain and magnetoelastic interaction [32]. The corresponding states are often denoted as soliton/antisoliton bound states. In the following we will use the limit of strong dimerization to elucidate this effect. Interchain or magnetoelastic interactions lead to an energetically preferred dimer pattern. Breaking a dimer forms two seemingly independent solitons in the surrounding of the well ordered dimers. A consequent displacement of one soliton with respect to the other distorts the dimer pattern and increases the energy of the system. In this way a binding potential which is approximately linear with distance is realized. The state with lowest energy in this soliton/antisoliton binding potential is a triplet. A number of further excitation levels is realized, the soliton bound states. As the potential is steeper with increasing interaction, a smaller number of bound states is expected in systems that are closer to two dimensions [32]. For larger distances of the solitons, corresponding to energies above 2Δ, new soliton/antisoliton states are created. In the limit of vanishing interaction a soliton continuum of quasi-free particles is formed.

From the experimental point of view the importance of interchain interaction on the magnetic excitation spectrum of quasi-one dimensional compounds is not clear. This is caused by the fact that most of the so-far investigated systems exhibit both a non-negligible spin–phonon and interchain interaction. Regardless of this complexity, the observed phenomena were discussed and compared in most cases with purely magnetic model calculations. Experimental evidence for singlet bound states, excited triplet states (three-magnon process) and defect-induced states have been found in Raman scattering. In neutron scattering experiments triplet modes interpreted as a bound states have been observed. A complete discussion of the respective compounds and corresponding references will be given below.

Frustration is a very important aspect for 2D spin systems as it leads both to a gap in the triplet spectrum and an appreciable binding of the singlet states. A model system within this respect is the strongly frustrated $SrCu_2(BO_3)_2$ [111]. In the underlying 2D orthogonal dimer lattice triplets are strongly localized [11,28] and form bound states [118,427,428]. For this exchange topology a quantum critical point dividing a spin liquid from a Néel state has been postulated. The phase boundary is controlled by the ratio of the interdimer to the frustrating intradimer exchange coupling. A comparison of calculations of the magnetic susceptibility with measurements suggests that the compound is indeed close to the critical point [28,115,117]. Furthermore, a large number of low-energy singlet modes are observed in Raman scattering experiments that are attributed to two- and three-particle bound states [124]. For further discussion see Section 4.4.

To assign experimentally the observed excitations to magnetic bound states and distinguish them from alternative explanations a number of stringent criteria have been developed. The polarization selection rules and preferred energies in the interval $[\Delta_{01}, 2\Delta_{01}]$ have already been discussed. In addition, the application of a magnetic field should identify one-magnon scattering as a splitting or shift of the signal. The strength of the obligatory spin–orbit coupling may be judged by the g-value of the compound. Furthermore, the intensity or spectral weight of the additional modes as function of temperature or defect concentration is a useful characteristic. The singlet bound state as a composite state at the Γ-point is very sensitive to any fluctuation. It should therefore be

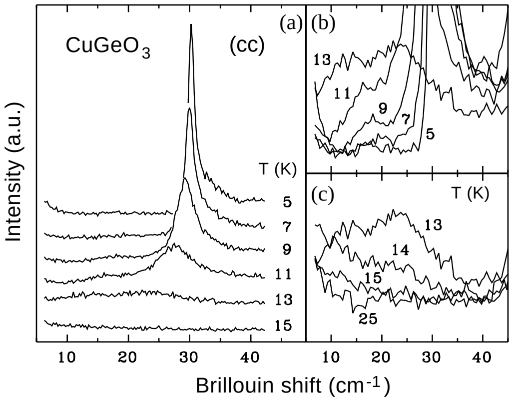

Fig. 4.3. Brillouin light scattering spectra of CuGeO$_3$ in intrachain (*cc*) polarization for several temperatures showing: (a) the singlet bound state response (the curves have been given an offset for clarity); (b) three-magnon scattering for $T < T_{SP}$; and (c) the disappearance of the scattering intensity for $T > T_{SP}$ [416].

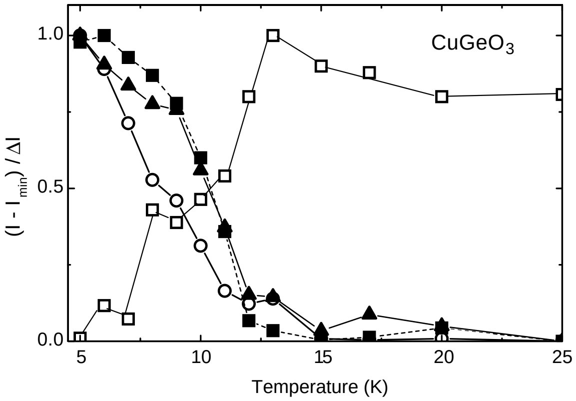

Fig. 4.4. Renormalized scattering intensities of the spin-Peierls-induced modes in CuGeO$_3$. The integrated intensity of the spinon continuum is marked by open squares. The modes at 369, 224, and 30 cm^{-1} are given by closed squares, closed triangles, and open circles, respectively [328].

destroyed with rising temperature or due to defects. In contrast, two-magnon scattering (from the zone boundary) persists as paramagnon scattering for $T \gg T_N$ due to short-range correlations [400]. To distinguish magnetic bound states from phonon-related bound states several arguments based on the frequency and lineshape of the observed modes may be used. They will be described in Section 4.2.

4.1. Bound states in CuGeO$_3$

The thoroughly studied inorganic spin-Peierls system CuGeO$_3$ has been used as a model system concerning bound states in dimerized spin chains [6,21,29,32,33,35,353]. In neutron scattering experiments a triplet state, $\Delta_{01} = 2.1$–2.4 meV, with a second, similar gap to a continuum is observed [295,296,320,319]. In light scattering experiments a sharp asymmetric mode is observed at $\Delta_{00} = 30$ cm^{-1} $\approx 1.78\Delta_{01}$. The appearance of this mode in the dimerized phase of CuGeO$_3$ is shown in Fig. 4.3(a) [416]. These experiments have been performed using a Sandercock-type tandem Fabry–Perot interferometer in 90° scattering geometry.

The mode at 30 cm^{-1} has been discussed controversially as a "1D two-magnon density of states", a soft mode connected with the spin-Peierls transition or as a continuum of bound states [97,308,309,313,326,415,433]. It is now understood as a singlet bound state Δ_{00} of triplet excitations [328,416]. This mode is only observable in light scattering experiments with intrachain polarization, i.e. incident and scattered light are polarized along the chain direction. This polarization selection rule is consistent with the spin conserving nature (no spin flip, i.e. $\Delta S = 0$) of the exchange light scattering mechanism, as described in Section 3. In addition this low-energy mode shows no shift or splitting in an applied magnetic field [313].

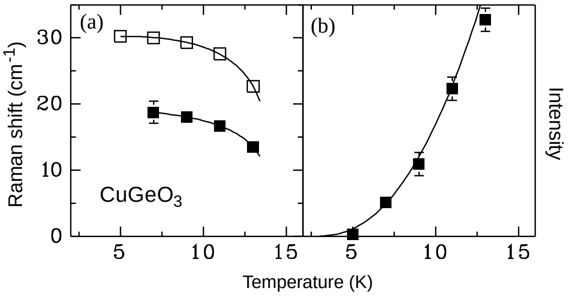

Fig. 4.5. Temperature dependence of the energy of the singlet bound state (open symbols) and the three-magnon scattering at 18 cm^{-1} (filled symbols). Solid lines are guides to the eye. (b) Temperature dependence of the intensity of the 18-cm^{-1} shoulder. The solid line corresponds to an activated T-dependence of the intensity of the three-magnon signal [416].

The temperature dependence of the integrated light scattering intensity of several spin-Peierls-induced modes is shown in Fig. 4.4 [328]. For elevated temperatures but still below the spin-Peierls transition $T \leqslant T_{SP}$ the intensity of the singlet bound state at 30 cm^{-1} decreases faster compared to the intensity of the dimerization-induced phonon modes at 369 and 224 cm^{-1}. This approximately linear decrease of integrated intensity with rising temperature shown in Fig. 4.4 by the open circles is a “fingerprint” of bound states as they are very sensitive to thermal fluctuations. The same effect leads to an enormous broadening comparable with the energy of this mode for temperatures still far below $T = T_{SP}$.

The strong decrease of the scattering intensity of the bound state and its broadening limits the temperature range in which the frequency of the bound state can be determined. This temperature dependence is composed of a product of $\Delta_{01}(T)$ and the temperature dependence of the binding energy (a weak function of the dimerization). As seen in Fig. 4.5(a) (open squares), this temperature dependence is non-mean field-like. It is not-identical to $\Delta_{01}(T)$ determined by neutron scattering experiments [295].

4.1.1. Three-magnon scattering in $CuGeO_3$

With rising temperature the lowest triplet branch in $CuGeO_3$ is thermally populated and a new scattering channel opens up at lower frequency. This three-magnon scattering corresponds to transitions between thermally excited states, i.e. from the triplet branch at Δ_{01} to the continuum of two-triplet excitations with its low-energy onset at $2\Delta_{01}$. Therefore, Δ_{01} is also expected to be the low-energy boundary for this process. A theoretical description of this process is given in Section 3.3.2.

In Fig. 4.3(a) Brillouin spectra of $CuGeO_3$ at several temperatures below T_{SP} are shown. It is evident which at elevated temperatures the bound state at 30 cm^{-1} is not the only signal. At temperatures above 7 K a shoulder at frequencies of about 18 cm^{-1} develops that at a temperature of 13 K is comparable in intensity with the singlet bound state. At temperatures above 14 K this signal disappears again.

As shown in Fig. 4.5(a), the energy of this mode has a similar temperature dependence as the singlet at 30 K [416]. It must therefore be closely related to the singlet–triplet gap Δ_{01}. The ratio of both energies corresponds to the binding energy of the singlet bound state. The intensity of the 18 cm^{-1} mode, however, shows just the opposite temperature dependence compared with the intensity of the singlet bound state (compare open circles in Fig. 4.4 with Fig. 4.5(b). The fit in Fig. 4.5(b) corresponds to the temperature dependence that would be expected for a thermally activated process. The light scattering intensity at 18 cm^{-1} is totally intrachain polarized and observable neither in scattering in crossed nor in circular light polarization as all magnetic scattering in $\mathrm{CuGeO_3}$. No magnetic field dependence of these signals could be found up to 6 T [304,416]. These experimental results rule out one-magnon scattering which should have antisymmetric Raman tensor elements and should display a Zeeman splitting. Therefore, all experimental observations support the interpretation of the mode at 18 cm^{-1} as a three-magnon scattering process between excited triplet states.

4.1.2. Defect-induced bound states in $\mathrm{CuGeO_3}$

The effect of substitutions either on the Cu site or on the Ge site of $\mathrm{CuGeO_3}$ may be summarized as a strong change of the low-energy excitations in the dimerized phase as well as the creation of long-range Néel order. For a summary of substitution effects we refer to Sections 2.7.1 and 3.3.3.

Every spin vacancy breaks up one dimer and frees one spinon [37,417]. As there is a binding effect of the spinon to the defect site [32,36] and the Raman operator allows the excitation of the ground state of this spinon [353] it may lead to well-defined modes in Raman scattering experiments, the so-called dopant-bound spinons [416].

Indeed, in early Raman scattering experiments in $\mathrm{CuGeO_3}$ a mode with an energy smaller than the singlet bound state Δ_{00} has been observed. Some of these and later results have been tentatively attributed to one-magnon scattering [326,352,434]. Only recently more detailed experiments together with appropriate theoretical approaches have become available [36,353] (see also Section 3.3.3).

In describing these experimental results we will concentrate on the region with low and intermediate substitution level to minimize possible defect interactions. Furthermore, a substitution with a negligible effect on the global lattice properties and a very local disruption of the intrachain exchange path is desirable. All this is realized for Zn substitution of the Cu site of $\mathrm{CuGeO_3}$ [328,345]. There is no strong change of the lattice constants or the phonon frequencies with Zn doping and samples with a small and homogeneous Zn distribution are easily prepared [338]. In contrast, substitutions of Ge by Si lead to strong effects of lattice pressure due to the different ionic radii and possible changes of the interchain interaction [328,344].

In addition to the observed dopant-bound spinon in $\mathrm{CuGeO_3}$, the effect of substitutions are twofold. On the one hand the singlet bound state (of the pure system) is broadened and suppressed in spectral weight as a coherent confined state of two triplets [328,434]. On the other hand short-range dimer fluctuations are enhanced [37]. The latter effect has been studied in Zn as well as Si-substituted samples using Raman scattering of the dimerization-induced phonon mode at 370 cm^{-1} and X-ray scattering in Mg-substituted samples [328,341,352,435].

The effect of substitutions on the singlet bound state is demonstrated in Fig. 4.6 presenting Brillouin spectra of $\mathrm{Cu_{1-x}Zn_xGeO_3}$ with $x=0$–3.3% [304,353]. The singlet bound state (SBS) is well resolved as a sharp and asymmetric peak at 30 cm^{-1}. With Zn substitution the intensity of this mode drops drastically. Already for $x=2.0\%$ no definite mode is observed anymore. In the left panels of this figure the loss of integrated intensity and the frequency shift of the singlet bound state with substitution are given.

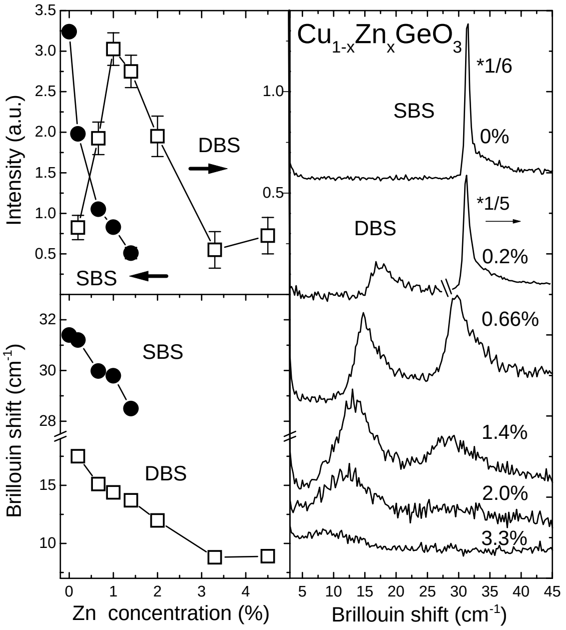

Fig. 4.6. Brillouin spectra of $Cu_{1-x}Zn_xGeO_3$, $x = 0$–3.3% in intrachain (cc) polarization are shown on the right panel with the singlet bound state (SBS) and the defect-induced dopant-bound spinon (DBS) ($T = 2.2$ K). The intensity corresponding to $x = 0$ is reduced by 1/6 and the SBS at $x = 0.2\%$ by 1/5. The upper and the lower left panel show the integrated intensity and the frequency of the modes as function of x [353].

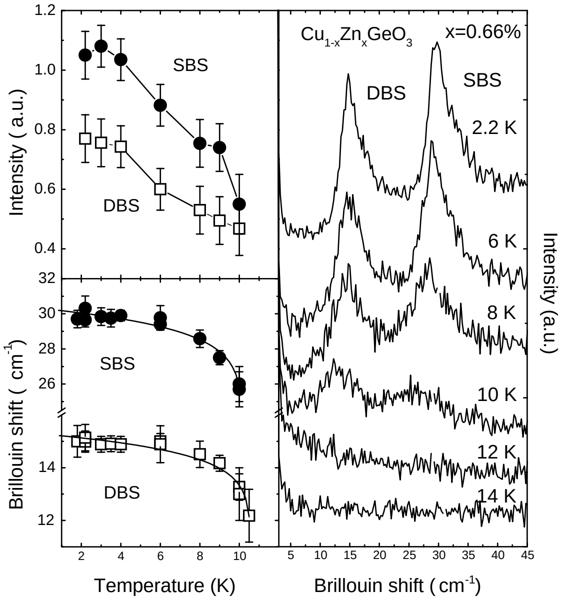

Fig. 4.7. Temperature dependence of the singlet bound state (SBS) and the dopant-bound spinon (DBS) in intrachain polarized Brillouin spectra of $Cu_{1-x}Zn_xGeO_3$, with $x = 0.66\%$ (right panel). The temperature dependence of the integrated intensity and the peak position of the modes are given in the upper and lower left panel [353].

A new well-defined excitation, denoted as a dopant-bound spinon (DBS), is observed at nearly half the frequency of the singlet bound state [353]. The integrated intensity of this mode increases roughly linear with increasing x for $x \leqslant 1\%$ (see upper left panel of Fig. 4.6). This linear increase corresponds to the desirable case of non- or weakly interacting defects. For larger x the intensity of this mode decreases again. In this concentration region the lineshapes of the two modes and the dependence of the frequencies of the modes on x are very similar. In addition, both modes are only observed in the presented intrachain (cc) scattering geometry.

The temperature dependence (2.2–14 K) of the Brillouin spectra for fixed $x = 0.66\%$ in Fig. 4.7 indicates further similarities of the two modes [353]. The integrated intensity, the energy as well as the linewidth vary in a comparable way with temperature. The left-hand panels of this figure show a detailed analysis of the data. Therefore, both modes must be related to the singlet–triplet gap. A further important piece of experimental evidence is the application of a magnetic field as it should discriminate possible one-magnon scattering contributions from magnetic bound states. The former scattering intensity should show a splitting or a shift of the observed signals. In Fig. 4.8 a comparison of Brillouin spectra with $B = 0$ and 4 T of $Cu_{1-x}Zn_xGeO_3$ with $x = 0.66\%$ is shown

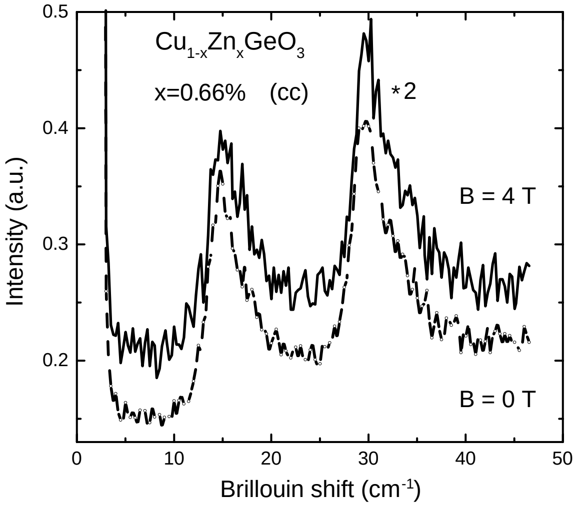

Fig. 4.8. Brillouin spectra of $Cu_{1-x}Zn_xGeO_3$ with $x = 0.66\%$ in intrachain (cc) polarization with an applied magnetic field of $B = 0$ and 4 T ($T = 2.2$ K) [304].

[304]. Neither the singlet bound state nor the dopant-bound spinon show an effect of the applied magnetic field.

In concluding, the presented data undoubtedly prove the existence of bound states of a substitution-induced spinon at the defect site. Neither the above discussed three-magnon light scattering process observed at elevated temperature nor one-magnon scattering can explain the observed experimental results.

4.2. Bound states in NaV_2O_5

The compound NaV_2O_5 differs in several aspects from $CuGeO_3$. This is summarized in its description as a quarter-filled ladder that on one hand adds electronic degrees of freedom to the system and on the other hand, as a ladder, has a different exchange topology. The dimerization-induced modes are altered from $CuGeO_3$ with respect to their multiplicity and polarization selection rules. Similar to $CuGeO_3$, the investigation of the temperature dependence of the intensity, frequency and half-width of these additional modes lead to a clear distinction between modes at low-energy that are candidates for magnetic bound states and simple zone-folded phonon modes due to the crystallographic distortion. From phonon and low-energy quasielastic scattering strong fluctuations are evident with an onset at $T_{CO} \approx 80$ K. This has been discussed in Section 2.7.2. These fluctuations may also be important for the understanding of the magnetic bound states in NaV_2O_5.

4.2.1. Experimental observations in NaV_2O_5

A comparison of intraladder (bb) spectra at $T = 100$ K and $T = 5$ K (Fig. 4.9) indicates several new modes in the low-temperature phase of NaV_2O_5 [362]. In addition, a step-like decrease of the background scattering intensity is observed for frequencies $\Delta\omega < 120\ \mathrm{cm}^{-1} = 83.5$ K. This marks

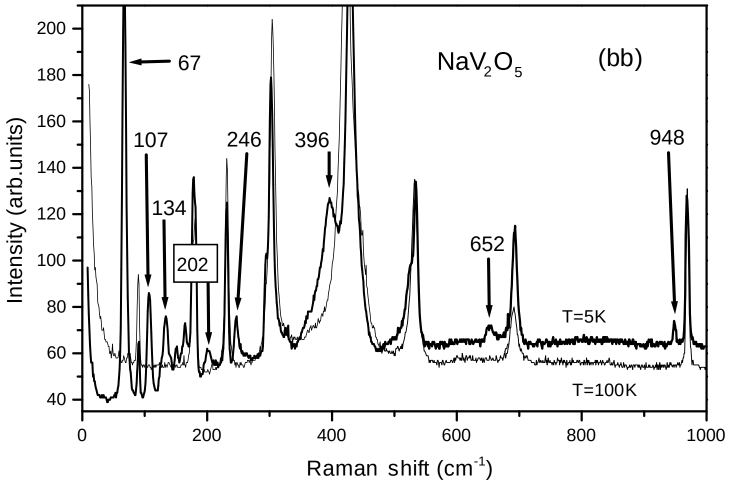

Fig. 4.9. Raman light scattering spectra of NaV_2O_5 at $T = 100$ and 5 K in intraladder (*bb*) polarization. The additional modes in the low-temperature phase are marked [362].

the onset of a gap with $\Delta_{01} = 86$ K. This value is smaller than $\Delta_{01}^{\mathbf{k}_{AF}} = 115$ K for $\mathbf{k}_{AF} = (h, 1/2, 0)$ and h = integer, but is comparable to $\Delta_{01}^{h,1/2,0} = 89$ K with h = half-integer observed in neutron scattering [373,374].

In Fig. 4.10 the intensity and linewidth of selected modes visible in the low-temperature phase are displayed as function of temperature [362]. Three low-energy modes at 67, 107, and 134 cm^{-1} have a particular temperature dependence of the intensity comparable with dimerization-induced phonon modes. The intensity increases more gradually upon cooling, with a smaller slope. No saturation in intensity is observed toward lowest temperature. Additionally, these three modes strongly broaden and soften slightly toward lower frequencies approaching T_{SP} from below. In contrast, the modes at 202, 246, and 948 cm^{-1} follow the scheme of zone-folded phonons. They neither show any broadening nor any shift in frequency as they become Raman active due to the lowering of the symmetry for $T \leqslant T_{SP}$.

Selection rules and magnetic field dependence. An analysis of the selection rules of the Raman modes, given in Fig. 4.11, shows, however, that the bound state candidates with the exception of the mode at 107 cm^{-1} are of mixed symmetry, i.e. the 67 and 134 cm^{-1}-modes appear in interchain (*aa*) as well as intrachain (*bb*) and crossed (*ab*) polarizations [362]. The 107 cm^{-1}-mode is observed only in intrachain (*bb*) polarization. The latter would be the preferable polarization selection rule of a magnetic bound state in a model spin chain. With $\Delta_{01} = 85\ K \equiv 60\ cm^{-1}$ from susceptibility measurements these three low-energy modes are situated below or near $2\Delta_{01} = 120\ cm^{-1}$. This gap value is also confirmed in the Raman light scattering experiments as a drop in the background intensity. As the number and selection rules of the singlet bound states differ from what has been observed in $CuGeO_3$ we will carefully check this assignment.

In view of the very close energy of the 67 cm^{-1}-mode to the singlet–triplet energy gap ($\Delta_{01} = 60\ cm^{-1}$), this mode might be one-magnon scattering allowed due to spin–orbit coupling [436]. However, the g-value in NaV_2O_5 is even closer to 2 than in $CuGeO_3$ [207,437], pointing to

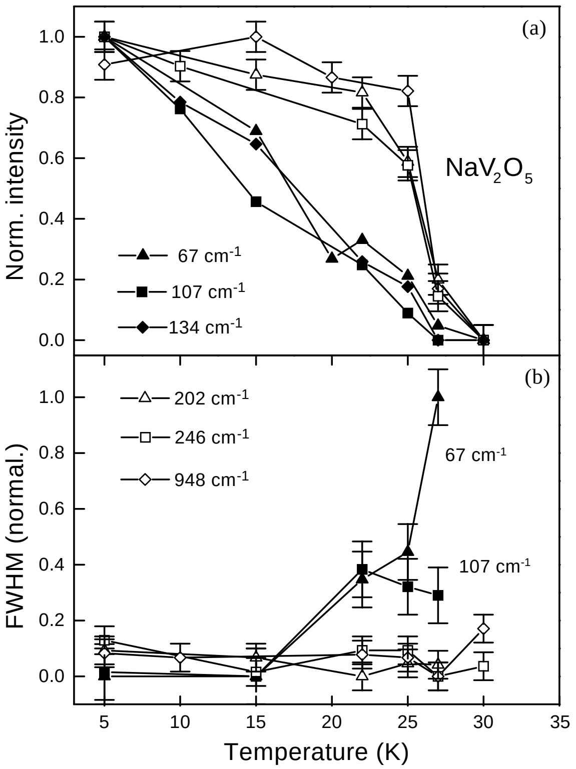

Fig. 4.10. (a) Integrated intensity of selected transition-induced modes observed in NaV_2O_5 for temperatures below T_{SP} and (b) normalized half-width (FWHM) of the additional modes as function of temperature [362].

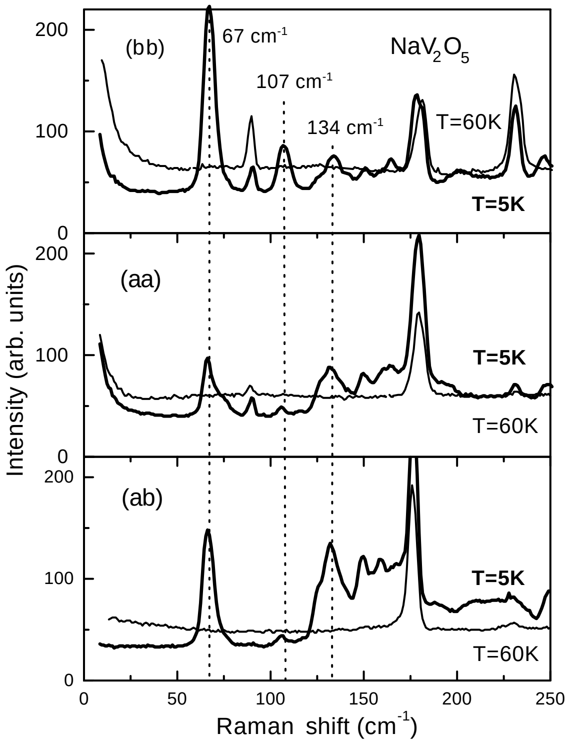

Fig. 4.11. Low-energy Raman light scattering spectra of NaV_2O_5 for three light scattering polarizations in the *ab* plane of the single crystal [362].

a negligible orbital momentum in this compound. Recently, however, a combination of the electronic structure and the DM interaction, allowed by symmetry in this material, has been discussed to describe a observable Raman cross-section of one- and two-magnon scattering [438].

Applying a magnetic field may lift the three times degeneracy of a triplet state resulting in a splitting or shift of the 67 cm^{-1}-mode. As shown in Fig. 4.12 neither a shift, a splitting, nor even a broadening of this mode in a field up to 7 T is observed [189]. Therefore, a simple one-magnon interpretation has been ruled out. In a similar approach the mode at 134 cm^{-1} has been identified as the corresponding two-magnon scattering [439]. This, however, would be surprising. Already in two-dimensional spin systems two-magnon scattering is strongly renormalized to lower frequencies due to magnon–magnon interaction.

Coherent magnetic oscillations and time-resolved probes. New excitations related to the magnetic system of NaV_2O_5 have recently been observed in pump–probe femtosecond time-domain spectroscopy. A mode at 127 cm^{-1}, corresponding to an energy nearly twice the spin gap, is attributed to a bound state. The selection rule of the coherent oscillation following from the circular polarized

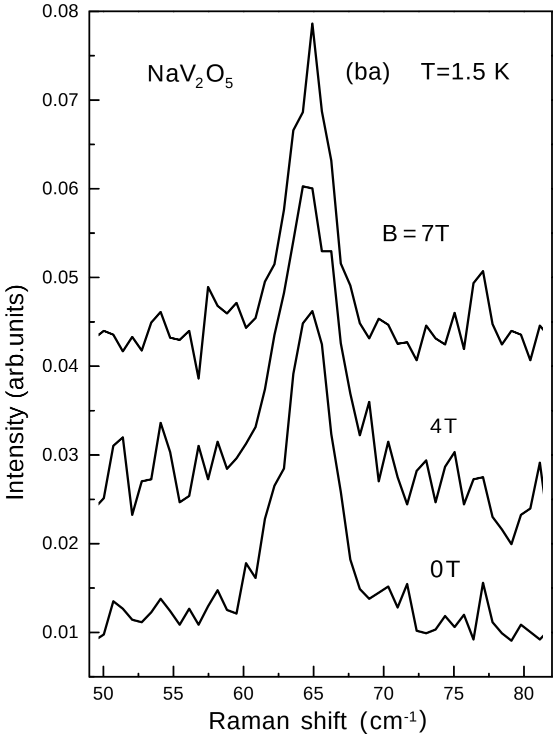

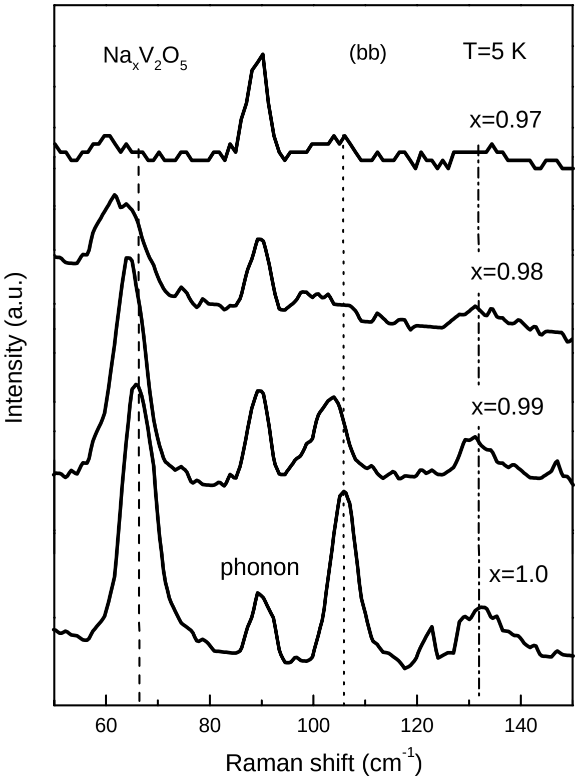

Fig. 4.12. Magnetic field dependence of the Raman mode at 67 cm^{-1} of NaV$_2$O$_5$ in crossed (*ba*) light scattering polarization. No splitting or broadening in a field up to 7 T is observed [189].

Fig. 4.13. Effect of Na deficiency in NaV$_2$O$_5$, with $x = 0.97$–1 on Raman light scattering spectra in intrachain (*bb*) polarization [445,446].

light used for the pump or probe beam points to its origin in a spin-flip excitation from the singlet ground state [440]. Other excitation at 90.6, 181, 230, 303, 420, 450 and 531 agree within 3 cm^{-1} with phonons observed in Raman scattering. In the pump–probe experiments they show different temperature dependencies and selection rules as the bound state at 127 cm^{-1}.

The application of this and other time-resolved techniques is at present rather limited. Exciting results exits for the 1D spin chain system Sr$_2$CuO$_3$, were an instantaneous photoinduced absorption and picosecond recovery due to very large dipole coupling between nearly degenerate one and two-photon states is observed. These effects are based on the electronic properties of the 1D Mott insulator [157]. Further investigations on other strongly correlated and low-dimensional systems are under way.

Phonon-related bound states. Also phonon-related bound states may be considered. Indeed, such phenomena were observed for example in YbS [441–443]. These modes were interpreted as excitons interacting with a LO phonon at ω_0 giving rise to exciton–phonon bound states with frequencies $\omega = n \cdot \omega_0$, with integer n. The polarization selection rules are identical with the LO phonon. Finally, the linewidth of these phonon bound states is a linear function of n. Integer multiples of excitation energies can be found in NaV_2O_5 by assuming an ω_0 of about $30\,cm^{-1}$. However, no such mode could be detected in light scattering experiments. Besides, the light scattering intensity of the bound states in NaV_2O_5 appears not only in the fully symmetric scattering components (aa), (bb), but also in the crossed (ab) component. A similar disagreement is found for the linewidth that does not show a systematic broadening. Also the scenario of folded phonons with an additional coupling to the spin and charge degrees of freedom has been discussed. Recent infrared absorption studies on NaV_2O_5 showing numerous modes with partly weak intensity in close proximity to the Raman excitations follow a similar route [444]. These approaches are to the present understanding not compatible with results from temperature and substitution studies. Summarizing, the experimental results in NaV_2O_5 are not compatible with an approach based on phonon bound states.

4.2.2. Deficiency and substitutions on the Na site

One of the most subtle problems preparing $Na_xV_2O_5$ samples is to control the Na content x [199,447]. Deviations from the nominal stoichiometry result in a shift of the ratio between V^{4+} and V^{5+} toward the non-magnetic ($s = 0$) V^{5+}. This leads to an effective substitution. Further possible substitutions in NaV_2O_5 are Li and Ca substitution on the Na site [199]. Systematic studies of Na deficiencies, as reported in Refs. [200,367], indeed show that the drop in the magnetic susceptibility is suppressed and T_{SP} is slightly shifted toward lower temperatures. Therefore, this Na-deficiency is also a promising tool to discuss the bound states.

A direct comparison of spectra with $x = 0.97$–1 in intrachain (bb) scattering configuration is displayed in Fig. 4.13 [445,446]. Solely, the three bound states show a considerable shift in frequency and a strong broadening. The zone-folded phonon modes do not show this shift toward lower frequencies. The frequency shift of the bound states is quite naturally explained by assuming that the Na deficiency leads to a reduced singlet–triplet gap and hence to a smaller energy of the magnetic bound states.

For Li substitution on the Na site a similar but somewhat smaller shift of the bound states is observed. In Fig. 4.14 spectra of $Na_{1-x}Li_xV_2O_5$ are shown [445]. For larger Li concentration (7%) only a broad maximum remains of the bound state scattering contribution. It should be noted, that all magnetic bound states react in a similar way to the substitution while the effect on the phonon modes is weaker. These results are comparable to the effect of Zn substitution on the magnetic bound state in $CuGeO_3$ [328].

4.2.3. Theoretical considerations

Concluding the experimental data it is stated that the modes at 67, 107 and $134\,cm^{-1}$ are described best as singlet bound states. They, however, are not consistent in number as well as in selection rules with the excitation spectrum of a frustrated and dimerized 1D Heisenberg chain, which exhibits one singlet bound state. The intensity of this singlet bound state should only be observed in intrachain scattering configuration, i.e. with light scattering polarization parallel to the dominant exchange path.

In the high-temperature phase ($T \geqslant T_{SP}$) NaV_2O_5 is described as a quarter-filled ladder with charge degrees of freedom. However, since the charge transfer gap $\Delta_{CT} \approx 1$ eV is large, the low-energy excitations are dominated by spin fluctuations of one spin per rung along the ladder direction. This leads to a mapping of the system on a spin 1/2 Heisenberg chain [287]. Actually, the mode at

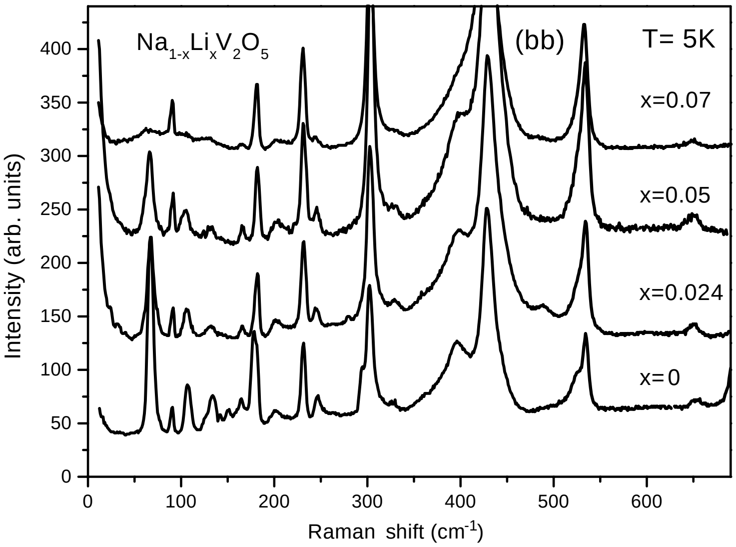

Fig. 4.14. Effect of Li substitution in $Na_{1-x}Li_xV_2O_5$, with $x = 0$–0.07, on Raman light scattering spectra in intrachain (*bb*) polarization [445].

$107\ cm^{-1} = 1.78 \times \Delta_{01}$ is consistent both in selection rule and energy with the singlet bound state in $CuGeO_3$ ($30\ cm^{-1} = 1.78 \times \Delta_{01}$). Therefore, we identify this mode as the singlet bound state of an effective chain.

To describe the two unpolarized bound states, a quasi-2D system or a cluster model [398,448] in the *ab* plane of the compound may be relevant. This means taking into consideration dimers parallel, perpendicular as well as diagonal to the ladder. The observed bound states have a small energy separation compared to $\Delta_{CT} \approx 1$ eV. Actually, their energy scale is given by the singlet–triplet gap Δ_{01} [373,374]. Therefore, the character of the excitations is predominantly magnetic allowing a description of the bound states in the context of a pure spin model.

The analogy of this situation to the dynamical Jahn–Teller effect motivated the proposal of a dynamic dimer formation as a ground state of the system [362,188]. The superposition of different energetically nearly degenerate dimer configurations may show up in the triplet channel of the excitation spectrum. This phenomenological approach, however, has later not been supported by synchrotron X-ray scattering experiments as the low-temperature phase showed only evidence for a static stacking disorder of zig-zag charge ordering patterns in NaV_2O_5 [359].

4.3. Bound states in $(VO)_2P_2O_7$

The compound $(VO)_2P_2O_7$ was for many years a canonical example for a spin ladder compound (see Section 2.5.2). Only recently neutron scattering experiments on single crystals have determined that the dominant exchange path is along the *b*-axis direction. In addition, *two* strongly dispersing triplet modes ($\Delta_{01} = 25\ cm^{-1}$ and $\Delta'_{01} = 46\ cm^{-1}$) have been observed. The second mode has been interpreted as the triplet bound state of an alternating spin chain [217]. The experimental spectral weight of both modes has been found to be comparable. However, no triplet continuum has been

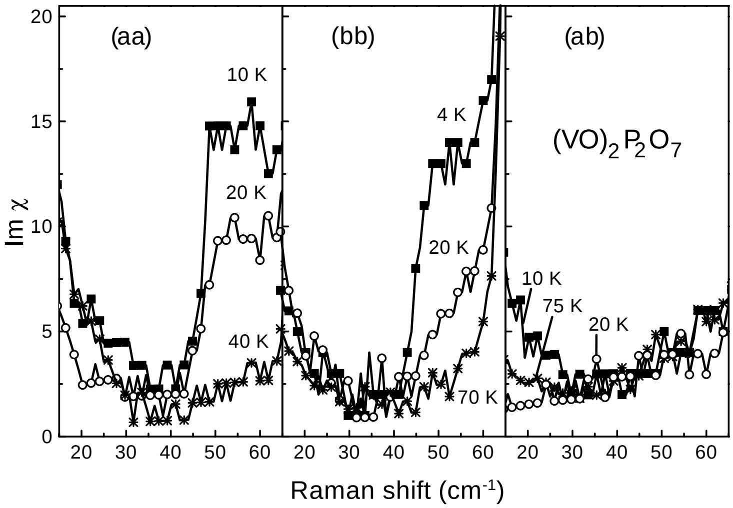

Fig. 4.15. Low-energy Raman scattering in $(VO)_2P_2O_7$ with light scattering polarizations in the *ab* plane. The spectra are corrected by the Bose factor. A shoulder with an onset at 45 cm^{-1} is observed in intrachain (*bb*) as well as interchain (*aa*) polarization [214,449].

observed like in $CuGeO_3$ [319]. To clarify which model applies, such as a purely 1D magnetic chain, frustration or a more complicated scenario including spin–phonon coupling, other spectroscopic information together with theoretical modelling is needed.

In calculations using a "simple" alternating spin chain the spectral weight of the triplet bound states has been found to be restricted to a limited part of the Brillouin zone. This result is in contrast to the experimental neutron scattering observations [222] and motivated two refined theoretical studies taking an additional diagonal coupling (frustration) via the phosphate group into account [31,223]. With this approach a much better description of the neutron scattering experiments has been achieved. In addition, a singlet bound states with $\Delta_{00}^{k=0} = 1.68\Delta_{01} = 42$ cm^{-1} has been postulated [223]. Concluding, a frustrated quasi-2D spin model might describe the excitations observed in neutron scattering experiments with respect to their energy and spectral weight across the whole Brillouin zone.

In Raman light scattering experiments a shoulder of the scattering intensity is observed at low temperatures with an onset at 45 cm^{-1}, an energy only slightly renormalized with respect to $2\Delta_{01} = 50$ cm^{-1} determined by neutron scattering experiments (see Fig. 4.15) [214,217,449]. This intensity is masked at higher energy ($\Delta\omega > 60$ cm^{-1}) by phonon scattering and shows up with light polarizations both parallel and perpendicular to the dominant exchange direction. It is not observed in crossed light polarization. This excludes two-magnon scattering of an usual 2D spin system. As no splitting or shift of the shoulder is evident in an applied magnetic field, one-magnon scattering is excluded [214,449]. A later Raman study on $(VO)_2P_2O_7$ showed evidence for a peak at 90 cm^{-1} and attributed this mode to the second gap [224].

The shoulder at 45 cm^{-1} is observed for $T < 50$ K in interchain (*aa*) polarization and for $T < 75$ K $\approx 2\Delta_{01}$ in intrachain (*bb*) polarization. This temperature is comparable to the size of the gap itself (see Fig. 4.16). The intensity of this shoulder shows a linear increase with decreasing temperature

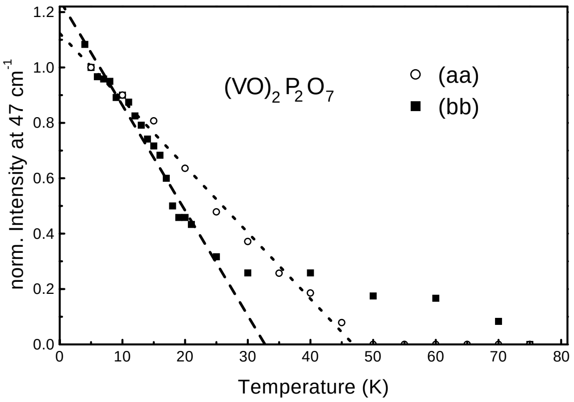

Fig. 4.16. Normalized intensity of the Raman scattering at 47 cm^{-1} with respect to the intensity at lower frequency in $(VO)_2P_2O_7$ as function of temperature. Open circles: (*aa*) light polarization; black squares: (*bb*) light polarization [214].

comparable to the bound states in NaV_2O_5 or $CuGeO_3$. All these observations allow an assignment of this shoulder to a singlet bound state with a negligible binding energy. As this binding is weaker than predicted for the frustrated quasi-2D spin system, a purely magnetic model for the excitation spectrum in $(VO)_2P_2O_7$ may not be appropriate. The observed anomalies of phonons, with energies close to the magnetic excitations, point to this alternative direction (see Section 2.5.2). Theoretically, phonon- or magnetoelasticity-induced bound state phenomena are expected if optical phonon modes have an energy close to the magnetic spectrum of the compound [33–35]. This scenario might be relevant for the case of $(VO)_2P_2O_7$.

4.4. Bound states in $SrCu_2(BO_3)_2$

Low-energy light scattering in $SrCu_2(BO_3)_2$ exhibits a drastic evolution with decreasing temperature [124]. Quasielastic scattering observed at high temperatures ($T > \Delta_{01}$) is replaced by a broad two-magnon-like continuum centered near 50 cm^{-1}. The selection rules of these intensities yield B_2 symmetry, i.e. the light polarization vectors along (*ab*) connect next nearest dimers within the *ab* plane of the compound [124]. In this polarization no Raman scattering process from the dimer ground state is allowed [118,428]. The observed scattering intensity is therefore due to scattering on thermally induced and strongly localized triplet states of the Shastry–Sutherland lattice. Consequently for $T \to 0$ all scattering is suppressed in this geometry due to the large spin gap (see Fig. 4.17). The temperature dependencies can be mapped on thermodynamic data, such as the magnetic susceptibility and the specific heat of the spin system as shown in Fig. 4.18.

The temperature dependence of the intensity of the 30-cm^{-1} bound state is shown in Fig. 4.18(a). The solid line is a fit based on the strong damping of this state due to scattering on thermally excited triplet states. The decrease of the scattering intensity I_B with temperature is governed by the density of excitations and follows the equation $I_B(T) \propto (1 - Ae^{-\Delta/k_BT})$, where A is a constant. A reasonable agreement is found with only one free parameter ($A = 215.7$) and fixing $\Delta = 34$ K from experimental data. In Fig. 4.18(b) the temperature dependence of the continuum between 20 and 80 cm^{-1} is well described by the temperature-dependent susceptibility [107]. In (c) the quasielastic

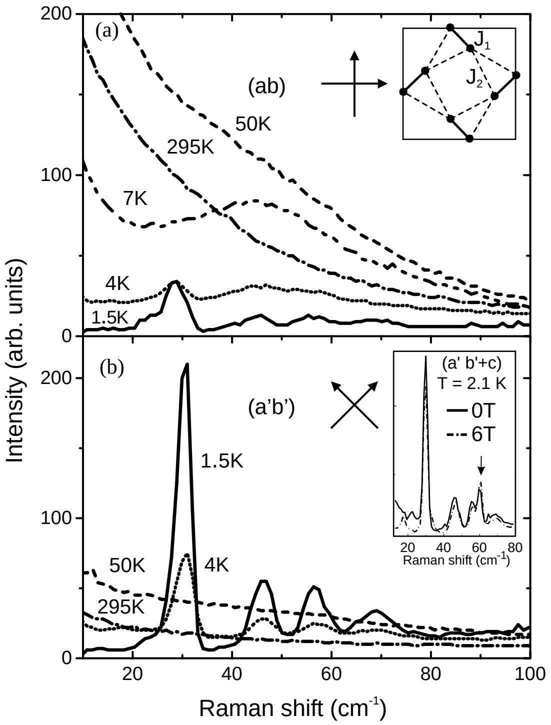

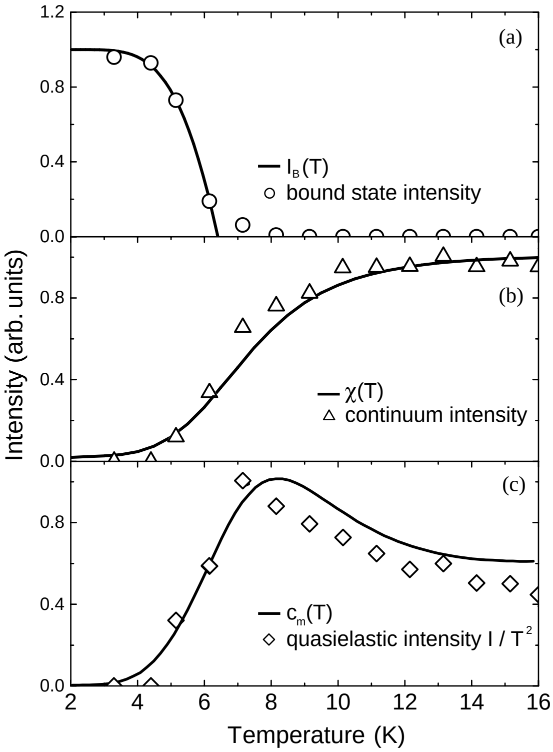

Fig. 4.17. Raman spectra of $SrCu_2(BO_3)_2$ in two scattering geometries: (a) light polarization (ab) and (b) rotated by 45°, i.e. ($a'b'$). The upper inset shows Cu-dimers of 1/4 of the unit cell. The respective polarization (arrows) of incident and scattered light is given with respect to the crystallographic axes. The lower inset shows spectra for $B=0$ (full line) and 6 T (dotted line) in ($a'b'+c$) polarization. An additional A_g-phonon is marked by an arrow [124].

Fig. 4.18. Mapping of the temperature dependence of normalized Raman scattering intensities (open symbols) of the bound states, the intensity of the continuum and of the quasielastic scattering on thermodynamic quantities (lines) [124].

magnetic scattering intensity divided by T^2 is well described by the specific heat according to Eq. (5.1) in Section 5 [108].

It is noteworthy that a mapping of the intensity of the Raman scattering continuum on the magnetic susceptibility also works for the frustrated spin chain system $CuGeO_3$ and corresponds to replacing a four-spin correlation function by a two-spin function [124]. The theoretical implications of this experimental evidence that has not been investigated so far.

For very low temperatures compared with the spin gap ($T \ll \Delta_{01}$) four well-defined modes with energies Δ^i_{00}=30, 46, 56 and 70 cm^{-1} appear. A refined analysis discovered a further broadened mode centered around 100 cm^{-1} [109]. These excitations are primarily observed in the ($a'b'$) scattering configuration corresponding to B_1 symmetry selection rules and polarization vectors that connect nearest dimers. Only this scattering geometry allows exchange Raman scattering on the Shastry–Sutherland lattice if no excited triplet states are present. The modes neither split nor shift in an applied magnetic field up to 6 T as shown in the inset of Fig. 4.17. In (ab) polarization two weaker shoulders of intensity appear near 25 and 40 cm^{-1} for $T \ll \Delta_{01}$. The frequencies of these modes are identical to the triplet excitations observed in neutron scattering and ESR (24.5 and 40 cm^{-1}). Applying a magnetic field, at least for the former mode a definite shift corresponding to the triplet nature of the underlying excitation has been detected.

If the above mentioned modes are normalized to the energy of the singlet–triplet gap $\Delta_{01} = 24.5$ cm^{-1} they correspond to ratios of $1.25\Delta_{01}$–$2.9\Delta_{01}$. The sequence of modes is astonishingly similar to the reduced energy of low-temperature modes found in $CuGeO_3$ ($1.78\Delta_{01}$) and NaV_2O_5 ($1.1\Delta_{01}$, $1.78\Delta_{01}$ and $2.2\Delta_{01}$). Therefore, and as the triplet excitations in $SrCu_2(BO_3)_2$ are even more localized and strongly interacting compared with frustrated spin chains, all above given modes are assigned to magnetic bound states [124]. Several theoretical studies of the magnetic excitation spectrum support this interpretation [118,427,428].

4.4.1. Effect of substitutions

Comparing the behavior of $SrCu_2(BO_3)_2$ with other quantum spin system it is obvious that here the triplet excitations are even stronger spatially localized and the spin–spin correlation length is extremely small. As shown in the previous sections substitution experiments are a sensitive probe to this degree of localization. Furthermore and related to this question, the phase diagram of this compound and the assumed proximity of $SrCu_2(BO_3)_2$ to a Néel phase opens the up the chance to study quantum criticality. Here Zn substitutions inducing spin vacancies in the system might help at least to shift the compound into the cross over regime.

Several substitution studies have been performed by H. Kageyama and Yu. Ueda, ISSP Tokyo using Zn substitutions on the Cu site to induce spin vacancies. Furthermore the effect of Ba and Ca substitution on the Sr site has been studied. The latter, in a certain solubility window, decreases or increases the crystallographic c-axis and the distance of the $CuBO_3$ planes, respectively. The results of these studies are easy to summarize: No decrease of the spin gap or emergence of an antiferromagnetic instability has been observed. Instead a defect-induced low-temperature Curie-tail is induced together with a flattening of the plateaus in high-field magnetization [450].

In Fig. 4.19 the effect of Zn substitution on the low-energy Raman spectra of $SrCu_2(BO_3)_2$ are shown at three different temperatures, $T = 1.5$, 4 and 5 K, respectively [109]. Obviously the effect of the substitution on the excitation spectra is limited, only the intensities of the modes are reduced. In this sense this trivial effect of substitutions may be approximated by an effective increase of temperature. The non-existent energy shift is compatible with a constant and substitution-independent global magnitude of the spin gap. Only in a very limited concentration range an additional broad intensity at 16–18^{-1} is observed which might be related to a breaking of the translational invariance. All these experimental facts are well understood considering thermally and substitution-induced triplets as quasilocalized on each Cu dimer on the Shastry–Sutherland lattice. Therefore, substitutions locally switch off the spin gap without leading to a global effect on the singlet state.

4.4.2. Polarization dependence

The magnetic bound states in $SrCu_2(BO_3)_2$ are purely in-plane polarized. As shown in Fig. 4.20 scattering intensity appears only in (aa) and ($a'b'$) polarization. Furthermore in the investigated frequency range no additional interlayer bound states show up in (cc) polarization. The only scattering intensity observed in this spectral range is a phonon with a large anharmonicity. This interlayer

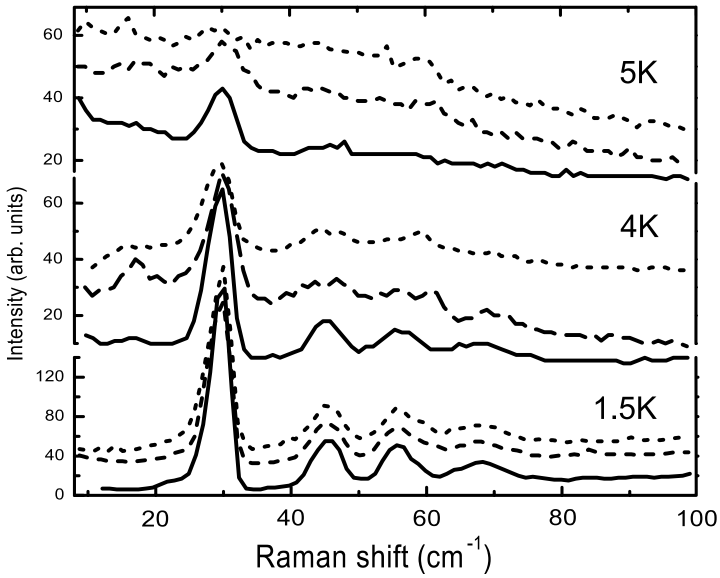

Fig. 4.19. Low-energy Raman scattering of Zn-substituted $Sr(Cu_{1-x},Zn_x)_2(BO_3)_2$ in $(a'b')$ polarization at 1.5, 4 and 5 K [109]. The measurements with $x = 0$ (full line), $x = 0.01$ (dashed) and 0.02 (dotted) are vertically displaced for clarity.

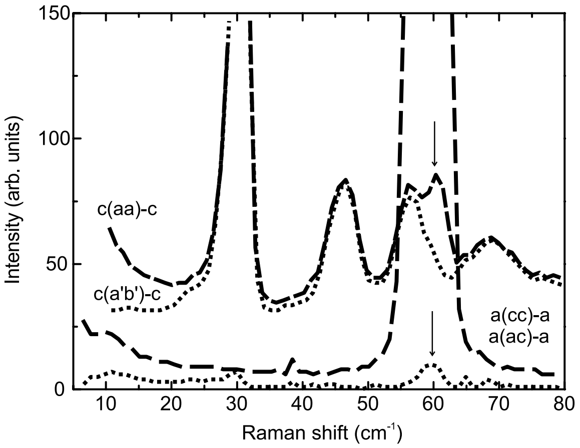

Fig. 4.20. Low-energy Raman scattering for $SrCu_2(BO_3)_2$ in interlayer and intralayer polarizations at $T = 1.6$ K. The measurements in intralayer polarizations are vertically displaced upwards for clarity. The (aa), (cc) and (ac) polarizations show an additional phonon mode marked by an arrow. No evidence for additional interlayer modes is found [109].

phonon mode with a frequency of $58\ \mathrm{cm}^{-1}$ at $T = 4$ K is discussed further in Section 2.3.2 (see Fig. 2.15). It is related to a structural phase transition at $T = 395$ K [125]. Its anharmonicity and its energy comparable to the spin system might induce an enhancement of the spin–phonon interaction. Further investigations of both experimental and theoretical nature are underway.

5. Quasielastic scattering in low-dimensional spin systems

Raman spectra of several magnetic systems show quasielastic light scattering as a strongly broadened central peak with Lorentzian or Gaussian lineshape and with specific selection rules. A canonical example for 3D AF spin systems is the cubic, quasi-isotropic compound $KNiF_3$ in which magnetic energy fluctuations for temperatures close to the Néel ordering (T_N=248.5 K) give rise to quasielastic scattering [452].

In low-dimensional spin systems quasielastic scattering is a very general feature, too. The temperature dependence of this intensity can be used to characterize the low-energy excitations of the system. It is especially sensitive to the opening of a spin gap and can be very useful to determine the magnetic part of the specific heat. In direct measurements of the specific heat very often the lattice degrees of freedom dominate the magnetic part. Spin systems investigated so far are the "pure" spin chain $KCuF_3$ [227], the charge ordered rare earth spin chain Yb_4As_3 [175], the spin-Peierls compound $CuGeO_3$ [451], the alternating spin chain system $(VO)_2P_2O_7$ [214], the quarter-filled spin ladder NaV_2O_5, [189] and very recently the strongly frustrated 2D spin dimer compound $SrCu_2(BO_3)_2$ [124,453].

In compounds with a dimerization transition (T_{SP}) the coupling to optical phonons leads to fluctuation contributions that are observed for temperatures slightly above T_{SP}. This quasielastic scattering is considered to redistribute its spectral weight to soliton bound states ($T < T_{SP}$) [315] and to be connected to the non-observance of soft modes at the transition [316].

In the above-mentioned 1D spin systems quasielastic scattering should only be observed in intrachain scattering configuration, i.e. with the light polarization parallel to the effective chain direction. A comparison of different scattering geometries including right angle scattering in $CuGeO_3$ is shown in Fig. 5.1. Quasielastic scattering is indeed only observed in (*cc*), i.e. intrachain polarization. A similar investigation for NaV_2O_5 is shown in Fig. 2.44. Here quasielastic scattering is also observed only in intraladder (*bb*) polarization [189,362].

In this sense $(VO)_2P_2O_7$ seems to be an exception since quasielastic scattering is primarily observed in interchain (*aa*) polarization. In *a*-axis direction neutron scattering data give evidence only for a flat ferromagnetic dispersion compared to the steep antiferromagnetic dispersion along the *b*-axis. Uhrig and Normand [31] proposed a quasi-2D model with an additional diagonal AF exchange for $(VO)_2P_2O_7$. The 2D spin dimer compound $SrCu_2(BO_3)_2$ shows this scattering contribution in (*ab*) configuration, i.e. in polarization yielding B_2 symmetry [124]. These results are described and analyzed in Section 4.4 (see Figs. 4.17(a) and 4.18) together with other magnetic scattering contributions. The experimentally observed spectral weight of the quasielastic scattering contribution shows generally a strong increase with increasing temperature. In the same temperature range the magnetic contribution to the specific heat has a maximum.

The quasielastic scattering has been explained within two different scenarios: Spin diffusion [454,455] that is forbidden in perfect 1D spin systems and would lead to a Gaussian lineshape of the central line [456] or fluctuations of the energy density of the spin system [457]. The latter mechanism leads to a Lorentzian spectral function and is important for systems with non-negligible spin–phonon coupling. The energy of a magnetic system is not constant, but fluctuates about its mean value [458]. Already a weak spin–phonon coupling increases the spectral weight of these fluctuations as it decreases their time scale.

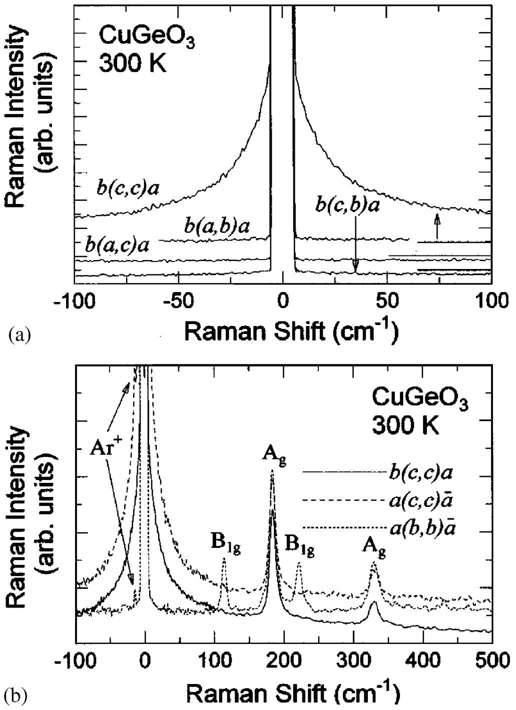

Fig. 5.1. Symmetry analysis of quasielastic light scattering in $CuGeO_3$. (a) for the frequency range −100 to 100 cm^{-1} and (b) for the frequency range −100 to 500 cm^{-1} in right angle scattering geometry [451].

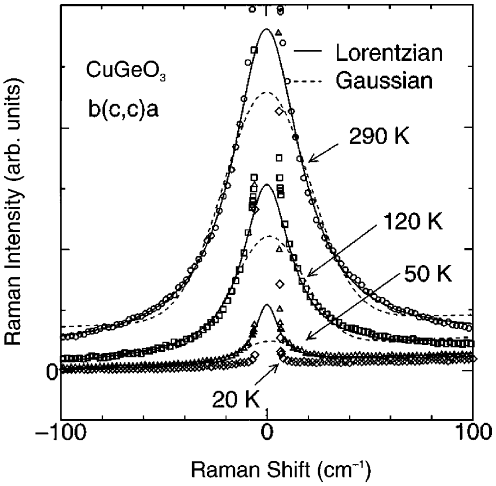

Fig. 5.2. Quasielastic light scattering in $CuGeO_3$ for intrachain (*cc*) polarization and different temperatures [451].

In Fig. 5.2 a Raman experiment of $CuGeO_3$ displays quasielastic scattering as function of temperature [451]. In this compound very strong spin–phonon coupling is evident for two phonon branches [306]. Therefore, the Lorentzian spectral function leads to a very good description of the data. For smaller temperatures the intensity of the scattering contribution is diminished as the fluctuations are suppressed.

From this quasielastic light scattering intensity one can easily deduce the magnetic contribution to the specific heat, C_m. This analysis has been performed for $KCuF_3$ [227], $CuGeO_3$ [451] and $(VO)_2P_2O_7$ [214]. Therefore, we briefly summarize the theory of Reiter and Halley [457,458].

The scattering intensity can be calculated using the Fourier components of a correlation function of the magnetic energy density. For high temperatures and hydrodynamic conditions this function can be simplified leading to an expression that connects the scattering intensity with the magnetic specific heat C_m:

$$I(\omega) \propto \frac{C_m T^2 D_T k^2}{\omega^2 + (D_T k^2)^2} , \tag{5.1}$$

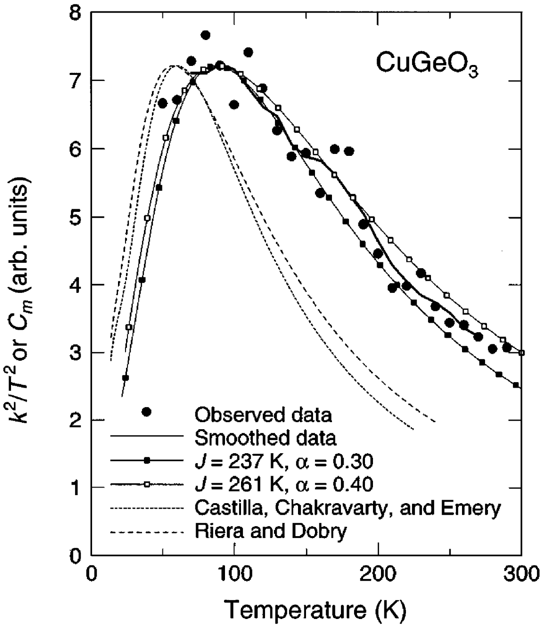

Fig. 5.3. Analysis of the quasielastic light scattering in $CuGeO_3$ in terms of the magnetic specific heat C_m [451]. The data (black dots) are smoothed (line) and then compared with calculations using the given coupling constants. The dotted and dashed lines correspond to $J = 150$ K and $\alpha = 0.24$ [294] or $J = 160$ K and $\alpha = 0.36$ [293].

with $D_T = K/C_m$ the thermal diffusion coefficient, K the magnetic thermal conductivity, and $\omega \sim D_T k^2 \ll \omega_0$ leading to $k \simeq 2k_0 \sin\theta/2$, with θ the scattering angle, and ω_0, k_0 characterized by the incident light.

Analyzing experiments using Eq. (5.1) the scattering background is assumed to be constant. Especially contributions from Rayleigh scattering should be reduced using a suitable experimental setup and scattering geometry. For transparent samples right angle scattering geometry is most favorable. In Fig. 5.3 results for $CuGeO_3$ in 90° scattering geometry are shown. The resulting C_m has been compared with theoretical models considering frustrated spin chains [451]. A qualitative agreement with the exchange coupling and the frustration parameter from thermodynamic experiments [297,298] has been obtained.

In Raman experiments on $(VO)_2P_2O_7$ strong phonon anomalies have been observed for modes with energies comparable to the magnetic excitation spectrum. Therefore, assuming strong spin–phonon coupling, the existence of fluctuations of the energy density seems reasonable in this compound. For a comprehensive discussion we refer to Section 2.5.

Indeed, quasielastic scattering is observed in interchain (aa) scattering configuration. The respective data are shown in Fig. 5.4. This intensity strongly decreases with lowering temperature. Calculations using a Lorentzian and a Gaussian lineshape are given in this figure as a solid and a dashed line, respectively. The maxima observed near 60 and 70 cm^{-1} are due to phonon scattering and should be ignored here.

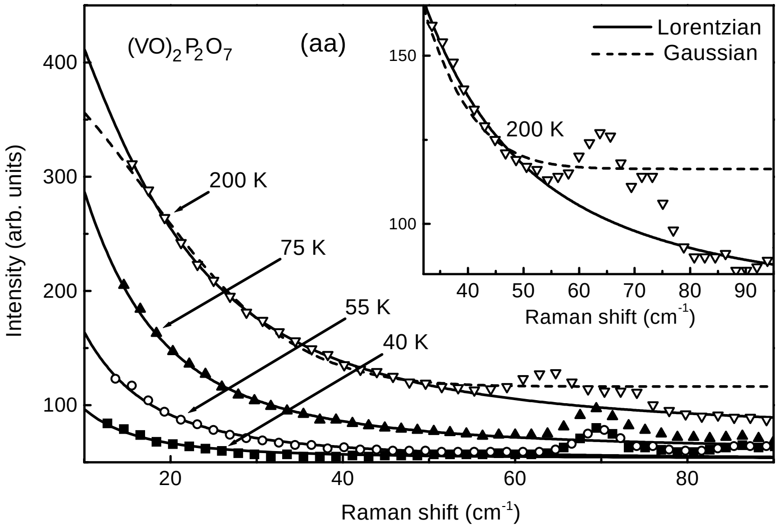

Fig. 5.4. Quasielastic scattering intensity in $(VO)_2P_2O_7$ determined in interchain (*aa*) polarization for different temperatures. The dashed and solid line show a calculation using a Gaussian and Lorentzian lineshape, respectively [214]. The inset is an enlarged view of the data for $T = 200$ K.

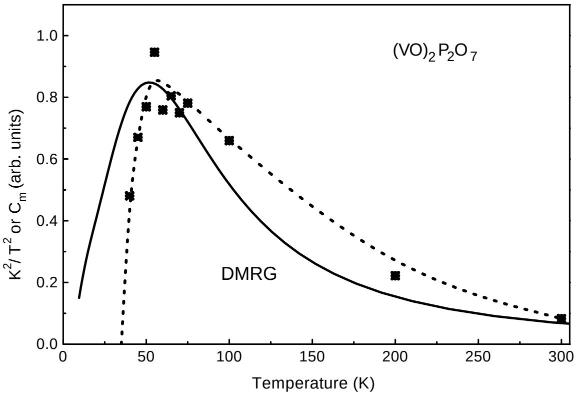

Fig. 5.5. Specific heat of $(VO)_2P_2O_7$ (black squares) determined from quasielastic light scattering shown in Fig. 5.4. The dashed curve is a guide to the eye. The full curve is a DMRG calculation of the specific heat of an alternating Heisenberg chain [214,215].

Following the arguments given above the magnetic specific heat was determined from the quasielastic scattering using Eq. (5.1). The result is shown in Fig. 5.5 [214]. A direct measurement of this quantity is not yet available. However, DMRG calculations [225] of the magnetic specific heat with the parameters $J = 110$ K and $\delta = 0.09$ K are shown for comparison in the same figure. The maximum of the magnetic specific heat determined by light scattering experiments is at $T_{\max} = 55$ K. The corresponding maximum in the magnetic susceptibility is at 74 K [221]. The DMRG calculation for a strongly alternating Heisenberg chain agrees well with the experimental data.

This supports the scenario of $(VO)_2P_2O_7$ as an alternating chain system with considerable spin–phonon coupling.

6. Conclusions and outlook

Over the past decade the understanding of low-dimensional strongly correlated electron systems improved enormously. From the experimental side this is related to the significant progress made in materials science of complex transition-metal oxides. Indeed, quantum spin systems with chain, ladder, depleted-planar, and other exchange geometries have been designed and investigated. One motivation for these studies has been the possible connection between high-temperature superconductivity and low dimensionality. In the undoped and insulating parent compounds of the high-temperature superconductors long-range Néel order is observed. To get more insight in the suppression of antiferromagnetic long-range order upon doping, spin liquids, such as, e.g., one-dimensional half-filled spin systems with the above given topologies have been studied. In these model-type systems long-range order is suppressed without doping.

The compound $Sr_{14-x}Ca_xCu_{24}O_{41}$ shows indeed superconductivity under pressure. The spin gaps of the ladders and the dimerized chains agree well with the behavior expected for low-dimensional spin systems. A suppression of the Raman scattering intensity has been found for frequencies below 200 and 490 cm^{-1}. These frequencies correspond to the doubled singlet–triplet gaps of the chain and the ladder sublattice, respectively. Upon Ca substitution the electronic properties of $Sr_{14-x}Ca_xCu_{24}O_{41}$ cross over into a 2D regime. Still, Raman and neutron scattering experiments undoubtedly prove that the magnitude of the spin gap in the ladders is preserved. Charge ordering in the dimerized chains is observed in Raman scattering as a shift of a phonon mode and the appearance of additional side bands. Upon substitution these phonon anomalies and the gap feature are suppressed in the Raman spectra. Taking into account a charge transfer from the chains to the ladders with increasing Ca substitution makes this effect understandable as it suspends the dimerization of the chains. Much attention has been devoted to NMR on $Sr_{14-x}Ca_xCu_{24}O_{41}$ under applied pressure. These investigations claim a change of the ladder gap from a distinct gap to a “pseudo-spin gap”. However, NMR data at ambient pressure as a function of Ca substitution are already in conflict with Raman and neutron scattering experiments. This may be due to a higher sensitivity of NMR to incoherent low-energy states. These states may exist either due to structural defects or mobile carriers. To clarify this problem, further spectroscopic experiments under pressure are needed. Summarizing the present status, most experimental results including Raman scattering are in favor of a preserved spin gap and low dimensionality of the ladder sublattice in the doped system. A situation of similar complexity that is also linked to the problem of a doped quantum spin system is realized in NaV_2O_5. Raman scattering experiments in this compound point to charge ordering with an onset at higher temperatures ($T_{CO} = 80$ K) than the subsequent dimerization transition ($T_{SP} = 34$ K). The observed phonon anomalies point to a temperature scale (T_{CO}/T_{SP}) of this effect that is comparable to the 1D stripe formation in the nickelate La_2NiO_4. The polarization selection rules of the magnetic bound states in NaV_2O_5 support the proposed zigzag charge ordering.

A further interesting realization of a spin liquid is given in the two-dimensional compounds CaV_4O_9 and $SrCu_2(BO_3)_2$. In these systems spin gaps exist due to their exotic exchange topologies. Theoretical studies on 1/5-depleted square lattices and the orthogonal dimer (Shastry–Sutherland) lattice indeed proposed a manifold of possible singlet ground states and a rich excitation spectrum. Experimentally the gap formation and triplet bound states were observed in ESR, NMR and neutron scattering. In $SrCu_2(BO_3)_2$ a multitude of singlet bound states was detected in light scattering experiments. The observed polarization selection rules of these modes and quasielastic scattering (at higher temperatures) reflect the two-dimensional nature of the underlying spin–spin correlations. This reflects the two-dimensional nature of the underlying spin–spin correlations. In the one-dimensional spin systems discussed here the maximum energy of the bound states is restricted to the doubled singlet–triplet gap. This is not the case for $SrCu_2(BO_3)_2$ and is attributed to a strong frustration-induced localization of the triplets.

Light scattering experiments proved to be a versatile tool to investigate compounds that represent low-dimensional quantum spin systems. This is based on the high sensitivity and energy resolution on comparably small samples, and, furthermore on the specific symmetry information that may be gained from an analysis of the Raman scattering tensor. A further promising aspect of these experiments is the easier feasibility in which high hydrostatic pressure may be applied. This parameter may be used to increase the interchain interaction or the frustration of a spin system in a controlled way. Experimental investigations on pure and substituted $CuGeO_3$ found an increase of the frustration with pressure that leads to a “revival” of the spin-Peierls transition in the substituted compounds. Pressure studies will surely gain increased significance in the future. The observation of singlet bound states in light scattering experiments has opened up a new way of characterizing triplet–triplet interactions. These states can be regarded as the magnetic analogue to excitonic states in semiconductors. Magnetic light scattering as a spin conserving exchange process is complementary to magnetic neutron scattering in which these singlet bound states cannot be observed. Singlet bound states are now believed to be a general phenomenon in systems with a gapped excitation spectrum. From the theoretical side three approaches have been undertaken to understand the binding effect of triplets. Briefly, they may be characterized as taking into account frustration in dimerized magnetic systems, interchain interaction, or the important role of spin–phonon coupling. In the experimental data presented here the spectral weight and binding energy of the bound states were found to be dominated by frustration, e.g., due to next nearest neighbor exchange interaction in $CuGeO_3$, or by a complicated exchange topology in $SrCu_2(BO_3)_2$ and NaV_2O_5. The experimental identification of magnetic bound states is based on the investigation of the spectral weight and lineshape of the respective scattering intensity as function of dimerization, magnetic field and polarization selection rules. In all cases the spectral weight of the singlet bound states showed a linear increase with decreasing temperature. This characteristics is linked to their nature as bound two-particle states in a system with strong fluctuations and short-ranged spin–spin correlations. The spin-Peierls compound $CuGeO_3$ has been used as a model system in this respect. The singlet bound state observed here corresponds in energy, polarization selection rules and other properties exactly to the expected behavior of a frustrated alternating chain system. The importance of frustration is also highlighted by the observation of spinon scattering for $T > T_{SP}$. This scattering intensity is only allowed due to frustration. In the “pure” non-frustrated spin chain system $KCuF_3$ no corresponding signal was observed. In substituted $CuGeO_3$ the defect-induced dopant-bound spinon is observed in light scattering as a well-defined mode. This mode demonstrates distinctly the binding effect of spinons to a defect site. Finally, for the first time a three-magnon process was observed and successfully modelled as scattering from a thermally populated triplet branch to a higher lying one. It is noteworthy that this scattering process is lost in any bosonic description where only quadratic terms in the expansion of the Raman tensor in terms of the spin are kept. This process is a generic feature of gapfull low-dimensional spin liquids.

In summary, we provided an overview of selected aspects in the field of low-dimensional quantum spin systems. Most of the major issues discussed here were investigated using inelastic light scattering. This spectroscopy together with appropriate theoretical models undoubtedly gives important insight into interactions and will therefore also play an active role in the future. The physics of low-dimensional spin systems is an integral part of the field of strongly correlated electrons. It developed into a fascinating area of solid state physics and quantum magnetism in particular. Also in the more technologically relevant area of magnetism in reduced dimensions the basic understanding of electronic correlations and quantum spin systems achieved so far will prove to be important. Magnetic nanostructures scaled down to the quantum dot or molecular level will be crucial entities for quantum information processing.

Future developments that are difficult to foresee will surely lie in the materials science of new complex compounds. In this field the emerging use of preparation concepts as the "lone pair approach" and crystallographic database searching strategies are noticeable. These compounds might have similarly extraordinary properties as the high-temperature superconductors. The large number of very recently discovered or reinvestigated materials with exotic properties and unique magnetic exchange topologies point into this promising direction.

References

[1] A. Auerbach, Interacting Electrons and Quantum Magnetism, Graduate Texts in Contemporary Physics, Springer, New York, 1994; P. Fazekas, Lecture Notes on Electron Correlations and Magnetism, World Scientific, Singapore, 1999.
[2] N.D. Mermin, H. Wagner, Phys. Rev. Lett. 17 (1966) 1133.
[3] K. Yosida, Theory of Magnetism, Solid-State Sciences, Vol. 122, Springer, New York, 1996.
[4] H.A. Bethe, Z. Phys. 71 (1931) 205.
[5] J. des Cloizeaux, J.J. Pearson, Phys. Rev. 128 (1962) 2131.
[6] G.S. Uhrig, H.J. Schulz, Phys. Rev. B 54 (1996) R9624.
[7] R.B. Laughlin, Phys. Rev. Lett. 79 (1997) 1726.
[8] R.B. Laughlin, in: Y.M. Cho, J.B. Hong, C.N. Yang (Eds.), Proceedings of the Inaugural Conference of the Asia-Pacific Center for Theoretical Physics, World Scientific, Singapore, 1998.
[9] F.D.M. Haldane, Phys. Rev. B 25 (1982) 4925.
[10] C.K. Majumdar, J. Phys. C 3 (1970) 911.
[11] B.S. Shastry, B. Sutherland, Phys. Rev. Lett. 47 (1981) 964.
[12] R. Chitra, S. Pati, H.R. Krishnamurthy, D. Sen, S. Ramasesha, Phys. Rev. B 52 (1995) 6581.
[13] E. Dagotto, J. Riera, D.J. Scalapino, Phys. Rev. B 45 (1992) 5744.
[14] B.G. Levi, Phys. Today 49 (1996) 17.
[15] E. Dagotto, T.M. Rice, Science 271 (1996) 618.
[16] D.C. Cabra, M.D. Grynberg, Phys. Rev. Lett. 82 (1999) 1768.
[17] Z. Weihong, V. Kotov, J. Oitmaa, Phys. Rev. B 57 (1998) 11439.
[18] Y. Honda, T. Horiguchi, cond-mat/0106426 (2001), unpublished.
[19] D.C. Cabra, A. Honecker, P. Pujol, Phys. Rev. B 58 (1998) 6241.
[20] S.R. White, D.J. Scalapino, Phys. Rev. B 57 (1998) 3031.
[21] O.P. Sushkov, V.N. Kotov, Phys. Rev. Lett. 81 (1998) 1941.
[22] T.M. Rice, S. Gopalan, M. Sigrist, Europhys. Lett. 23 (1993) 445.
[23] M. Sigrist, T.M. Rice, F.C. Zhang, Phys. Rev. B 49 (1994) 12058.
[24] T.M. Rice, S. Haas, M. Sigrist, F.C. Zhang, Phys. Rev. B 56 (1997) 14655.

[25] S. Taniguchi, T. Nishikawa, Y. Yasui, Y. Kobayashi, M. Sato, T. Nishioka, M. Kotani, K. Sano, J. Phys. Soc. Japan 64 (1995) 2758.
[26] S. Sachdev, N. Read, Phys. Rev. Lett. 77 (1996) 4800.
[27] K. Ueda, H. Kontani, M. Sigrist, P.A. Lee, Phys. Rev. Lett. 76 (1996) 1932.
[28] S. Miyahara, K. Ueda, Phys. Rev. Lett. 82 (1999) 3701.
[29] G. Bouzerar, A.P. Kampf, G.I. Japaridze, Phys. Rev. B 58 (1998) 3117.
[30] V.N. Kotov, O.P. Sushkov, R. Eder, Phys. Rev. B 59 (1999) 6266.
[31] G.S. Uhrig, B. Normand, Phys. Rev. B 58 (1998) R14705.
[32] I. Affleck, in: A.T. Skjeltrop, D. Sherrington (Eds.), Dynamical Properties of Unconventional Magnetic Systems, NATO ASI Series E: Applied Sciences, Vol. 349, Kluwer Academic Publishers, Dordrecht, 1998, pp. 123–131.
[33] D. Augier, D. Poilblanc, E. Sørensen, I. Affleck, Phys. Rev. B 58 (1998) 9110.
[34] D. Augier, D. Poilblanc, E. Sørensen, I. Affleck, Physica B 259–261 (1998) 1015.
[35] E. Sørensen, I. Affleck, D. Augier, D. Poilblanc, Phys. Rev. B 58 (1998) 14701.
[36] D. Augier, E. Sørensen, J. Riera, D. Poilblanc, Phys. Rev. B 60 (1999) 1075.
[37] M. Laukamp, G.B. Martins, C. Gazza, A.L. Malvezzi, E. Dagotto, P.M. Hansen, A.C. Lopez, J. Riera, Phys. Rev. B 57 (1998) 10755.
[38] H. Fukuyama, N. Nagaosa, M. Saito, T. Tanimoto, J. Phys. Soc. Japan 65 (1996) 2377.
[39] Y. Motome, N. Katoh, N. Furukawa, M. Imada, J. Phys. Soc. Japan 65 (1996) 1949.
[40] Y. Iino, M. Imada, J. Phys. Soc. Japan 65 (1996) 3728.
[41] N. Nagaosa, A. Furusaki, M. Sigrist, H. Fukuyama, J. Phys. Soc. Japan 65 (1996) 3724.
[42] G.B. Martins, E. Dagotto, J.A. Riera, Phys. Rev. B 54 (1996) 16032.
[43] N. Fujiwara, H. Yasuoka, Y. Fujishiro, M. Azuma, M. Takano, Phys. Rev. Lett. 80 (1998) 604.
[44] H. Fukuyama, H. Tanitomoto, M. Saito, J. Phys. Soc. Japan 65 (1996) 1182.
[45] H. Kohno, H. Fukuyama, M. Sigrist, J. Phys. Soc. Japan 68 (1999) 1500.
[46] H. Fukuyama, J. Phys. Chem. Solids 60 (1999) 1003.
[47] H. Fukuyama, H. Kohno, B. Normand, T. Tanamoto, J. Low Temp. Phys. 99 (1995) 429.
[48] V.J. Emery, S.A. Kivelson, O. Zachar, Phys. Rev. B 56 (1997) 6120.
[49] D.H. Kim, Ph.D. Thesis, Massachusetts Institute of Technology, 1998.
[50] J.M. Tranquada, J.D. Axe, N. Ichikawa, Y. Nakamura, S. Uchida, B. Nachumi, Phys. Rev. B 54 (1996) 7489.
[51] P. Wochner, J.M. Tranquada, D.J. Buttrey, V. Sachnan, Phys. Rev. B 57 (1998) 1066.
[52] J.M. Tranquada, N. Ichikawa, S. Uchida, Phys. Rev. B 59 (1999) 14712.
[53] M. Takigawa, N. Motoyama, H. Eisaki, S. Uchida, Phys. Rev. B 57 (1998) 1124.
[54] U. Ammerahl, G. Dhalenne, A. Revcolevschi, J. Berthon, H. Mouddon, J. Crystal Growth 193 (1998) 55.
[55] M. Imada, Y. Iino, J. Phys. Soc. Japan 66 (1997) 568.
[56] G.B. Martins, M. Laukamp, J. Riera, E. Dagotto, Phys. Rev. Lett. 78 (1997) 3563.
[57] B. Grenier, J.-P. Renard, P. Veillet, C. Paulsen, R. Calemczuk, G. Dhalenne, A. Revcolevschi, Phys. Rev. B 57 (1998) 3444.
[58] M. Mostovoy, D. Khomskii, J. Knoester, Phys. Rev. B 58 (1998) 8190.
[59] Y. Oka, T. Yao, N. Yamamoto, M. Ueda, S. Maegawa, J. Solid State Chem. 149 (2000) 414.
[60] P. Lemmens, M. Fischer, M. Grove, P.H.M.v. Loosdrecht, G. Els, E. Sherman, C. Pinettes, G. Güntherodt, in: B. Kramer (Ed.), Advances in Solid State Physics 39, Vieweg Verlag, Braunschweig, 1999, pp. 281–290.
[61] D. Khomskii, W. Geertsma, M. Mostovoy, Czech. J. Phys. 46 (1996) 3239.
[62] W. Geertsma, D. Khomskii, Phys. Rev. B 54 (1996) 3011.
[63] M. Johnsson, K.W. Törnroos, F. Mila, P. Millet, Chem. Mater. 12 (2000) 2853.
[64] P. Lemmens, K.-Y. Choi, E.E. Kaul, C. Geibel, K. Becker, W. Brenig, R. Valentí, C. Gros, M. Johnsson, P. Millet, F. Mila, Phys. Rev. Lett. 87 (2001) 227201.
[65] M. Johnsson, K.W. Törnroos, P. Lemmens, P. Millet, Chem. Mater., 2002, submitted.
[66] S. van Smaalen, Z. Kristallogr. 214 (1999) 786.
[67] P.Y. Zavalij, M.S. Wittingham, Acta Cryst. B 55 (1999) 627.
[68] V. Kiryukhin, B. Keimer, D.E. Moncton, Phys. Rev. Lett. 74 (1995) 1669.
[69] V. Kiryukhin, B. Keimer, J.P. Hill, A. Vigliante, Phys. Rev. Lett. 76 (1996) 4608.

[70] T. Lorenz, B. Büchner, P.H.M. van Loosdrecht, F. Schönfeld, G. Chouteau, A. Revcolevschi, G. Dhalenne, Phys. Rev. Lett. 81 (1998) 148.
[71] F.D.M. Haldane, Phys. Lett. 93A (1983) 464.
[72] I.K. Affleck, Nucl. Phys. B 257 (1985) 397.
[73] Z. Tun, W.J.L. Buyers, R.L. Armstrong, K. Hirakawa, B. Briat, Phys. Rev. B 42 (1990) 4677.
[74] P.E. Sulewski, S.-W. Cheong, Phys. Rev. B 51 (1995) 3021.
[75] N. Ogita, Y. Tsunezumi, T. Yokoo, J. Akimitsu, M. Udagawa, J. Phys. Soc. Japan 66 (1997) 873.
[76] T. Yokoo, S. Raymond, A. Zheludev, S. Maslov, E. Ressouche, I. Zaliznyak, R. Erwin, M. Nakamura, J. Akimitsu, Phys. Rev. B 58 (1998) 14424.
[77] K.P. Schmidt, C. Knetter, G.S. Uhrig, Europhys. Lett. 56 (2001) 877.
[78] C. Jurecka, V. Gruetzun, A. Friedrich, W. Brenig, cond-mat/0104465 (2001).
[79] M. Johnsson, P. Lemmens, unpublished results.
[80] R. Valentí, T. Saha-Dasgupta, cond-mat/0110311 (2002).
[81] K. Hanke, V. Kupcik, O. Lindqvist, Acta Cryst. B 29 (1973) 963.
[82] B. Bleaney, K.D. Bowers, Proc. R. Soc. A 214 (1952) 451.
[83] M. Isobe, Y. Ueda, J. Phys. Soc. Japan 65 (1996) 3142.
[84] Y. Sasago, M. Hase, K. Uchinokura, M. Tokunaga, N. Miura, Phys. Rev. B 52 (1995) 3533.
[85] A. Zheludev, G. Shirane, Y. Sasago, M. Hase, K. Uchinokura, Phys. Rev. B 53 (1996) 11 642.
[86] R. Valentí, T. Saha-Dasgupta, C. Gros, cond-mat/0202310 (2002).
[87] J.B. Goodenough, Phys. Rev. 100 (1955) 564.
[88] J. Kanamori, J. Phys. Chem. Solids 10 (1959) 87.
[89] P.W. Anderson, Solid State Phys. 14 (1963) 99.
[90] P. Lemmens, K.-Y. Choi, G. Güntherodt, R. Valentí, C. Gros, W. Brenig, M. Johnsson, P. Millet, F. Mila, Proc. LT23, Hiroshima, Japan, to be published in Physica B.
[91] P. Lemmens, K.-Y. Choi, A. Ionescu, J. Pommer, G. Güntherodt, R. Valentí, C. Gros, W. Brenig, M. Johnsson, P. Millet, F. Mila, J. Phys. Chem. Solids 63 (2002) 1115.
[92] F. Mila, Eur. J. Phys. 21 (2000) 499.
[93] M. Mambrini, F. Mila, Eur. Phys. J. B 17 (2000) 651.
[94] C. Gros, P. Lemmens, M. Vojta, R. Valentí, K.-Y. Choi, H. Kageyama, Z. Hiroi, N.V. Mushnikov, T. Goto, M. Johnson, P. Millet, to be published (2002).
[95] W. Brenig, K.W. Becker, Phys. Rev. B 64 (2001) 214413.
[96] W. Brenig, K.W. Becker, P. Lemmens, Physica B, 2002, in print.
[97] V.N. Muthukumar, C. Gros, W. Wenzel, R. Valentí, P. Lemmens, B. Eisener, G. Güntherodt, M. Weiden, C. Geibel, F. Steglich, Phys. Rev. B 54 (1996) R9635.
[98] R.R.P. Singh, D.A. Huse, Phys. Rev. Lett. 68 (1992) 1766.
[99] H. Iwase, M. Isobe, Y. Ueda, H. Yasuoka, J. Phys. Soc. Japan 65 (1996) 2397.
[100] O.A. Starykh, M.E. Zhitomirsky, D.I. Khomskii, R.R.P. Singh, K. Ueda, Phys. Rev. Lett. 77 (1996) 2558.
[101] L.O. Manuel, M.I. Micheletti, A.E. Trumper, H.A. Ceccatto, Phys. Rev. B 58 (1998) 8490.
[102] T. Ohama, H. Yasuoka, M. Isobe, Y. Ueda, J. Phys. Soc. Japan 66 (1997) 23.
[103] K. Kodama, H. Harashina, H. Sasaki, Y. Kobayashi, M. Kasai, S. Taniguchi, Y. Yasui, M. Sato, K. Kakurai, T. Mori, M. Nishi, J. Phys. Soc. Japan 66 (1997) 793.
[104] W.E. Pickett, Phys. Rev. Lett. 79 (1997) 1746.
[105] C.S. Hellberg, W.E. Pickett, L.L. Boyer, H.T. Stokes, M.J. Mehl, J. Phys. Soc. Japan 68 (1999) 3489.
[106] M. Mambrini, F. Mila, Physica B 259–261 (1999) 967.
[107] H. Kageyama, K. Yoshimura, R. Stern, N.V. Mushnikov, K. Onizuka, M. Kato, K. Kosuge, C.P. Slichter, T. Goto, Y. Ueda, Phys. Rev. Lett. 82 (1999) 3168.
[108] H. Kageyama, H. Suzuki, M. Nohara, K. Onizuka, H. Takagi, Y. Ueda, Physica B 281 (2000) 667.
[109] K.-Y. Choi, P. Lemmens, G. Güntherodt, H. Kageyama, Y. Ueda, 2002, unpublished.
[110] R.W. Smith, D.A. Keszler, J. Solid State Chem. 93 (1991) 430.
[111] H. Kageyama, K. Onizuka, Y. Ueda, N.V. Mushnikov, T. Goto, K. Yoshimura, K. Kosuge, J. Phys. Soc. Japan 67 (1998) 4304.
[112] H. Kageyama, K. Onizuka, T. Yamauchi, Y. Ueda, J. Cryst. Growth 206 (1999) 65.

[113] H. Kageyama, J. Phys. Soc. Japan 69 (2000) 65.

[114] H. Kageyama, M. Nishi, N. Aso, K. Onizuka, T. Yoshihama, K. Nukui, K. Kodama, K. Kakurai, Y. Ueda, Phys. Rev. Lett. 84 (2000) 5876.

[115] Z. Weihong, C.J. Hamer, J. Oitmaa, Phys. Rev. B 60 (1999) 6608.

[116] H. Kageyama, N.V. Mushnikov, T. Goto, Y. Ueda, 2002, unpublished.

[117] E. Müller-Hartmann, R.R.P. Singh, C. Knetter, G.S. Uhrig, Phys. Rev. Lett. 84 (2000) 1808.

[118] C. Knetter, A. Bühler, E. Müller-Hartmann, G.S. Uhrig, Phys. Rev. Lett. 85 (2000) 3958.

[119] K. Onizuka, H. Kageyama, Y. Narumi, K. Kindo, Y. Ueda, T. Goto, J. Phys. Soc. Japan 69 (2000) 1016.

[120] T. Momoi, K. Totsuka, Phys. Rev. B 62 (2000) 15067.

[121] H. Nojiri, H. Kageyama, K. Onizuka, Y. Ueda, M. Motokawa, J. Phys. Soc. Japan 68 (1999) 2906.

[122] T. Room, U. Nagel, E. Lippmaa, H. Kageyama, K. Onizuka, Y. Ueda, Phys. Rev. B 61 (2000) 14342.

[123] N. Aso, M. Nishi, H. Kageyama, K. Kakurai, Y. Ueda, Proc. LT23, Hiroshima, Japan, to be published in Physica B.

[124] P. Lemmens, M. Grove, M. Fischer, G. Güntherodt, V.N. Kotov, H. Kageyama, K. Onizuka, Y. Ueda, Phys. Rev. Lett. 85 (2000) 2605.

[125] K. Sparta, G.J. Redhammer, P. Roussel, G. Heger, G. Roth, P. Lemmens, A. Ionescu, M. Grove, G. Güntherodt, F. Hüning, H. Lueken, H. Kageyama, K. Onizuka, Y. Ueda, Eur. Phys. J. B 19 (2001) 507.

[126] S. Miyahara, K. Ueda, J. Phys. Soc. Japan 69 (Suppl. B) (2000) 72.

[127] T. Saito, et al., J. Solid State Chem. 153 (2000) 124.

[128] C. Gross, W. Assmus, High Pressure Research, 2002, in print.

[129] G.S. Uhrig, B. Normand, Phys. Rev. B 63 (2001) 134418.

[130] T. Timusk, B. Statt, Rep. Prog. Phys. 62 (1999) 61.

[131] G. Blumberg, M. Kang, M.V. Klein, K. Kadowaki, C. Kendziora, Science 278 (1997) 1427.

[132] R. Nemetschek, M. Opel, C. Hoffmann, P.F. Müller, R. Hackl, H. Berger, L. Forro, A. Erb, E. Walker, Phys. Rev. Lett. 78 (1997) 4837.

[133] B. Batlogg, V.J. Emery, Nature 382 (1996) 20.

[134] T. Auler, M. Horvatiè, J.A. Gillet, C. Berthier, Y. Berthier, P. Ségransan, J.Y. Henry, Phys. Rev. B 56 (1997) 11294.

[135] F.C. Zhang, T.M. Rice, Phys. Rev. B 37 (1988) 3759.

[136] N. Nagaosa, P.A. Lee, Phys. Rev. B 45 (1992) 966.

[137] E. Dagotto, Rev. Mod. Phys. 66 (1994) 763.

[138] W. Brenig, Phys. Rep. 251 (1995) 154.

[139] A.V. Chubukov, D. Pines, B. Stojkovic, J. Phys.: Condens. Matter 8 (48) (1996) 10017.

[140] D. Pines, Z. Phys. B 103 (1997) 129.

[141] P.W. Anderson, Adv. Phys. 46 (1997) 3.

[142] M.D. Lumsden, B.C. Sales, D. Mandrus, S.E. Nagler, J. Thompson, Phys. Rev. Lett. 86 (2001) 159.

[143] K.Y. Choi, P. Lemmens, G. Güntherodt, unpublished results.

[144] P.A. Fleury, H.J. Guggenheim, Phys. Rev. Lett. 24 (1970) 1346.

[145] M.D. Lumsden, personal communication (2002).

[146] A. Joshi, M. Ma, F. Mila, D.N. Shi, F. Zhang, Phys. Rev. B 60 (2002) 6584.

[147] F.C. Zhang, S. Nagler, Personal communication, 2002.

[148] J.v.d. Brink, Phys. Rev. Lett. 87 (2001) 217202.

[149] E.M. McCarron, M.A. Subramanian, J.C. Calabrese, R.L. Harlow, Mat. Res. Bull. 23 (1988) 1355.

[150] M. Uehara, T. Nagata, J. Akimitsu, H. Takahashi, N. Môri, K. Kinoshita, J. Phys. Soc. Japan 65 (1996) 2764.

[151] E. Dagotto, Rep. Prog. Phys. 62 (1999) 1525.

[152] Z. Hiroi, M. Azuma, M. Takano, Y. Bando, J. Solid State Chem. 95 (1991) 230.

[153] T. Ami, M.K. Crawford, R.L. Harlow, Z.R. Wang, D.C. Johnson, Q. Huang, R.W. Erwin, Phys. Rev. B 51 (1995) 5994.

[154] K. Magishi, S. Matsumoto, Y. Kitaoka, K. Ishida, K. Asayama, M. Ueda, T. Nagata, J. Akimitsu, Phys. Rev. B 57 (1998) 11533.

[155] C. Kim, A.Y. Matsuura, Z.-X. Shen, N. Motoyama, H. Eisaki, S. Uchida, S. Maekawa, Phys. Rev. Lett. 77 (1996) 4054.

[156] H. Fujisawa, Y. Yokoya, T. Takahashi, S. Miyasake, M. Kibune, H. Takagi, Phys. Rev. B 59 (1999) 7358.

[157] T. Osagawara, M. Ashida, N. Motoyama, H. Eisaki, S. Uchida, Y. Tokura, H. Gosh, A. Shukla, S. Mazumada, M. Kuwata-Gonokami, Phys. Rev. Lett. 85 (2000) 2204.

[158] E. Dagotto, Science 293 (2001) 2410.

[159] J.H. Schön, M. Dorget, F.C. Beuran, X.Z. Xu, E. Arushanov, C.D. Cavellin, M. Laguës, Nature 414 (2001) 434.

[160] J.H. Schön, M. Dorget, F.C. Beuran, X.Z. Xu, E. Arushanov, M. Laguës, C.D. Cavellin, Science 293 (2001) 2430.

[161] M. Azuma, Z. Hiroi, M. Takano, K. Ishida, Y. Kitaoka, Phys. Rev. Lett. 73 (1994) 3463.

[162] K. Ishida, Y. Kitaoka, Y. Tokunaga, S. Matsumoto, M. Azuma, Z. Hiroi, M. Takano, Phys. Rev. B 53 (1996) 2827.

[163] M. Azuma, M. Takano, R.S. Eccleston, J. Phys. Soc. Japan 67 (1998) 740.

[164] S. Ohsugi, Y. Kitaoka, Y. Tokunaga, K. Ishida, M. Azuma, Y. Fujishiro, M. Takano, Physica B 259–261 (1999) 1040.

[165] M. Azuma, Y. Fujishiro, M. Takano, M. Nohara, H. Takagi, Phys. Rev. B 55 (1997) R8658.

[166] E.Y. Sherman, Private communication, 2002.

[167] D.E. Cox, T. Iglesias, K. Hirota, G. Shirane, M. Matsuda, N. Motoyama, H. Esaki, S. Uchida, Phys. Rev. B 57 (1998) 10750.

[168] M. Kato, K. Shiota, Y. Koike, Physica C 258 (1996) 284.

[169] T. Nagata, M. Uehara, J. Goto, J. Akimitsu, N. Motoyama, H. Eisaki, S. Uchida, H. Takahashi, T. Nakanishi, N. Môri, Phys. Rev. Lett. 81 (1998) 1090.

[170] S.A. Carter, B. Batlogg, R.J. Cava, J.J. Krajewski, W.F. Peck Jr., T.M. Rice, Phys. Rev. Lett. 77 (1996) 1378.

[171] S. Katano, T. Nagata, J. Akimitsu, M. Nishi, K. Kakurai, Phys. Rev. Lett. 82 (1999) 636.

[172] R.S. Eccleston, M. Uehara, J. Akimitsu, H. Eisaki, N. Motoyama, S. Uchida, Phys. Rev. Lett. 81 (1998) 1702.

[173] T. Osafune, N. Motoyama, H. Eisaki, S. Uchida, Phys. Rev. Lett. 78 (1997) 1980.

[174] T. Osafune, N. Motoyama, H. Eisaki, S. Uchida, S. Tajima, Phys. Rev. Lett. 82 (1999) 1313.

[175] M. Grove, Ph.D. Thesis, 2. Physikalisches Institut, RWTH Aachen, 2000.

[176] N. Nücker, M. Merz, C.A. Kuntscher, S. Gerhold, S. Schuppler, R. Neudert, M.S. Golden, J. Fink, S. Stadler, V. Chakarian, J. Freeland, Y.U. Idzerda, M. Uehara, T. Nagata, J. Goto, J. Akimitsu, N. Motoyama, H. Eisaki, S. Uchida, U. Ammerahl, A. Revcolevschi, Phys. Rev. B 62 (2000) 14384.

[177] H. Kitano, R. Inoue, T. Hanaguri, A. Maeda, N. Motoyama, M. Takaba, H. Eisaki, S. Uchida, Physica B 284 (2000) 1936.

[178] M.V. Abrashev, C. Thomsen, M. Surtchev, Physica C 280 (1997) 297.

[179] S. Sugai, M. Suzuki, Phys. Stat. Sol. B 215 (1999) 653.

[180] S. Sugai, Raman spectroscopy of magnetic compounds with strong electron-correlation, in: S. Sugano, N. Kojima (Eds.), Magneto-Optics, Vol. 128, Springer, New York, 2000, pp. 75–106 (Chapter 3).

[181] P.J. Freitas, R.R.P. Singh, Phys. Rev. B 62 (2000) 14113.

[182] A. Gozar, Phys. Rev. B 65 (2002) 176403.

[183] A. Gozar, B. Blumberg, B.S. Dennis, B.S. Shastry, N. Motoyama, H. Eisaki, S. Uchida, Phys. Rev. Lett. 87 (2001) 197202.

[184] P. Lemmens, M. Grove, unpublished.

[185] T.F.A. Müller, V. Anisimov, T.M. Rice, I. Dasgupta, T. Saha-Dasgupta, Phys. Rev. B 57 (1998) 12655.

[186] M. Matsuda, T. Yoshihama, K. Kakurai, G. Shirane, Phys. Rev. B 59 (1999) 1060.

[187] Z.V. Popović, M.J. Konstantinović, V.A. Ivanov, O.P. Khuong, R. Gajić, A. Vietkin, V.V. Moshchalkov, Phys. Rev. B 63 (2001) 165105.

[188] E.Ya. Sherman, M. Fischer, P. Lemmens, P.H.M. van Loosdrecht, G. Güntherodt, Europhys. Lett. 48 (1999) 648.

[189] M. Fischer, P. Lemmens, G. Els, G. Güntherodt, E.Ya. Sherman, E. Morré, C. Geibel, F. Steglich, Phys. Rev. B 60 (1999) 7284.

[190] S.-H. Lee, S.-W. Chong, Phys. Rev. Lett. 79 (1997) 2514.

[191] H. Mayaffre, P. Auban-Senzier, M. Nardone, D. Jerome, D. Poilblanc, C. Bourbonnais, U. Ammerahl, G. Dhalenne, A. Revcolevschi, Science 279 (5349) (1998) 345.

[192] S. Katano, T. Nagata, H. Fujino, J. Akimitsu, M. Nishi, K. Kakurai, Physica B 259–261 (1999) 1046.

[193] M. Isobe, Y. Uchida, E. Takayama-Muromachi, Phys. Rev. B 59 (1999) 8703.

[194] J. Akimitsu, Physica B 259–261 (1999) 1030.

[195] J. Akimitsu, K. Ohshi, T. Yokoo, K. Kakuta, H. Fujino, T. Nagata, R. Kadono, M. Nishi, K. Kakurai, S. Katano, Physica B 289 (2000) 157.

[196] D. Braithwaite, T. Nagata, I. Sheikin, H. Fujino, J. Akimistu, J. Flouquet, Solid State Commun. 114 (2000) 533.

[197] T. Yamauchi, H. Yamada, N. Takeshita, Y. Ueda, N. Mori, J. Phys. Chem. Solids 63 (2002) 951.

[198] W. Bao, C. Broholm, G. Aeppli, S.A. Carter, P. Dai, T.F. Rosenbaum, J.M. Honig, P. Metcalf, S.F. Trevino, Phys. Rev. B 58 (1998) 12727.

[199] M. Isobe, Ph.D. Thesis, Institute for Solid State Physics, The University of Tokyo, 1998.

[200] M. Isobe, Y. Ueda, J. Magn. Magn. Mat. 177–181 (1998) 671.

[201] M. Isobe, Y. Ueda, K. Takizawa, T. Goto, J. Phys. Soc. Japan 67 (1998) 755.

[202] P. Millet, C. Satto, J. Bouvoisin, B. Normand, K. Penc, M. Albrecht, F. Mila, Phys. Rev. B 57 (1998) 5005.

[203] R. Valentí, T. Saha-Dasgupta, J.V. Alvarez, K. Požgajčić, C. Gros, Phys. Rev. Lett. 86 (2001) 5381.

[204] H. Fujiwara, H. Yasuoka, M. Isobe, Y. Ueda, S. Maegawa, Phys. Rev. B 55 (1997) R11945.

[205] J. Galy, A. Casalot, M. Pouchard, P. Hagenmuller, C.R. Acad. Sci. Paris C 262 (1966) 1055.

[206] P.A. Carpy, J. Galy, Acta Cryst. B 31 (1975) 1481.

[207] M. Isobe, Y. Ueda, J. Phys. Soc. Japan 65 (1996) 1178.

[208] M. Weiden, R. Hauptmann, C. Geibel, F. Steglich, M. Fischer, P. Lemmens, G. Güntherodt, Z. Phys. B 103 (1997) 1.

[209] H.G.v. Schnering, Y. Grin, M. Kaupp, M. Somer, R.K. Kremer, O. Jepsen, T. Chatterji, M. Weiden, Z. Kristallogr.-New Cryst. Struct. 213 (1998) 246.

[210] H. Yamada, Y. Ueda, Physica B 284 (2000) 1651.

[211] M. Itoh, N. Akimoto, H. Yamada, M. Isobe, Y. Ueda, J. Phys. Soc. Japan 69 (2000) 155.

[212] Y. Ueda, J. Phys. Soc. Japan 69 (2000) 149.

[213] M. Itoh, N. Akimoto, M. Tsuchiya, H. Yamada, M. Isobe, Y. Ueda, Physica B 281 (2000) 606.

[214] M. Grove, P. Lemmens, G. Els, G. Güntherodt, B.C. Sales, F. Büllesfeld, W. Assmus, Phys. Rev. B 61 (2000) 6126.

[215] A.W. Garrett, S.E. Nagler, T. Barnes, B.C. Sales, Phys. Rev. B 55 (1997) 3631.

[216] T. Barnes, J. Riera, Phys. Rev. B 50 (1994) 6817.

[217] A.W. Garrett, S.E. Nagler, D.A. Tennant, B.C. Sales, T. Barnes, Phys. Rev. Lett. 79 (1997) 745.

[218] D.A. Tennant, S.E. Nagler, T. Barnes, A.W. Garrett, J. Riera, B.C. Sales, Physica B 241 (1997) 501.

[219] A.W. Garrett, S.E. Nagler, D.A. Tennant, T. Barnes, C.C. Torardi, Physica B 241 (1997) 552.

[220] J. Kikuchi, K. Motoya, T. Yamauchi, Y. Ueda, Phys. Rev. B 60 (1999) 6731.

[221] A.V. Prokovief, B. Büllesfeld, W. Assmus, H. Schenk, D. Wichert, U. Löw, B. Lüthi, Eur. Phys. J. B 5 (1998) 313.

[222] T. Barnes, J. Riera, D.A. Tennant, Phys. Rev. B 59 (1999) 11384.

[223] A. Weiße, G. Bouzerar, H. Fehske, Eur. Phys. J. B 7 (1999) 5.

[224] U. Kuhlmann, C. Thomsen, A.V. Prokoviev, B. Büllesfeld, E. Uhrig, W. Assmus, Phys. Rev. B 62 (2000).

[225] A. Klümper, Eur. Phys. J. B 5 (1998) 687.

[226] U. Kuhlmann, C. Thomsen, A.V. Prokofiev, F. Büllesfeld, E. Uhrig, M. Anton, C. Gross, W. Assmus, Phys. Rev. B 66 (2002) 064420.

[227] I. Yamada, H. Onda, Phys. Rev. B 49 (1994) 1048.

[228] D.A. Tennant, T.G. Perring, R.A. Cowley, S.E. Nagler, Phys. Rev. Lett. 70 (1993) 4003.

[229] D.A. Tennant, R.A. Cowley, S.E. Nagler, A.M. Tsvelik, Phys. Rev. B 52 (1995) 13368.

[230] G. Müller, H. Thomas, H. Beck, J.C. Bonner, Phys. Rev. B 24 (1981) 1429.

[231] B. Lake, D.A. Tennant, S.E. Nagler, Phys. Rev. B 85 (2000) 832.

[232] A. Oosawa, T. Takamasu, K. Tatani, H. Abe, N. Tsujii, O. Suzuki, H. Tanaka, G. Kido, K. Kindo, Phys. Rev. B 66 (2002) 104405.

[233] K.-Y. Choi, P. Lemmens, A. Ionescu, G. Güntherodt, A. Oosawa, H. Tanaka, 2002, unpublished.

[234] H. Tanaka, K. Takatsu, W. Shiramura, T. Ono, J. Phys. Soc. Japan 65 (1996) 1945.

[235] T. Nakamura, K. Okamoto, Phys. Rev. B 58 (1998) 2411.

[236] D.C. Cabra, A. Honecker, P. Pujol, Eur. Phys. J. B 13 (2000) 55.

[237] T. Kato, K. Takatsu, H. Tanaka, W. Shiramura, M. Mori, K. Nakajima, K. Kakurai, J. Phys. Soc. Japan 67 (1998) 752.

[238] N. Cavadini, W. Henggeler, A. Furrer, H.-U. Güdel, K. Krämer, H. Mutka, Eur. Phys. J. B 7 (1999) 519.

[239] A. Oosawa, T. Kato, H. Tanaka, K. Nakajima, K. Nishi, K. Kakurai, J. Phys. Soc. Japan, Suppl. A 70 (2000) 166.
[240] A. Oosawa, T. Kato, H. Tanaka, K. Kakurai, M. Müller, H.-J. Mikeska, Phys. Rev. B 65 (2002) 094426.
[241] N. Suzuki, Y. Fujimoto, S. Kokado, Physica B 284 (2000) 1567.
[242] N. Cavadini, W. Henggeler, A. Furrer, H.-U. Güdel, K. Krämer, H. Mutka, Physica 276 (2000) 540.
[243] M. Troyer, H. Tsunetsugu, D. Würtz, Phys. Rev. B 50 (1994) 13513.
[244] N. Cavadini, W. Henggeler, A. Furrer, H.U. Gudel, K. Kramer, H. Mutka, Eur. Phys. J. 7 (2000) 519.
[245] W. Higemoto, H. Tanaka, I. Watanabe, S. Ohira, A. Fukaya, K. Nagamine, Physica B 289 (2000) 172.
[246] D. Andreica, N. Cavadini, H.U. Güdel, F.N. Gygax, K. Krämer, M. Pinkpank, A. Schenck, Physica B 289 (2000) 176.
[247] K. Takatsu, W. Shiramura, H. Tanaka, T. Kambe, H. Nojiri, M. Motokawa, J. Magn. Mag. Mat. 177–181 (1998) 697.
[248] A. Oosawa, M. Ishii, H. Tanaka, J. Phys.: Condens. Matter 11 (1999) 265.
[249] T. Nikuni, M. Oshikawa, A. Oosawa, H. Tanaka, Phys. Rev. Lett. 84 (2000) 5868.
[250] O. Vyaselev, M. Takigawa, A. Oosawa, H. Tanaka, in: Y. Ajiro, J.-P. Boucher (Eds.), Proc. Japanese–French Symposium on Quantum Properties of Low-Dimensional Antiferromagnets, Kyushu University Press, Japan, 2002, pp. 55–61.
[251] E.Ya. Sherman, P. Lemmens, B. Busse, unpublished results.
[252] W. Shiramura, K. Takatsu, B. Kurniawan, H. Tanaka, H. Uekusa, Y. Ohashi, K. Takizawa, H. Mitamura, T. Goto, J. Phys. Soc. Japan 67 (1998) 1548.
[253] B. Kurniawan, M.I.T.K.H. Tanaka, K. Takizawa, T. Goto, J. Phys.: Condens. Matter 11 (1999) 9073.
[254] M. Oshikawa, I. Affleck, Phys. Rev. Lett. 79 (1997) 2883.
[255] I. Affleck, M. Oshikawa, Phys. Rev. B 60 (1999) 1038.
[256] M. Oshikawa, M. Yamanaka, I. Affleck, Phys. Rev. Lett. 78 (1997) 1984.
[257] D.C. Cabra, A. Honecker, P. Pujol, Phys. Rev. Lett. 79 (1997) 5126.
[258] K. Totsuka, Phys. Rev. B 57 (1998) 3454.
[259] K. Tandon, S. Lal, S.K. Pati, S. Ramasesha, D. Sen, Phys. Rev. B 59 (1999) 396.
[260] A.M. Heyns, C.J.H. Schutte, J. Mol. Struct. 8 (1971) 339.
[261] F. Mila, A. Honecker, Private communication, 2001.
[262] W.J.L. Buyers, R.M. Morra, R.L. Armstrong, M.J. Hogan, P. Gerlach, K. Hirakawa, Phys. Rev. Lett. 56 (1986) 371.
[263] R.M. Morra, W.J.L. Buyers, R. Armstrong, K. Hirakawa, Phys. Rev. B 38 (1988) 543.
[264] R. Helfrich, M. Kïoppen, M. Lang, F. Steglich, A. Ochiai, J. Magn. Mag. Mat. 177–181 (1998) 309.
[265] A. Ochiai, T. Suzuki, T. Kasuya, J. Phys. Soc. Japan 59 (1990) 4129.
[266] M. Kohgi, K. Iwasa, J.-M. Mignot, A. Ochiai, T. Suzuki, Phys. Rev. B 56 (1997) 11388.
[267] M. Koghi, K. Iwasa, J.-M. Mignot, N. Pyka, A. Ochiai, H. Aoki, T. Suzuki, Physica B 259–261 (1999) 269.
[268] K. Iwasa, M. Koghi, A. Gukasov, J.-M. Mignot, A. Ochiai, H. Aoki, T. Suzuki, Physica B 281–282 (2000) 460.
[269] P. Fulde, B. Schmidt, P. Thalmeier, Europhys. Lett. 31 (1995) 323.
[270] M. Kohgi, K. Iwasa, J.-M. Mignot, B. Faak, P. Gegenwart, M. Lang, A. Ochiai, H. Aoki, T. Suzuki, Phys. Rev. Lett. 86 (2001) 2439.
[271] B. Schmidt, P. Thalmeier, P. Fulde, Europhys. Lett. 35 (1996) 109.
[272] G. Uimin, Y. Kudasov, P. Fulde, A. Ovchinnikov, Eur. Phys. J. B 16 (2000) 241.
[273] M. Oshikawa, K. Ueda, H. Aoki, A. Ochiai, M. Kohgi, J. Phys. Soc. Japan 68 (1999) 3181.
[274] H. Aoki, A. Ochiai, M. Oshikawa, K. Ueda, Physica B 281–282 (2000) 465.
[275] H. Shiba, K. Ueda, O. Sakai, J. Phys. Soc. Japan 69 (2000) 1493.
[276] O.V. Misochko, S. Tajima, C. Urano, H. Eisaki, S. Uchida, Phys. Rev. B 53 (1996) 14733.
[277] R.E. Peierls, Quantum Theory of Solids, Oxford University Press, London, 1955.
[278] S. Huizinga, J. Kommandeur, G.A. Sawatzky, B.T. Thole, K. Kopinga, W.J.M. deJonge, J. Roos, Phys. Rev. B 19 (1979) 4723.
[279] J.W. Bray, H.R. Hart, L.V. Interrante, I.S. Jacobs, J.S. Kasper, G.D. Watkins, S.H. Wee, J.C. Bonner, Phys. Rev. Lett. 35 (1975) 744.
[280] I.S. Jacobs, J.W. Bray, H.R. Hart, L.V. Interrante, J.S. Kasper, G.D. Watkins, D.E. Prober, J.C. Bonner, Phys. Rev. B 14 (1976) 3036.
[281] F. Creuzet, C. Bourbonnais, L.G. Caron, D. Jerome, K. Bechgaard, Synth. Met. 19 (1987) 289.

[282] J.W. Bray, L.V. Iterrante, I.S. Jacobs, J.C. Bonner, in: J.S. Miller (Ed.), Extended Linear Chain Compounds, Plenum Press, New York, 1983, pp. 353–415 (Chapter 7).

[283] M. Hase, I. Terasaki, K. Uchinokura, Phys. Rev. Lett. 70 (1993) 3651.

[284] J.P. Boucher, L.P. Regnault, J. Phys. I (Paris) 6 (1996) 1939.

[285] A.P. Ramirez, Annu. Rev. Mat. Sci. 24 (1994) 453.

[286] A.P. Ramirez, Czech. J. Phys. 46 (1996) 3247.

[287] H. Smolinski, C. Gros, W. Weber, U. Peuchert, G. Roth, M. Weiden, C. Geibel, Phys. Rev. Lett. 80 (1998) 5164.

[288] H. Völlenkle, A. Wittman, N. Nowotny, Monatsh. Chem. 98 (1967) 1352.

[289] S.D. Dević, M.J. Konstantinović, Z.V. Popović, G. Dhalenne, A. Revcolevschi, J. Phys.: Condens. Matter 6 (1994) L745.

[290] Z. Popović, S.D. Dević, V.N. Popov, G. Dhalenne, A. Revcolevschi, Phys. Rev. B 52 (1995) 4185.

[291] M. Braden, G. Wilkenorf, J. Lorenzana, M. Aïn, G.J. McIntyre, M. Behruzi, G. Heger, G. Dhalenne, A. Revcolevschi, Phys. Rev. B 54 (1996) 1105.

[292] J.C. Bonner, M.E. Fisher, Phys. Rev. 135 (1964) A640.

[293] J. Riera, A. Dobry, Phys. Rev. B 51 (1995) 16098.

[294] G. Castilla, S. Chakravarty, V.J. Emery, Phys. Rev. Lett. 75 (1995) 1823.

[295] M. Nishi, O. Fujita, J. Akimitsu, Phys. Rev. B 50 (1994) 6508.

[296] L.P. Regnault, M. Aïn, B. Hennion, G. Dhalenne, A. Revcolevschi, Phys. Rev. B 53 (1996) 5579.

[297] B. Büchner, U. Ammerahl, T. Lorenz, W. Brenig, G. Dhalenne, A. Revcolevschi, Phys. Rev. Lett. 77 (1996) 1624.

[298] K. Fabricius, A. Klümper, U. Löw, B. Büchner, T. Lorenz, G. Dhalenne, A. Revcolevschi, Phys. Rev. B 57 (1998) 1102.

[299] G.S. Uhrig, Phys. Rev. B 57 (1998) R14004.

[300] Q.J. Harris, Q. Feng, R.J. Birgeneau, K. Hirota, K. Kakurai, J.E. Lorenzo, G. Shirane, M. Hase, K. Uchinokura, H. Kojima, I. Tanaka, Y. Shibuya, Phys. Rev. B 50 (1994) 12606.

[301] J.P. Pouget, L.P. Regnault, M. Aïn, B. Hennion, J.P. Renard, P. Veillet, G. Dhalenne, A. Revcolevschi, Phys. Rev. Lett. 72 (1994) 4037.

[302] J.E. Lorenzo, K. Hirota, G. Shirane, J.M. Tranquada, M. Hase, K. Uchinokura, H. Kojima, I. Tanaka, Y. Shibuya, Phys. Rev. B 50 (1994) 1278.

[303] G.S. Uhrig, Phys. Rev. Lett. 79 (1997) 163.

[304] G. Els, Ph.D. Thesis, 2. Physikalisches Institut der RWTH Aachen, 1999.

[305] K. Hirota, D.E. Cox, J.E. Lorenzo, G. Shirane, J.M. Tranquada, M. Hase, K. Uchinokura, H. Kojima, Y. Shibuya, I. Tanaka, Phys. Rev. Lett. 73 (1994) 736.

[306] R. Werner, C. Gros, M. Braden, Phys. Rev. B 59 (1999) 14356.

[307] M. Braden, B. Hennion, W. Reichert, G. Dhalenne, A. Revcolevschi, Phys. Rev. Lett. 80 (1998) 3634.

[308] H. Kuroe, T. Sekine, M. Hase, Y. Sasago, K. Uchinokura, H. Kojima, I. Tanaka, Y. Shibuya, Phys. Rev. B 50 (1994) 16468.

[309] P. Lemmens, B. Eisener, M. Brinkmann, L.V. Gasparov, G. Güntherodt, P.v. Dongen, M. Weiden, W. Richter, C. Geibel, F. Steglich, Physica B 223–224 (1996) 535.

[310] S. Glutsch, in: R. Helbig (Ed.), Festkörperprobleme—Advances in Solid State Physics, Vol. 37, Vieweg Verlag, Braunschweig, 1998, pp. 151–167.

[311] K. Hirota, G. Shirane, Q.J. Harris, Q. Feng, R.J. Birgeneau, M. Hase, K. Uchinokura, Phys. Rev. B 52 (1995) 15412.

[312] M. Braden, E. Ressouche, B. Büchner, R. Keßler, G. Heger, G. Dhalenne, A. Revcolevschi, Phys. Rev. B 57 (1998) 11497.

[313] N. Ogita, T. Minami, Y. Tanimoto, O. Fujita, J. Akimitsu, P. Lemmens, G. Güntherodt, M. Udagawa, J. Phys. Soc. Japan 65 (1996) 3754.

[314] M.C. Cross, D.S. Fisher, Phys. Rev. B 19 (1979) 402.

[315] A.W. Sandvik, D.K. Campbell, Phys. Rev. Lett. 83 (1999) 195.

[316] C. Gros, R. Werner, Phys. Rev. B 58 (1998) 14677.

[317] G. Wellein, H. Fehske, A.P. Kampf, Phys. Rev. Lett. 81 (1998) 3956.

[318] M. Arai, M. Fujita, M. Motokawa, J. Akimitsu, S.M. Bennington, Phys. Rev. Lett. 77 (1996) 3649.

[319] M. Aïn, J.E. Lorenzo, L.P. Regnault, G. Dhalenne, A. Revcolevschi, T. Jolicoeur, Phys. Rev. Lett. 78 (1997) 1560.

[320] M.C. Martin, G. Shirane, Y. Fujii, M. Nishi, O. Fujita, J. Akimitsu, M. Hase, K. Uchinokura, Phys. Rev. B 53 (1996) R14713.
[321] T.M. Brill, J.P. Boucher, J. Voiron, G. Dhalenne, A. Revcolevschi, J.P. Renard, Phys. Rev. Lett. 73 (1994) 1545.
[322] P.H.M. van Loosdrecht, S. Huant, G. Martinez, G. Dhalenne, A. Revcolevschi, Phys. Rev. B 54 (1996) R3730.
[323] J.E. Lorenzo, L.P. Regnault, J.P. Boucher, B. Hennion, G. Dhalenne, A. Revcolevschi, Europhys. Lett. 45 (1999) 619.
[324] I. Yamada, M. Nishi, J. Akimitsu, J. Phys.: Condens. Matter 8 (1996) 2625.
[325] M. Hidaka, M. Hatae, I. Yamada, M. Nishi, J. Akimitsu, J. Phys.: Condens. Matter 9 (1997) 809.
[326] I. Loa, S. Gronemeyer, C. Thomsen, R.K. Kremer, Solid State Commun. 99 (1996) 231.
[327] H. Nojiri, H. Ohta, S. Okubo, O. Fujita, J. Akimitsu, M. Motokawa, J. Phys. Soc. Japan (1999).
[328] P. Lemmens, M. Fischer, G. Güntheroth, C. Gros, P.G.J. van Dongen, M. Weiden, W. Richter, C. Geibel, F. Steglich, Phys. Rev. B 55 (1997) 15076.
[329] T. Lorenz, U. Ammerahl, T. Auweiler, B. Büchner, A. Revcolevschi, G. Dhalenne, Phys. Rev. B 55 (1997) 5914.
[330] M. Hase, I. Terasaki, K. Uchinokura, M. Tokunaga, N. Miura, H. Obara, Phys. Rev. B 48 (1993) 9616.
[331] J.-G. Lussier, S.M. Coad, D.F. McMorrow, D.M. Paul, J. Phys.: Condens. Matter 7 (1995) L325.
[332] N. Koide, Y. Uchiyama, T. Hayashi, T. Masuda, Y. Sasago, K. Uchinokura, K. Manabe, H. Ishimoto, cond-mat/9805095, 1999, unpublished.
[333] B. Grenier, J.-P. Renard, P. Veillet, C. Paulsen, G. Dhalenne, A. Revcolevschi, Phys. Rev. B 58 (1998) 8202.
[334] P.E. Anderson, J.Z. Liu, R.N. Shelton, Phys. Rev. B 56 (1997) 11014.
[335] T. Masuda, A. Fujioka, Y. Uchiyama, I. Tsukada, K. Uchinokura, Phys. Rev. Lett. 80 (1998) 4566.
[336] M. Hase, N. Koide, K. Manabe, Y. Sasago, K. Uchinokura, A. Sawa, Physica B 215 (1995) 164.
[337] M. Hase, K. Uchinokura, R.J. Birgeneau, K. Hirota, G. Shirane, J. Phys. Soc. Japan 65 (1996) 1392.
[338] M. Weiden, W. Richter, C. Geibel, F. Steglich, P. Lemmens, B. Eisener, M. Brinkmann, G. Güntherodt, Physica B 225 (1996) 177.
[339] M.C. Martin, M. Hase, K. Hirota, G. Shirane, Y. Sasago, N. Koide, K. Uchinokura, Phys. Rev. B 56 (1997) 3173.
[340] K.M. Kojima, Y. Fudamoto, M. Larkin, G.M. Luke, J. Merlin, B. Nachumi, Y.J. Uemura, M. Hase, Y. Sasago, K. Uchinokura, Y. Ajiro, A. Revcolevschi, J.P. Renard, Phys. Rev. Lett. 79 (1997) 503.
[341] H. Kuroe, H. Seto, J. Sasaki, T. Sekine, N. Koide, Y. Sasago, K. Uchinokura, M. Hase, M. Isobe, Y. Ueda, J. Magn. Magn. Mat. 177–181 (1998) 679.
[342] L.P. Regnault, J.P. Renard, G. Dhalenne, A. Revcolevschi, Europhys. Lett. 32 (1995) 579.
[343] J.P. Renard, K.L. Dang, P. Veillet, G. Dhalenne, A. Revcolevschi, L.P. Regnault, Europhys. Lett. 30 (1995) 475.
[344] M. Weiden, R. Hauptmann, W. Richter, C. Geibel, P. Hellmann, M. Köppen, F. Steglich, M. Fischer, P. Lemmens, G. Güntherodt, A. Krimmel, G. Nieva, Phys. Rev. B 55 (1997) 15067.
[345] M. Weiden, W. Richter, R. Hauptmann, C. Geibel, F. Steglich, Physica B 233 (1997) 153.
[346] M. Fabrizio, R. Melin, J. Souleti, Eur. Phys. J. B 10 (1999) 607.
[347] K. Manabe, H. Ishimoto, N. Koide, Y. Sasago, K. Uchinokura, Phys. Rev. B 58 (1998) R575.
[348] M. Fischer, P.H.M. van Loosdrecht, P. Lemmens, G. Güntherodt, B. Büchner, T. Lorenz, M. Breuer, J. Zeman, G. Martinez, G. Dhalenne, A. Revcolevschi, Phys. Rev. B 57 (1998) 7749.
[349] J. Villain, J. Phys. 41 (1980) 1263.
[350] J.E. Hirsch, R. Kariotis, Phys. Rev. B 32 (1985) 7320.
[351] H.-B. Schüttler, D.J. Scalapino, P.M. Grant, Phys. Rev. B 35 (1987) 3461.
[352] T. Sekine, H. Kuroe, J. Sasaki, K. Uchinokura, M. Hase, J. Magn. Mag. Mat. 177–181 (1998) 691.
[353] G. Els, G.S. Uhrig, P. Lemmens, H. Vonberg, P.H.M. van Loosdrecht, G. Güntherodt, O. Fujita, J. Akimitsu, G. Dhalenne, A. Revcolevschi, Europhys. Lett. 43 (1998) 463.
[354] T. Ohama, H. Yasuoka, M. Isobe, Y. Ueda, Phys. Rev. B 59 (1999) 3299.
[355] T. Ohama, A. Goto, T. Shimizu, E. Ninomiya, H. Sawa, M. Isobe, Y. Ueda, J. Phys. Soc. Japan 69 (2000) 2751.
[356] J. Lüdecke, A. Jobst, S. van Smaalen, E. Morré, C. Geibel, H.-G. Krane, Phys. Rev. Lett. 82 (1999) 3633.
[357] T. Ohama, M. Isobe, H. Yasuoka, Y. Ueda, J. Phys. Soc. Japan 66 (1997) 545.
[358] J. Riera, D. Poilblanc, Phys. Rev. B 59 (1999) 2667.
[359] S. Van Smaalen, P. Daniels, L. Palatinus, R.K. Kremer, Phys. Rev. B 65 (2002) 060101.
[360] C. Gros, R. Valentí, Phys. Rev. Lett. 82 (1999) 976.

[361] S.A. Golubchik, M. Isobe, A.N. Ivlev, B.N. Mavrin, M.N. Popova, A.B. Sushkov, Y. Ueda, A.N. Vasil'ev, J. Phys. Soc. Japan 66 (1997) 4042.
[362] P. Lemmens, M. Fischer, G. Güntherodt, A. Mishchenko, M. Weiden, R. Hauptmann, C. Geibel, F. Steglich, Phys. Rev. B 58 (1998) 14159.
[363] E.Ya. Sherman, C. Ambrosch-Draxl, P. Lemmens, G. Güntherodt, P.H.M. van Loosdrecht, Phys. Rev. B 63 (2001) 224305.
[364] P. Horsch, F. Mack, Eur. J. Phys. B 5 (1998) 367.
[365] Y. Fuji, H. Nakano, T. Yosihama, M. Nishi, K. Nakajima, K. Kakurai, M. Isobe, Y. Ueda, H. Sawa, J. Phys. Soc. Japan 66 (1997) 326.
[366] M. Fischer, P. Lemmens, G. Güntherodt, M. Weiden, R. Hauptmann, C. Geibel, F. Steglich, Physica B 244 (1998) 76.
[367] H. Nakao, K. Ohwada, N. Takesue, Y. Fujii, M. Isobe, Y. Ueda, H. Sawa, H. Kawada, Y. Murakami, W.I.F. David, R.M. Ibberson, Physica B 241 (1997) 534.
[368] J. Hemberger, M. Lohmann, M. Nicklas, A. Loidl, M. Klemm, G. Obermeier, S. Horn, Europhys. Lett. 42 (1998) 661.
[369] W. Schnelle, Y. Grin, R.K. Kremer, Phys. Rev. B 59 (1999) 73.
[370] M. Köppen, D. Pankert, R. Hauptmann, M. Lang, M. Weiden, C. Geibel, F. Steglich, Phys. Rev. B 57 (1998) 8466.
[371] A.N. Vasil'ev, A.I. Smirnov, M. Isobe, Y. Ueda, Phys. Rev. B 56 (1997) 5065.
[372] S. Luther, H. Nojiri, M. Motokawa, M. Isobe, Y. Ueda, J. Phys. Soc. Japan 67 (1998) 3715.
[373] T. Yosihama, M. Nishi, K. Nakajima, K. Kakurai, Y. Fujii, M. Isobe, C. Kagami, Y. Ueda, J. Phys. Soc. Japan 67 (1998) 744.
[374] T. Yosihama, M. Nishi, K. Nakajima, N. Aso, K. Kakurai, Y. Fujii, S.I.C.D. Frost, S. Bennington, M. Isobe, Y. Ueda, Physica B 281–282 (2000) 654.
[375] M.V. Mostovoy, D.I. Khomskii, Solid. State Commun. 113 (2000) 159.
[376] K. Ohwada, Y. Fujii, N. Takesue, M. Isobe, Y. Ueda, H. Nakao, Y. Wakabayashi, Y. Murakami, K. Ito, Y. Amemiya, Y. Fujihisa, K. Aoki, T. Shobu, Y. Noda, N. Ikeda, Phys. Rev. Lett. 87 (2001) 086402.
[377] P. Bak, J. von Boehm, Phys. Rev. B 21 (1980) 5297.
[378] D. Sa, C. Gros, Eur. Phys. J. B 18 (2001) 421.
[379] H. Seo, H. Fukuyama, J. Phys. Soc. Japan 67 (1998) 2602.
[380] P. Thalmeier, P. Fulde, Eur. Phys. Lett. 44 (1998) 242.
[381] A.N. Yaresko, V.N. Antonov, H. Eschrig, P. Thalmeier, P. Fulde, Phys. Rev. B 62 (2000) 15538.
[382] A. Hübsch, C. Waidacher, K.W. Becker, Phys. Rev. B 64 (2001) 241103.
[383] G.P. Zhang, T.A. Callcott, G.T. Woods, L. Lin, B. Sales, D. Mandrus, J. He, Phys. Rev. Lett., in press; cond-mat/0201497 (2002).
[384] S. Atzkern, M. Knupfer, M.S. Golden, J. Fink, A.N. Yaresko, V.N. Antonov, A. Hübsch, C. Waidacher, K.W. Becker, W. von der Linden, G. Obermeier, S. Horn, Phys. Rev. B 63 (2001) 165113.
[385] H. Seo, H. Fukuyama, J. Phys. Soc. Japan 66 (1997) 1249.
[386] K. Hiraki, K. Kanoda, Phys. Rev. Lett. 80 (1998) 4737.
[387] M.V. Mostovoy, D.I. Khomskii, J. Knoester, Phys. Rev. B 65 (2002) 064412.
[388] A. Hübsch, C. Waidacher, K.W. Becker, W.V. der Linden, Phys. Rev. B 64 (2001) 075107.
[389] Q.J. Harris, Q. Feng, R.J. Birgeneau, K. Hirota, G. Shirane, M. Hase, K. Uchinokura, Phys. Rev. B 52 (1995) 15420.
[390] C.H. Chen, S.-W. Cheong, Phys. Rev. B 51 (1995) 6777.
[391] P. Fertey, M. Poirier, M. Castonguay, J. Jegoudez, A. Revcolevschi, Phys. Rev. B 57 (1998) 13698.
[392] H. Schwenk, S. Zherlitsyn, B. Lüthi, E. Morré, C. Geibel, Phys. Rev. B 60 (1999) 9194.
[393] A. Damascelli, D. van der Marel, M. Grüninger, C. Presura, T.T.M. Palstra, J. Jegoudez, A. Revcolevschi, Phys. Rev. Lett. 81 (1998) 918.
[394] S. Ravy, J. Jegoudez, A. Revcolevschi, Phys. Rev. B 59 (1999) R681.
[395] A. Meetsma, J.L.D. Boer, A. Damascelli, J. Degoudez, A. Revcolevschi, T.T.M. Palstra, Acta Cryst. C 54 (1998) 1558.
[396] J. Galy, A. Hardy, Acta Cryst. 19 (1955) 432.

[397] D.N. Anderson, R.D. Willet, Acta Cryst. 27 (1971) 1476.
[398] J.L.D. Boer, A.M. Meetsma, J. Baas, T.T.M. Plastra, Phys. Rev. Lett. 84 (2000) 3962.
[399] A. Bernert, T. Chatterji, P. Thalmeier, P. Fulde, Eur. Phys. J. B 21 (2001) 535.
[400] M.G. Cottam, D.J. Lockwood, Light Scattering in Magnetic Solids, Wiley-Interscience, New York, 1986.
[401] T. Moriya, J. Phys. Soc. Japan 23 (1967) 490.
[402] K.B. Lyons, P.A. Fleury, L.F. Schneemeyer, J.V. Waszczak, Phys. Rev. Lett. 60 (1988) 732.
[403] M. Rübhausen, C.T. Rieck, N. Dieckmann, K.-O. Subke, A. Bock, U. Merkt, Phys. Rev. B 56 (1997) 14797.
[404] S. Sugai, S. Shamoto, M. Sato, Phys. Rev. B 38 (1988) 6436.
[405] R.C. Dynes, Solid State Commun. 92 (1994) 53.
[406] J.R. Schrieffer, Solid State Commun. 92 (1994) 129.
[407] P.A. Fleury, R. Loudon, Phys. Rev. 166 (1968) 514.
[408] A.V. Chubukov, D.M. Frenkel, Phys. Rev. B 52 (1995) 9760.
[409] F. Schönfeld, A.P. Kampf, E. Müller-Hartmann, Z. Phys. B 102 (1997) 25.
[410] F. Schönfeld, Diploma Thesis, Institut für Theoretische Physik Universität zu Köln, 1995.
[411] K. Yamamoto, T. Katsufuji, T. Tanaba, Y. Tokura, Phys. Rev. Lett. 80 (1998) 1493.
[412] G. Blumberg, M.V. Klein, S.-W. Cheong, Phys. Rev. Lett. 80 (1998) 564.
[413] Yu.G. Pashkevich, V.A. Blinkin, V.P. Gnezdilov, V.V. Tsapenko, V.V. Eremenko, P. Lemmens, M. Fischer, M. Grove, G. Güntherodt, L. Degiorgi, P. Wachter, J.M. Tranquada, D.J. Buttrey, Phys. Rev. Lett. 84 (2000) 3919.
[414] Yu.G. Pashkevich, V.A. Blinkin, V.P. Gnezdilov, V.V. Tsapenko, V.V. Eremenko, P. Lemmens, M. Fischer, G. Güntherodt, L. Degiorgi, P. Wachter, J.M. Tranquada, D.J. Buttrey, Physica B 284–288 (2000) 1473.
[415] P.H.M. van Loosdrecht, J.P. Boucher, G. Martinez, G. Dhalenne, A. Revcolevschi, Phys. Rev. Lett. 76 (1996) 311.
[416] G. Els, P.H.M. van Loosdrecht, P. Lemmens, H. Vonberg, G. Güntherodt, G. Uhrig, O. Fujita, J. Akimitsu, G. Dhalenne, A. Revcolevschi, Phys. Rev. Lett. 79 (1997) 5138.
[417] M.V. Mostovoy, M.T. Figge, J. Knoester, Phys. Rev. B 57 (1998) 2861.
[418] R.R.P. Singh, P. Prelovšek, B.S. Shastry, Phys. Rev. Lett. 77 (1996) 4086.
[419] V.N. Muthukumar, C. Gros, R. Valentí, M. Weiden, C. Geibel, F. Steglich, P. Lemmens, M. Fischer, G. Güntherodt, Phys. Rev. B 55 (1997) 5944.
[420] W. Brenig, Phys. Rev. B 56 (1997) 2551.
[421] M.J. Konstantinović, Z.V. Popović, M. Isobe, Y. Ueda, Phys. Rev. B 61 (2000) 15185.
[422] M. Matsuda, K. Katsumata, R.S. Eccleston, S. Brehmer, H.-J. Mikeska, Phys. Rev. B 62 (2000) 8903.
[423] A. Fledderjohann, C. Gros, Europhys. Lett. 37 (1997) 189.
[424] A. Dobry, D. Ibaceta, Phys. Rev. B 59 (1999) 8660.
[425] P.V. Shevchenko, V.N. Kotov, O.P. Sushkov, Phys. Rev. B 60 (1999) 3305.
[426] D. Braak, N. Andrei, Nucl. Phys. B 542 (1999) 551.
[427] Y. Fukumoto, J. Phys. Soc. Japan 69 (2000) 2755.
[428] K. Totsuka, S. Miyahara, K. Ueda, Phys. Rev. Lett. 86 (2001) 520.
[429] V.N. Kotov, J. Oitmaa, O.P. Sushkov, W.H. Zheng, Phys. Rev. B 60 (1999) 14613.
[430] P. Azaria, C. Hooley, P. Lecheminant, C. Lhuillier, A.M. Tsvelik, Phys. Rev. Lett. 81 (1998) 1694.
[431] C. Waldtmann, H.-U. Everts, B. Bernu, C. Lhuillier, P. Sindzingre, P. Lecheminant, L. Pierre, Eur. Phys. J. B 2 (1998) 501.
[432] V.N. Kotov, M.E. Zhitomirsky, O.P. Sushkov, Phys. Rev. B 63 (2001) 64412.
[433] P.H.M. van Loosdrecht, J. Zeman, G. Martinez, G. Dhalenne, A. Revcolevschi, Phys. Rev. Lett. 78 (1997) 487.
[434] T. Sekine, H. Kuroe, J. Sasaki, Y. Sasago, N. Koide, K. Uchinokura, M. Hase, J. Phys. Soc. Japan 67 (1998) 1440.
[435] Y.J. Wang, V. Kiryukhin, R.J. Birgeneau, T. Masuda, I. Tsukada, K. Uchinokura, Phys. Rev. Lett. 83 (1999) 1676.
[436] M.J. Konstantinović, K. Ladavac, A. Belić, Z.V. Popović, A.N. Vasil'ev, M. Isobe, Y. Ueda, J. Phys.: Condens. Matter 11 (1999) 2103.
[437] S. Schmidt, W. Palme, B. Lüthi, M. Weiden, R. Hauptmann, C. Geibel, Phys. Rev. B 57 (1998) 2687.
[438] R. Valentí, C. Gros, W. Brenig, Phys. Rev. B 62 (2000) 14164.
[439] H. Kuroe, H. Seto, J. Sasaki, T. Sekine, J. Phys. Soc. Japan 67 (1998) 2881.

[440] H. Kamioka, S. Saito, M. Isobe, Y. Ueda, T. Suemoto, Phys. Rev. Lett. 88 (2002) 127201.
[441] R. Merlin, G. Güntherodt, R. Humphreys, M. Cardona, R. Suryanarayanan, F. Holtzberg, Phys. Rev. B 17 (1978) 4951.
[442] J. Vitins, J. Magn. Mat. 5 (1977) 212.
[443] J. Vitins, P. Wachter, Physica B 86–88 (1977) 213.
[444] M.N. Popova, A.B. Sushkov, S.A. Klimin, E.P. Chukalina, B.Z. Malkin, M. Isobe, Y. Ueda, Phys. Rev. B 65 (2002) 144303.
[445] M. Fischer, Ph.D. Thesis, 2. Physikalisches Institut, RWTH Aachen, 2000.
[446] M.J. Konstantinović, J.C. Irwin, M. Isobe, Y. Ueda, Phys. Rev. B 65 (2001) 12404.
[447] M. Weiden, Ph.D. Thesis, Fachbereich Physik der Technischen Hochschule Darmstadt, 1997.
[448] C. Gros, R. Valentí, J.V. Alvarez, K. Hamacher, W. Wenzel, Phys. Rev. B 62 (2000) 14617.
[449] P. Lemmens, M. Fischer, M. Grove, G. Els, G. Güntherodt, M. Weiden, C. Geibel, F. Steglich, Physica B 259–261 (1999) 1050.
[450] H. Kageyama, K. Onizuka, Y. Ueda, S. Hane, H. Mitamura, T. Goto, K. Yoshimura, K. Kosuge, Proceedings of the Fourth International Symposium Advanced Physical Fields (National Research Institute for Metals, Tsukuba, Japan), Vol. B 281, 1999, p. 235.
[451] H. Kuroe, J.I. Sasaki, T. Sekine, N. Koide, Y. Sasago, K. Uchinokura, M. Hase, Phys. Rev. B 55 (1997) 409.
[452] K.B. Lyons, P.A. Fleury, Phys. Rev. Lett. 48 (1982) 202.
[453] P. Lemmens, M. Grove, M. Fischer, G. Güntherodt, H. Kageyama, K. Onizuka, Y. Ueda, Physica B 281–282 (2000) 656.
[454] P.M. Richards, W.J. Brya, Phys. Rev. B 9 (1974) 3044.
[455] W.J. Brya, P.M. Richards, Phys. Rev. B 9 (1974) 2244.
[456] B.N. Narozhny, Phys. Rev. B 54 (1996) 3311.
[457] J.W. Halley, Phys. Rev. Lett. 41 (1978) 1605.
[458] G.F. Reiter, Phys. Rev. 13 (1976) 169.